

THESIS FOR THE DEGREE OF DOCTOR OF PHILOSOPHY

Microwave Photon Generation and Entanglement for Distributed Quantum Computing

Jiaying Yang



Department of Microtechnology and Nanoscience
CHALMERS UNIVERSITY OF TECHNOLOGY
Göteborg, Sweden 2024

Microwave Photon Generation and Entanglement for Distributed Quantum Computing

JIAYING YANG

ISBN 978-91-8103-137-9

© JIAYING YANG, 2024.

Doktorsavhandlingar vid Chalmers tekniska högskola

Ny serie nr 5595

ISSN 0346-718X

Department of Microtechnology and Nanoscience

Chalmers University of Technology

SE-412 96 Göteborg, Sweden

Telephone + 46 (0)31 – 772 1000

Cover: A distributed quantum computing system, see Figure 4.1 on page 66.

Typeset by the author using L^AT_EX.

Printed by Chalmers Reproservice

Göteborg, Sweden 2024

To my grandpa 致我的姥爷

Abstract

Distributed Quantum Computing (QC) is a system that interconnects multiple quantum processors through quantum communication channels. It enables scalable and robust quantum computations by leveraging the combined capabilities of each processor. This thesis explores key components of distributed QC, specifically focusing on the generation of propagating microwave photons and the emission of entanglement using superconducting systems. We present a series of experimental and theoretical demonstrations that establish essential foundations for high-fidelity quantum state transfer and remote entanglement generation via propagating microwave photons. First, we demonstrate deterministic quantum state transfer from a superconducting qubit to a propagating microwave mode by encoding the quantum state as a superposition of the vacuum state and the single-photon Fock state. We employ photon shaping techniques to emit photons with time-symmetric amplitude and constant phase, thereby ensuring efficient reabsorption by a receiver. However, photon loss remains the primary loss channel in distributed QC networks. To address this challenge, we further propose and experimentally generate frequency-bin-encoded photonic modes, that can serve as a heralding protocol for detecting photon losses. The protocol is achieved by deterministic encoding of qubit information into two simultaneous photonic modes with different frequencies. By excluding the vacuum as a logical state, frequency-bin-encoded photons enable effective error detection at the receiver processor. Finally, we explore the generation of entangled photonic modes through the continuous driving of a quantum emitter. We demonstrate that the temporally filtered modes, obtained from the two sidebands of the resonance fluorescence spectrum, exhibit entanglement and can be extracted to separate quantum processors. These works serve as foundational building blocks for quantum state transfer and remote entanglement in distributed QC networks, with potential applications in waveguide quantum electrodynamics and scalable quantum architectures.

Keywords: Distributed quantum computing, Quantum networks, Superconducting circuits, Microwave quantum optics, Single-photon source, Single-rail photon emission, Dual-rail photon emission, Heralding protocols, Frequency-bin encoding, Entanglement

Acknowledgments

First, I would like to thank my main supervisor, Simone, for accepting me as a PhD student and providing exceptional supervision over the past five years. Simone's intelligence and abundance of ideas have greatly enriched my research, and a lot of inspirational discussions between us have been instrumental to my academic growth. I am also deeply thankful to my co-supervisor, Axel, whose dedication, professionalism, and expertise have significantly influenced me, contributing to my development as a researcher. I am grateful to my supervisors from Ericsson side, Per Persson and Asad, for their continuous support and for engaging discussions, especially when bringing in use cases relevant to the project. Your collaboration has been essential to the successful completion of this work. Additionally, I extend my sincere thanks to Per Delsing for serving as another co-supervisor from the Chalmers side, and to my examiner, Avgust, for their valuable insights and feedback.

During the past five years, I have had the pleasure of meeting many wonderful colleagues and friends. Aamir, thank you for conducting our first experiments at Luna together; it was also my first experience measuring a qubit. Looking back, we began with some basic characterization measurements, but I still find it so unforgettable the way we conducted those initial experiments step by step. Ingrid, I admire your cool personality—you are so self-motivated and confident—and it has been a joy discussing both theory and experiment with you. I would also like to extend my thanks to my office mates, Claudia, Kazi, and Linus. The time we spent chatting and supporting each other made my time at the lab enjoyable and memorable. Furthermore, I am thankful to the rest of the 202Q Lab team—Mikael, Francois, Simon, Kunal, Vyom, Ludvig, Niranjan, Vittorio, Pietro, Lukas, Harsh, Thomas and others—for making me feel consistently supported. Your willingness to help and the open environment you create have been invaluable. There is no shame in asking for help from you all, and your support has greatly contributed to my progress.

I would like to thank my excellent theory collaborators: Maryam, Akshay, Anton and Göran from AQP, as well as Alejandro and Carlos from Universidad Autónoma de Madrid, Spain. Your intelligence and professionalism have greatly enhanced our collaboration, and I am delighted to have had the opportunity to work with you. Hope that there can be more collaboration in the future. While I did not perform the fabrication myself, Claudia, Daniel, Amr, and Janka provided invaluable assistance with fabricating the devices and addressing all my questions regarding fabrication. Without your hard work in the cleanroom, I would not have been able to begin my experiments. Special thanks to Marco for designing the sample holder and to Lars

for fabricating it, as well as for making all the copper parts we urgently ordered for the fridge.

I would also like to express my gratitude to my colleagues on the 7th floor QT team for their continual support. Philip Krantz interviewed me before I began my PhD studies. After four years apart, he attended my presentation and provided me with significant encouragement, helping me to recognize the progress I have made over these years. Heartfelt thanks to Linda for always being helpful and enabling us to focus on our research. I am grateful to Yong, Marina, Hangxi, Liangyu, Hampus, Chris, Andreas, Tong, Emil, Giovanna, Anita, Daryoush, Anuj, Tom, Sahar and others for their valuable discussions. Additionally, thank you to Oleskiy and Olga for helping with the operation and maintenance of the dilution refrigerators.

I have also received significant support from my colleagues at Ericsson. Beatriz, my line manager, has helped me with all administrative matters related to my industrial PhD. Beyond that, I can talk with her like a friend regarding my concerns and career planning. Rana, as my project manager, has provided me with valuable advice from a more technical perspective. I would also like to thank my other colleagues at Ericsson: Ahsan, Catrin, Azimeh, Gemma, Diarmuid, Jonas, Björn, and others. Although I spent most of my time physically at Chalmers, your warm welcome whenever I visited Kista made me feel at home.

Thank you to my friends in Gothenburg and Stockholm for always being so kind and consistently responding positively when I invited you out. However, I am not a good friend who had to decline several of your invitations due to my busy PhD schedule, but you never blamed me and were always understanding. Additionally, I extend my thanks to friends who are further away; it was delightful to reunite with you during meetings and trips, and I cherished those moments. I have also organized a Chinese lunch in the building, it is nice to meet you people once a week, and we can 'practice' our Mandarin together.

Finally, I would like to thank my family for their unwavering support. 最后, 谢谢家人对我一如既往地支持。I didn't realize it until when I am approaching 30, that I have received the most precious gift of life, that is your unconditional love from my parents. 在我即将30岁的时候, 我才意识到我早就已经获得了人生最珍贵的礼物, 来自原生家庭的无条件的爱。Thank you for your unconditional support in every decision I have made, although the decisions sometimes make me further and further away from you in distance. 谢谢你们总是无条件的支持我的所有决定, 即便我的决定常常让我们在距离上越来越远。I would like to thank my grandpa for your simple wisdom and belief in the power of education. 感谢我的姥爷, 你朴素的智慧和永远相信教育的力量, 我很想念你。My husband, Yiping, is probably the person who has witnessed me the most during my five years of PhD studies. Thank you for your companionship over not only the past five years, but also the five years before that. We understand each other deeply, and you are my best friend. Finally, I'd like to thank myself for going through such a long journey.

Jiaying Yang

Göteborg, November 2024

List of Publications

This thesis is based on the following appended papers:

Paper 1. Jiaying Yang, Axel Martin Eriksson, Mohammed Ali Aamir, Ingrid Strandberg, Claudia Castillo-Moreno, Daniel Perez Lozano, Per Persson, and Simone Gasparinetti. *Deterministic generation of shaped single microwave photons using a parametrically driven coupler*. Physical Review Applied 20, 054018 (2023).

Paper 2. Jiaying Yang, Ingrid Strandberg, Alejandro Vivas-Viaña, Akshay Gaikwad, Claudia Castillo-Moreno, Anton Frisk Kockum, Muhammad Asad Ullah, Carlos Sánchez Muñoz, Axel Martin Eriksson, and Simone Gasparinetti. *Entanglement of photonic modes from a continuously driven two-level system*. arXiv:2407.07991.

Paper 3. Jiaying Yang, Maryam Khanahmadi, Ingrid Strandberg, Akshay Gaikwad, Claudia Castillo-Moreno, Anton Frisk Kockum, Muhammad Asad Ullah, Göran Johansson, Axel Martin Eriksson, and Simone Gasparinetti. *Deterministic generation of frequency-bin-encoded microwave photons*. arXiv:2410.23202.

Other relevant publications co-authored by Jiaying Yang:

Yong Lu, Marina Kudra, Timo Hillmann, **Jiaying Yang**, Hang-Xi Li, Fernando Quijandría, and Per Delsing . *Resolving Fock states near the Kerr-free point of a superconducting resonator*. npj Quantum Information volume 9, Article number: 114 (2023)

Axel Martin Eriksson, Théo Sépulcre, Mikael Kervinen, Timo Hillmann, Marina Kudra, Simon Dupouy, Yong Lu, Maryam Khanahmadi, **Jiaying Yang**, Claudia Castillo-Moreno, Per Delsing, and Simone Gasparinetti. *Universal control of a bosonic mode via drive-activated native cubic interactions*. Nature Communications volume 15, Article number: 2512 (2024)

List of Acronyms

1D	–	One Dimensional
2D	–	Two Dimensional
ac	–	alternating current
ADC	–	Analog-to-Digital Converter
AWG	–	Arbitrary Waveform Generator
CP	–	Completely Positive
CPW	–	CoPlanar Waveguide
CS	–	Compressed Sensing
dc	–	direct current
GD	–	Gradient Descent
LO	–	Local Oscillator
LS	–	Least Squares
NISQ	–	Noisy Intermediate-Scale Quantum
QC	–	Quantum Computing
QED	–	Quantum ElectroDynamics
QPT	–	Quantum Process Tomography
QST	–	Quantum State Tomography
RWA	–	Rotating Wave Approximation
SNAIL	–	Superconducting Nonlinear Asymmetric Inductive Element
SQUID	–	Superconducting Quantum Interference Device
TLS	–	Two-Level System
TP	–	Trace Preserving
TWPA	–	Traveling Wave Parametric Amplifier
VNA	–	Vector Network Analyzer
wQED	–	waveguide Quantum ElectroDynamics

Contents

Abstract	v
Acknowledgments	vii
List of Publications	ix
List of Acronyms	xi
I Thesis	1
1 Introduction	3
1.1 Introduction to Distributed Quantum Computing	3
1.2 Superconducting circuit	7
1.2.1 Circuit elements	7
1.2.2 Quantum harmonic oscillator	8
1.2.3 Superconducting transmon qubit	10
1.2.4 Flux-tunable transmon qubit with SQUID	13
1.2.5 Readout resonator	14
1.2.6 Jaynes-Cummings model	15
1.2.7 Decoherence	15
1.2.8 Waveguide	16
2 Methods	19
2.1 Cryogenic setup	19
2.2 TWPA calibration	21
2.3 Device	24
2.4 Temporal mode matching and moment denoising	26
2.5 Photonic-state tomography	29
2.5.1 State tomography	29
2.5.2 Process tomography	31
2.5.3 Analysis of the reconstructed matrix	33

3 Experiments	35
3.1 Deterministic single-rail photon emission	35
3.1.1 Method 1 – Parametric drive emission	36
3.1.2 Method 2 – Second-order transition emission	42
3.2 Photon shaping to facilitate reabsorption	44
3.2.1 Photon envelope reshaping	44
3.2.2 Photon phase compensation	45
3.3 Dual-rail photon emission in frequency bins	48
3.3.1 Setup	48
3.3.2 Experiments	50
3.3.3 Tomography results	52
3.4 Generation of entangled photons from continuously-driven TLS	54
3.4.1 Experimental setup	54
3.4.2 Theoretical model	56
3.4.3 Single-mode measurement results	57
3.4.4 Two-mode measurement results	59
3.4.5 Tomography result and logarithmic negativity	61
4 Conclusions	65
4.1 Summary	65
4.2 Outlook	65
4.2.1 Potential distributed QC system	66
4.2.2 Applications of distributed QC systems	67
5 Appendix	71
5.1 Room-temperature measurement setup	71
5.1.1 Continuous-wave setup	71
5.1.2 Pulsed setup	72
5.2 Device characterization measurements	75
5.2.1 From continuous-wave setup	75
5.2.2 From pulsed setup	79
Bibliography	85
II Appended papers	97
1 Deterministic generation of shaped single microwave photons using a parametrically driven coupler	99
2 Entanglement of photonic modes from a continuously driven two-level system	115
3 Deterministic generation of frequency-bin-encoded microwave photons	137

Part I

Thesis

Chapter 1

Introduction

This thesis is structured as follows. In this introductory chapter, we first explore the motivation and background for the work, with a literature review of the state-of-the-art distributed quantum computing systems, which is the main goal of this work. We then present the foundational concepts necessary for understanding photonic-state generation and qubit entanglement in superconducting circuits, which form the basis for distributed quantum computing.

Chapter 2 covers the common methodologies used across all of our experiments. Chapter 3 presents the experiments described in Paper 1 to Paper 3. Chapter 4 provides a summary and outlook for future research. Chapter 5, included as an appendix, contains additional information relevant to the experiments.

1.1 Introduction to Distributed Quantum Computing

Distributed quantum computing.— Quantum computing (QC) offers promising solutions to complex computational problems by leveraging the principles of superposition and entanglement [1]. However, in the noisy intermediate-scale quantum (NISQ) era [2], these processors are constrained by both the number of qubits and noise. To address these limitations, quantum processors must be scaled up [3], as practical quantum computing will likely require tens of thousands to millions of physical qubits to implement quantum error correction (QEC) [4].

As single-chip quantum processors scale up, various constraints emerge, including wafer size, available refrigerated space, and cooling power [5, 6], presenting significant challenges. Moreover, as quantum processors grow, the likelihood of all qubits functioning reliably on the same chip decreases. For instance, if each qubit has a 0.1% chance of failure, a processor with 1,000 qubits would have approximately a 37% probability that no qubits fail, and a processor with 10,000 qubits would have only about a 0.005% chance to have all qubits flawless. This estimate assumes that correlated errors are excluded from consideration, though these types of errors also increase as qubit numbers grow and represent an additional factor that motivates the need for distributed architectures. Consequently, instead of solely scaling up

a single quantum chip, distributed QC architectures or quantum networks [7, 8] offer an alternative solution by distributing computations across multiple processors, thereby enabling the cooperative resolution of larger tasks.

To implement a distributed QC architecture, quantum channels—communication pathways for transmitting quantum information—are required between remotely distributed quantum processors. For platforms with trapped-ion qubits [9], neutral atoms [10, 11], semiconductor quantum dots [12, 13], and color-center qubits [14, 15], quantum channels can be implemented using optical fibers to transmit photons over long distances, mediating entanglement between distant qubits [16]. However, the process using the optical channels is typically probabilistic, or with a low information transfer rate. Superconducting quantum processors function within the microwave frequency range, where photons possess significantly lower energies compared to their optical counterparts. In recent years, these processors have made impressive strides toward scalable quantum computing. However, the lower energy of microwave photons introduces challenges for establishing long-distance channels at room temperature. This is because transmitting microwave photons in such conditions results in a significant increase in thermal noise, i.e., in the regime of $k_B T \gg \hbar\omega$ (where the thermal energy $k_B T$ is much greater than the energy of a single photon $\hbar\omega$), leading to a much higher presence of thermal photons compared to optical channels. To address this, transducers between microwave and optical photons [17–21] can be used to establish photonic channels between superconducting quantum processors. Nonetheless, practical applications in quantum communication remain limited due to the difficulty of achieving high-efficiency, low-noise transduction. Therefore, superconducting qubits connected solely by microwave channels currently represent a more feasible testbed, offering a deterministic method for transferring information between remote processors. Thus, for the remainder of this section, we focus on the implementation of microwave quantum channels between superconducting processors.

Distributed QC with superconducting qubits and microwave channels. — In superconducting circuits, the microwave-based quantum channels can be implemented based on standing modes [22, 23] or travelling microwave photons [5, 24–28]. In the first case, photons are transferred coherently through the discrete modes of the channel. However, the standing modes begin to overlap with increasing distance, forcing the cable lengths to be approximately one meter or less [22]. In the latter case, to transfer travelling microwave photons, it is essential to prevent reflected signals from returning to the emitter’s node. In [5, 24–26], this is done by adding a circulator in the middle of the channel, allowing the reflected signal to go through the third port of the circulator. In this way, the quantum channel can be modelled as a continuum of states with microwave photons travelling through. However, the circulator adds around 1 dB insertion loss to the process and forces the transmission to be unidirectional. Another method to prevent the reflected signal is to ensure that the emitted photons have temporal widths comparable to the cable length of the channel [27–29], fulfilling $L \sim \frac{\lambda}{2} = \frac{c}{2\Gamma}$. In this formula, L represents the cable length of the quantum channel and λ denotes the wavelength of the photon, which can be calculated as the ratio of the signal propagation speed c to the photon’s decay rate Γ . With this relation fulfilled, the adjacent standing modes merge together, and we

can also model the channel as a continuum. For either method—adding a circulator or ensuring the relation between the decay rate and the channel length—the photon carrying quantum information is emitted by the sender processor, travels through the quantum channel, and is reabsorbed by the receiver processor. This process enables deterministic quantum state transfer and remote entanglement between the qubits on both processors.

In [5], a cryogenic microwave link was established between two dilution refrigerators separated by a physical distance of five meters. While extending such setups to larger configurations presents challenges, efforts are shifting toward integrating microwave links within a single cryostat. The work in [23] represents state-of-the-art scalability, achieving entanglement between six superconducting qubits across two distinct processors, while Ref. [27] demonstrates the longest-distance quantum channel to date, spanning 64 meters. Moreover, quantum teleportation based on remote entanglement between processors has been achieved, as shown in [27, 30]. In related developments, Reference [31] presents a modular quantum computing system consisting of four modules interconnected via a router built with Superconducting Nonlinear Antisymmetric Inductive Element (SNAIL) technology. Finally, in [32, 33], a giant artificial molecule is used to enable bidirectional photon emission, facilitating the connection of more than two processors along a single waveguide.

Single-rail photon emission and reshaping.— Single-rail photon emission encodes the quantum information of a static qubit into the presence or absence of a single photon in a specific mode, serving as a fundamental component of distributed QC systems. As demonstrated in [34], photon reshaping is crucial in the emission process, because it enables reabsorption through the time-reversed process of emission, significantly increasing absorption efficiency from 54% to over 99%. Several studies have explored single-photon emission and reshaping using superconducting qubits [35–38]. Reference [36] employs a straightforward design, featuring a qubit coupled to a source line with a flux-tunable coupling rate to the waveguide for emitting and reshaping photons. References [35, 37] utilizes a qubit-cavity or qubit-resonator system for single-photon emission, leveraging a second-order transition to emit and reshape photons.

In our work (Paper 1), we implement a single-photon emission source based on parametric coupling [39] between two transmon qubits. We have achieved a deterministic transfer of a qubit state into a propagating microwave photon with a process fidelity of 94.5%. Compared to [40] with a similar structure, we use a time-dependent parametric drive to shape the temporal profile of the propagating mode, ensuring its time symmetry and constant phase, which allows the reabsorption process by a receiving processor to be implemented as a time-reversed version of the emission [35].

Dual-rail photon emission.— The emitted microwave photons are exposed to noise during transmission through the quantum channel, posing a risk of photon loss when transmitting quantum information between remotely distributed quantum processors. For example, transmission losses in superconducting coaxial cables and waveguides at cryogenic temperatures can reach up to 5×10^{-3} dB/m [41], significantly higher than the 2×10^{-4} dB/m typically observed in optical fibres [42]. When using single-rail

photon emission to transmit quantum information, the loss of a single photon results in the loss of the encoded information, making the system highly vulnerable to transmission noise. Error detection protocols can address this issue by introducing an additional degree of freedom in the emission, converting the emission from a single-rail into a dual-rail photon emission. Dual-rail encoding employs two distinct modes—such as time-bin [43, 44], frequency-bin [45–47], polarization [48], path [49, 50], or angular momentum [51]—to represent the quantum information redundantly, which are commonly utilized in the optical regime. The fact that the vacuum is not a logical state allows the dual-rail photon to serve as a heralding protocol for error detection, addressing photon loss at the receiver processor. In [52, 53], time-bin encoded photon is experimentally demonstrated using superconducting qubits. In comparison, frequency-bin encoded photons offer a higher data rate by emitting at different frequencies simultaneously, doubling the transmission speed. However, to the best of our knowledge, no implementation of frequency-bin encoded photons exists in the microwave regime. Furthermore, if such an implementation were to be developed, it would typically necessitate additional hardware resources, such as extra qubits functioning as quantum state emitters, to emit both photons simultaneously.

In our work (Paper 3), we experimentally generate frequency-bin encoded photons using a qubit-coupler-qubit structure similar to that in Paper 1, where one qubit is strongly coupled to the waveguide. However, rather than using the coupler to mediate interactions between the qubits, we tune it into resonance with the emitter qubit to form a hybridized emitter. By applying two simultaneous pulses—one that preserves excitation and one that does not—we transfer the quantum state from the data qubit to the hybridized emitter. This allows for the simultaneous emission of two propagating modes at different frequencies. Our approach is hardware-efficient, as it eliminates the need for adding extra emitter qubits coupled to the waveguide.

Entangled photons from a resonance fluorescence system.— We now shift to a different framework for exploring entanglement, a fundamental feature of quantum mechanics. Entangled photons have broad applications in quantum communication [54–56] and distributed quantum computing [57–59]. Here we investigate entangled photonic modes from a coherently and continuously driven qubit, which can be described by a resonance fluorescence system [60]. Resonance fluorescence systems have been demonstrated to exhibit a rich landscape of multi-photon correlations, non-classical states and entanglement. Wigner-negative states have been shown to be achievable in such systems by continuously driving a qubit to its steady state, with both theoretical studies [61, 62] and experimental demonstrations [63] using a superconducting qubit. Moreover, higher-order correlations between the two-photon modes within this scheme have been explored both theoretically [64–66] and experimentally using quantum dots [67, 68]. In [69], Lopez et al. theoretically propose a method for generating entangled photons by off-resonantly driving a qubit and measuring the emission from the sidebands of the Mollow triplet [70, 71]. In our work (Paper 2), we demonstrate entanglement by combining the time and frequency dimensions through the selection of two temporally overlapping, yet spectrally orthogonal, photonic modes. The entanglement can be physically extracted and transferred to quantum memories to perform quantum information processing tasks or entanglement dis-

tribution, which can be potentially used in a distributed QC system for enhanced scalability and connectivity.

In summary, the three works in this thesis concentrate on two main aspects. The first one is encoding quantum information from the superconducting qubit to microwave photonic modes (Paper 1 and 3), with the later paper introducing error-detection protocol against photon loss. The second aspect is generating entangled photonic modes from a continuously driven superconducting qubit (Paper 2). Together, these contributions serve as fundamental building blocks for distributed QC systems in the microwave regime, with the potential to extend to broader applications.

1.2 Superconducting circuit

1.2.1 Circuit elements

Quantum electrodynamics (QED) provides a framework for studying interactions between light and matter at the quantum level, specifically within superconducting circuits. Superconducting qubits, which act as artificial atoms in this setting, are constructed from engineered circuit elements that leverage the principles of superconductivity. These elements, including capacitance, inductance, and the Josephson junction, form the foundation of superconducting qubit circuits and enable the controlled manipulation of quantum states.

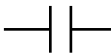
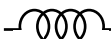

Circuit element	Symbol	Energy
Capacitance		$E_C = \frac{1}{2}C\dot{\Phi}^2$
Inductance		$E_L = \frac{\Phi^2}{2L}$
Josephson junction		$E_{JJ} = E_J \left[1 - \cos \left(2\pi \frac{\Phi}{\Phi_0} \right) \right]$

Table 1.1: Elements for superconducting qubit circuit

Capacitance (C) quantifies a capacitor's ability to store charge. The energy stored in a capacitor is $E_C = \frac{1}{2}CV^2$. Since the voltage across the capacitor relates to the time derivative of the magnetic flux (Φ) by $V = \dot{\Phi}$, the energy can also be expressed as $E_C = \frac{1}{2}C\dot{\Phi}^2$.

Inductance (L) quantifies an inductor's ability to store energy in a magnetic field when current flows through it. The energy stored in an inductor is $E_L = \frac{1}{2}LI^2$. Since the magnetic flux (Φ) through the inductor relates to the current (I) by $\Phi = LI$, the energy can also be expressed as $E_L = \frac{\Phi^2}{2L}$.

A Josephson junction is a nonlinear inductance made up of a thin insulating barrier between two superconducting materials [72] [Fig. 1.1]. In our experiment, we use aluminium as the superconducting material and aluminium oxide as the insulator. Unlike a normal inductance, the Josephson junction exhibits nonlinear

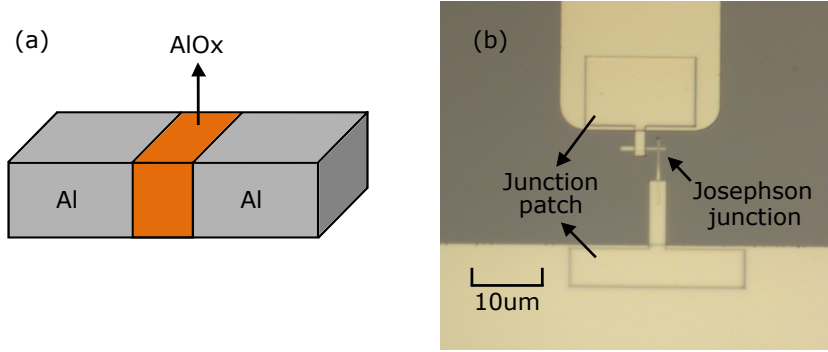


Figure 1.1: Josephson junction. (a) A schematic symbol, including two superconductors (Aluminium, Al) separated by an insulating barrier (Aluminium oxide, AlOx). (b) Photo of the Josephson junction in one of our devices. The junction is formed by two superconductors positioned perpendicularly to each other with a thin insulating layer between them. The junction patch serves as the interface between the junction arms and the rest of the circuit.

behaviour due to the tunnelling of Cooper pairs between the superconductors at low temperatures [72].

Josephson junction is characterized by two fundamental relations, the dc and ac Josephson relations. The former one describes the supercurrent I_s as a function of the phase difference ϕ between the superconducting condensates on the two sides of the junction,

$$I_s = I_c \sin \phi. \quad (1.1)$$

where I_c is the critical current. The second relation, the ac Josephson relation, links the time derivative of the phase difference to the voltage V across the junction,

$$\frac{d\phi}{dt} = \frac{2eV}{\hbar}. \quad (1.2)$$

Here, e is the elementary charge and \hbar is the reduced Planck's constant.

According to the ac Josephson relation, the voltage V across the junction is $V = \dot{\phi} = \frac{\hbar}{2e} \frac{d\phi}{dt}$, where the phase difference ϕ can be written by $\phi = 2\pi \frac{\Phi}{\Phi_0}$, with $\Phi_0 = \frac{h}{2e}$ the magnetic flux quanta. By combining these equations with the dc Josephson relation, integrating the power over time gives the energy E_{JJ} stored in the junction,

$$E_{JJ} = \int P dt = \int I_s V dt = \int I_c \sin \phi \cdot \frac{\hbar}{2e} \frac{d\phi}{dt} = E_J \left[1 - \cos \left(2\pi \frac{\Phi}{\Phi_0} \right) \right], \quad (1.3)$$

where $E_J = \frac{\hbar I_c}{2e}$ is the Josephson energy.

1.2.2 Quantum harmonic oscillator

To study superconducting qubit circuits, we can begin with the foundational concept of a quantum harmonic oscillator, formed by an LC circuit [Fig. 1.2(a)]. In our case, we consider the wavelength of the oscillator to be much larger than the physical

size of the circuit. This ensures that the circuit can be accurately modelled as a lumped element, where the inductance and capacitance are concentrated in discrete components.

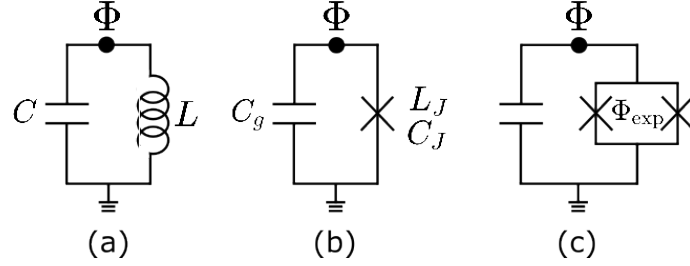


Figure 1.2: (a) Parallel LC circuit. (b) Fixed-frequency superconducting qubit circuit. (c) Frequency-tunable superconducting qubit circuit, enabled by a SQUID loop consisting of two Josephson junctions and applied external flux.

The Lagrangian \mathcal{L} of an LC circuit is given by the difference between the kinetic energy T and the potential energy V given by capacitance and inductance, respectively,

$$\mathcal{L} = T - V = \frac{1}{2}C\dot{\Phi}^2 - \frac{\Phi^2}{2L}. \quad (1.4)$$

For the transition from the Lagrangian to the Hamiltonian, we first define the conjugate momentum to the flux as Q , representing the charge on the capacitance,

$$Q = \frac{\partial \mathcal{L}}{\partial \dot{\Phi}} = C\dot{\Phi}. \quad (1.5)$$

Using the classical definitions of charge Q and flux Φ , we can express the Hamiltonian H for a circuit as:

$$H = Q\dot{\Phi} - \mathcal{L} = \frac{Q^2}{2C} + \frac{\Phi^2}{2L},$$

where the terms correspond to the energy stored in the capacitor (charge Q) and the inductor (flux Φ), respectively. This Hamiltonian describes a classical harmonic oscillator with a resonance frequency of $\frac{1}{\sqrt{LC}}$.

To transfer to the quantum mechanical representation, we promote the classical variables Q and Φ to quantum operators \hat{Q} and $\hat{\Phi}$. The quantum Hamiltonian is then written as,

$$\hat{H} = \frac{\hat{Q}^2}{2C} + \frac{\hat{\Phi}^2}{2L} = 4E_C\hat{n}^2 + \frac{1}{2}E_L\hat{\phi}^2,$$

where we define the reduced charge operator $\hat{n} = \frac{\hat{Q}}{2e}$ and flux operator $\hat{\phi} = \frac{2\pi\hat{\Phi}}{\Phi_0}$, with Φ_0 the flux quantum. $E_C = \frac{e^2}{2C}$ represents the charging energy. $E_L = \Phi_0^2/4\pi^2L$ defines the inductive energy. In this quantum mechanical framework, \hat{Q} and $\hat{\Phi}$ are no longer just real numbers but quantum operators, satisfying the canonical commutation relation,

$$[\hat{\Phi}, \hat{Q}] = i\hbar. \quad (1.6)$$

By introducing the annihilation operator \hat{a} [73],

$$\hat{n} = i \left(\frac{E_L}{32E_C} \right)^{1/4} (\hat{a}^\dagger - \hat{a}), \quad (1.7)$$

$$\hat{\phi} = \left(\frac{2E_C}{E_L} \right)^{1/4} (\hat{a}^\dagger + \hat{a}), \quad (1.8)$$

The Hamiltonian of the quantum harmonic oscillator can be rewritten as,

$$\hat{H} = \hbar\omega \left(\hat{a}^\dagger \hat{a} + \frac{1}{2} \right), \quad (1.9)$$

where the angular frequency ω of the quantum harmonic oscillator is given by $\omega = \frac{8\sqrt{E_C E_L}}{\hbar} = \frac{1}{\sqrt{LC}}$.

1.2.3 Superconducting transmon qubit

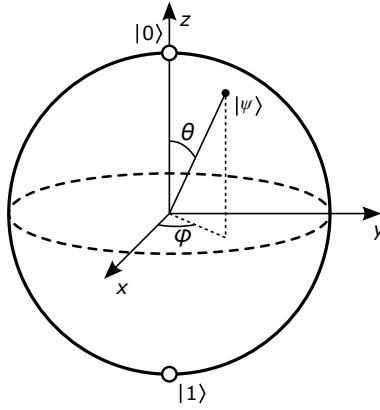


Figure 1.3: The Bloch sphere, with figure taken from [74].

The state of a qubit can be described by a state vector on a Bloch sphere (Fig. 1.3),

$$|\psi\rangle = \cos \frac{\theta}{2} |0\rangle + \sin \frac{\theta}{2} e^{i\varphi} |1\rangle, \quad (1.10)$$

with θ and φ angles in real values. Here, $|0\rangle = \begin{pmatrix} 1 \\ 0 \end{pmatrix}$ and $|1\rangle = \begin{pmatrix} 0 \\ 1 \end{pmatrix}$ represent the two basis states of the qubit. The manipulation of this state to perform quantum operations relies on the application of quantum gates, which can be expressed using the Pauli operators, defined as,

$$\hat{\sigma}_X = \begin{pmatrix} 0 & 1 \\ 1 & 0 \end{pmatrix}, \quad \hat{\sigma}_Y = \begin{pmatrix} 0 & -i \\ i & 0 \end{pmatrix}, \quad \hat{\sigma}_Z = \begin{pmatrix} 1 & 0 \\ 0 & -1 \end{pmatrix}. \quad (1.11)$$

There are many physical ways to implement qubits, such as trapped-ion qubits [75, 76], photonic qubits [77], quantum dots [78, 79], and superconducting circuits. Among

these implementations, superconducting qubits [80–84] have gained significant improvements due to their scalability and compatibility with existing technologies, such as cryogenic systems for maintaining low-temperature environments, high-fidelity microwave control systems for qubit manipulation, and standard semiconductor fabrication techniques used to produce Josephson junctions and other circuit elements. Charge qubits are one of the most commonly used types of superconducting qubits [85].

The Cooper-pair box is the first type of superconducting charge qubit that can be coherently controlled in experiments [86]. It has the structure of two superconducting islands connected via a Josephson junction, as the equivalent circuit shown in Fig. 1.2(b). The system's behaviour is governed by the charging energy $E_C = e^2/2C$, which favours discrete charge states on the island, and the Josephson energy E_J , which enables Cooper-pair tunnelling through the junction.

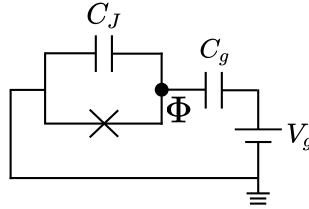


Figure 1.4: Circuit representation of the Cooper-pair box qubit.

To derive the Hamiltonian of a cooper-pair box qubit, we start with deriving the Lagrangian from a more explicit circuit representation (Fig. 1.4),

$$\mathcal{L} = T - V = \frac{1}{2}C_J\dot{\Phi}^2 + \frac{1}{2}C_g(V_g - \dot{\Phi})^2 + E_J \cos\left(\frac{\pi\Phi}{\Phi_0}\right). \quad (1.12)$$

Φ is the flux floating through the marked node in the circuit. The charge at this node can be calculated as,

$$Q = \frac{\partial L}{\partial \dot{\Phi}} = C_J\dot{\Phi} - C_g(V_g - \dot{\Phi}) \implies \dot{\Phi} = \frac{Q + C_gV_g}{C_J + C_g}. \quad (1.13)$$

We can now compute the Hamiltonian as follows,

$$H(\Phi, Q) = Q\dot{\Phi} - \mathcal{L} = \frac{1}{2} \frac{(Q + C_gV_g)^2}{C_J + C_g} - E_J \cos\left(\frac{2\pi\Phi}{\Phi_0}\right). \quad (1.14)$$

Introducing the dimensionless offset charge $n_g = \frac{C_gV_g}{2e}$, the charge energy $E_C = \frac{e^2}{2C_\Sigma} = \frac{e^2}{2(C_J+C_g)}$, and the number of Cooper pairs in the superconducting island $n = -\frac{Q}{2e}$, we can rewrite the Hamiltonian as,

$$H = 4E_C(n - n_g)^2 - E_J \cos\left(\frac{2\pi\Phi}{\Phi_0}\right). \quad (1.15)$$

We can then quantize the system, promoting n and Φ to operators, which fulfills the commutation relation,

$$\left[\frac{2\pi\hat{\Phi}}{\Phi_0}, \hat{n} \right] = -i. \quad (1.16)$$

where $\hat{n} |n\rangle = n |n\rangle$, with n being the number of excess Cooper pairs on the island.

Using the Baker-Campbell-Hausdorff lemma, $e^{\pm i \frac{2\pi\hat{\Phi}}{\Phi_0}} |n\rangle = |n \pm 1\rangle$, which shows that the exponential of the phase operator can act as a ladder operator on the charge basis, and the relation $\cos\left(\frac{2\pi\hat{\Phi}}{\Phi_0}\right) = \frac{1}{2} \left(e^{i \frac{2\pi\hat{\Phi}}{\Phi_0}} + e^{-i \frac{2\pi\hat{\Phi}}{\Phi_0}} \right)$, we can rewrite the Hamiltonian as,

$$\hat{H} = 4E_C \sum_n (\hat{n} - n_g)^2 |n\rangle\langle n| - \frac{E_J}{2} \sum_n (|n+1\rangle\langle n| + |n\rangle\langle n+1|). \quad (1.17)$$

When operating within the offset charge range $0 < n_g < 1$, the Cooper-pair box qubit can be effectively described in the two-charge state basis $\{|0\rangle, |1\rangle\}$, leading to the Hamiltonian,

$$\hat{H} = -\frac{E_{\text{ch}}(n_g)}{2} \hat{\sigma}_Z - \frac{E_J}{2} \hat{\sigma}_X, \quad (1.18)$$

where $E_{\text{ch}}(n_g) = 4E_C(1 - 2n_g)$, and $\hat{\sigma}_X$ and $\hat{\sigma}_Z$ are the Pauli operators.

The Cooper-pair box qubit has comparable E_J and E_C . In Fig. 1.5(a), we plot the lowest energy levels five of the Hamiltonian in Eq. (1.17), with $E_J = E_C$. We can see that the energy levels of the Cooper-pair box qubit vary significantly with the gate charge n_g , making the qubit highly sensitive to charge noise and limiting the coherence time of the qubit. To improve coherence time, n_g needs to be adjusted to the sweet point [87], which is at $n_g = 1/2$. At this point, the slope of the eigenenergies is zero respective to n_g , meaning that the noise will not affect the qubit frequency, thereby reducing the impact of dephasing. However, it is difficult to achieve this precisely in experiments.

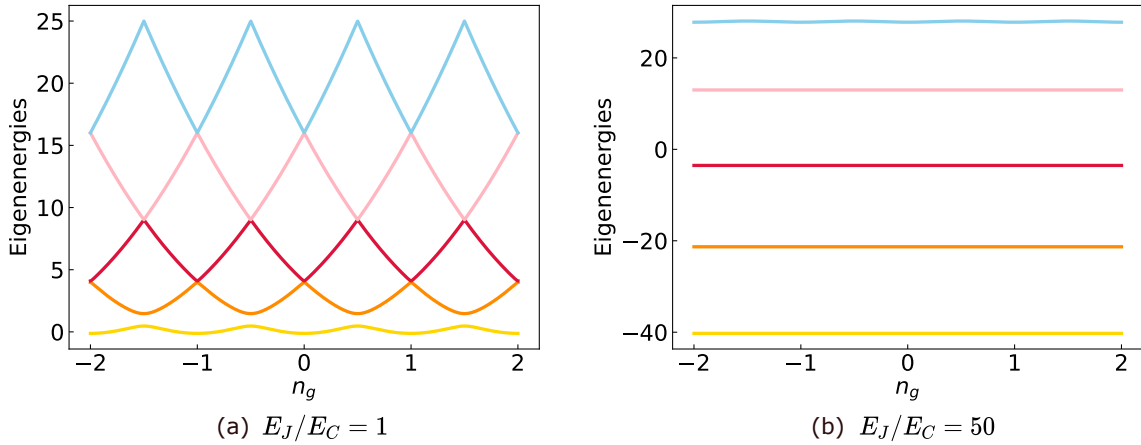


Figure 1.5: The lowest five energy levels of the Cooper-pair box qubit as a function of the gate charge, with (a) $E_J/E_C = 1$, and (b) $E_J/E_C = 50$, in the transmon regime.

To mitigate this issue, the transmon regime was introduced [88]. By increasing the ratio to ensure $E_J \gg E_C$, the energy levels become less dependent on n_g . In Figure 1.5(b), we show the energy levels with $E_J = 50E_C$, illustrating that the level spacing becomes nearly independent of the gate charge. This reduced sensitivity

to charge fluctuations enhances the qubit's coherence times, making the transmon qubit a more robust candidate for quantum computing.

By Taylor expanding the cosine term $\cos \hat{\phi} = \cos\left(\frac{2\pi\hat{\Phi}}{\Phi_0}\right)$ in Eq. (1.15), and introducing the annihilation operator \hat{a} as in Eq. (1.8), the Hamiltonian of transmon can be computed as,

$$\hat{H} = \hbar\omega_Q\hat{a}^\dagger\hat{a} + \frac{\hbar\alpha}{2}\hat{a}^\dagger\hat{a}^\dagger\hat{a}\hat{a}, \quad (1.19)$$

where $\omega_Q = \frac{\sqrt{8E_C E_J - E_C}}{\hbar}$ is the qubit transition frequency between the lowest two energy levels, and $\alpha = -E_C$ represents the anharmonicity of the qubit.

1.2.4 Flux-tunable transmon qubit with SQUID

By introducing a Superconducting Quantum Interference Device (SQUID) loop, we can turn a fixed-frequency transmon qubit into a flux-tunable one [Fig. 1.2(c)]. The SQUID, consisting of two Josephson junctions in a superconducting loop, has a flux-dependent Josephson energy. By applying external flux, Φ_{exp} , to the flux line that is inductively coupled to the SQUID loop (see Fig. 1.6 for the photo), the magnetic field through the loop is altered, which changes the phase difference across the junctions. This, in turn, modifies the effective Josephson energy, allowing us to tune the qubit frequency. For devices without an on-chip flux line, external flux can be applied using a coil positioned vertically above or below the device.

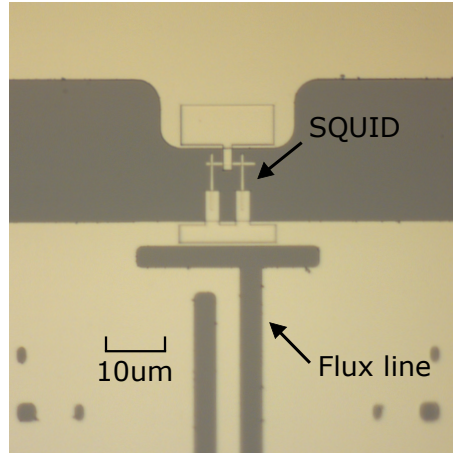


Figure 1.6: Photo of a SQUID loop on our device, which is inductively coupled to a flux line for applying external flux.

The effective Josephson energy $E_J(\Phi_{\text{exp}})$ of the flux-tunable transmon qubit is given by [89],

$$E_J(\Phi_{\text{exp}}) = E_{J\Sigma} \cos\left(\pi \frac{\Phi_{\text{exp}}}{\Phi_0}\right) \sqrt{1 + \left[d \tan\left(\pi \frac{\Phi_{\text{exp}}}{\Phi_0}\right)\right]^2}, \quad (1.20)$$

where Φ_{exp} is the applied magnetic flux through the SQUID loop, which is sometimes simplified to Φ in the next chapters. Φ_0 is the magnetic flux quanta. $E_{J\Sigma} = E_{J1} + E_{J2}$

is the total Josephson energy of the two junctions. $d = \frac{\beta - 1}{\beta + 1}$ is the junction asymmetry parameter, with $\beta = E_{J1}/E_{J2}$ and $E_{J1} \geq E_{J2}$. The qubit frequency ω_Q is then tunable, dependent on the applied flux Φ_{exp} ,

$$\omega_Q = \sqrt{8E_J(\Phi_{\text{exp}})E_C} - E_C. \quad (1.21)$$

Typically, flux-tunable transmon qubits are designed with symmetric Josephson junctions in the SQUID loop, meaning both junctions have equal Josephson energies ($E_{J1} = E_{J2}$). This symmetry enables tuning the qubit frequency down to zero with flux, as shown in the blue curve in Fig 1.7, and this is used in the couplers in our Device 1 and 2 in the following chapters of this thesis.

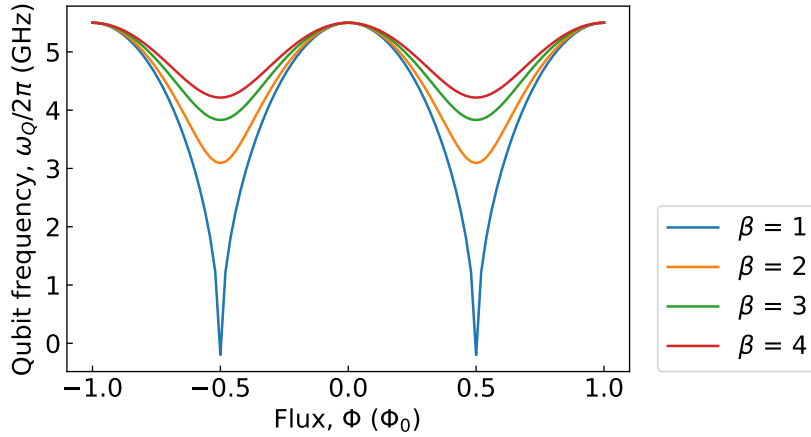


Figure 1.7: An example of the qubit frequency as a function of flux for different asymmetry parameters (β).

However, using symmetric junctions can make the qubit more susceptible to flux noise, which can degrade coherence times and cause flux crosstalk between two flux-tunable qubits [90]. Introducing asymmetry between the junctions ($E_{J1} > E_{J2}$) can mitigate this issue. An asymmetric transmon provides a smaller frequency-tuning range that is sufficient for frequency tunability variations (see the rest of the curves in Fig 1.7) without introducing unnecessary sensitivity to flux noise. The asymmetric junctions ($\beta = 3.6$) are used in the SQUID loop of our emitter qubit in Device 2, where both the coupled coupler and emitter qubit are flux-tunable, to reduce the crosstalk.

1.2.5 Readout resonator

We use a coplanar waveguide (CPW) for propagating photons on a superconducting quantum chip, which consists of a center conductor separated from the ground plane by gaps at both sides. In this section, we mainly focus on the transmission line resonators for the qubit-state readout. The readout resonators employed are designed as either quarter-wavelength ($\lambda/4$, with unequal boundary conditions at both ends) or half-wavelength ($\lambda/2$, with equal boundary conditions at both ends) resonators.

In this thesis, we use the $\lambda/4$ -type resonator, which has one end open, and the other end shorted to the ground plane. The Hamiltonian of the resonator can be described as a quantum harmonic oscillator as in Eq. (1.9). The CPW resonators also have important parameters including quality factor (Q) and its coupling strength to the qubit (j), which will be explained more explicitly in Sec. 2.3 and 5.2.1.

1.2.6 Jaynes-Cummings model

To analyze the interaction between a qubit and a readout resonator, we need a framework that captures the effect of their coupling j on both the qubit and resonator properties. The Jaynes-Cummings model provides an effective description of this coupled system, capturing how the qubit-resonator interaction modifies the frequencies of each component. When they are not interacting, considering the qubit as a two-level system (TLS), they can be described by the bare Hamiltonian,

$$\hat{H}_{\text{bare}} = \underbrace{\frac{1}{2}\hbar\omega_Q\hat{\sigma}_Z}_{\text{Qubit}} + \underbrace{\hbar\omega_R(\hat{a}^\dagger\hat{a} + \frac{1}{2})}_{\text{Resonator}}. \quad (1.22)$$

Considering the interaction between the qubit and the coupler, the Hamiltonian becomes,

$$\hat{H}_{\text{JC}} = \underbrace{\frac{1}{2}\hbar\omega_Q\hat{\sigma}_Z}_{\text{Qubit}} + \underbrace{\hbar\omega_R(\hat{a}^\dagger\hat{a} + \frac{1}{2})}_{\text{Resonator}} + \underbrace{\hbar j(\hat{a}\sigma_+ + \hat{a}^\dagger\sigma_-)}_{\text{Interaction}}, \quad (1.23)$$

where $\hat{\sigma}_- = |g\rangle\langle e| = \begin{pmatrix} 0 & 0 \\ 1 & 0 \end{pmatrix}$ and $\hat{\sigma}_+ = |e\rangle\langle g| = \begin{pmatrix} 0 & 1 \\ 0 & 0 \end{pmatrix}$ are the lowering and raising operators for the qubit, respectively. The two non-energy-conserving parts of the interaction Hamiltonian, $a\sigma_-$ and $a^\dagger\sigma_+$, are dropped.

In this thesis, we work in the dispersive regime for the qubit and the resonator, where the detuning between them, $\Delta = |\omega_Q - \omega_R|$, is much larger than the coupling, $\Delta \gg j$, and the direct excitation transfer between them is depressed [91]. By applying perturbation theory in j/Δ , we can find the dispersive Hamiltonian,

$$\hat{H}_{\text{disp}} = \frac{1}{2}\hbar(\omega_Q + \chi)\hat{\sigma}_Z + \hbar(\omega_R + \chi\hat{\sigma}_Z)\hat{a}^\dagger\hat{a}, \quad (1.24)$$

where $\chi = j^2/\Delta$. Now the frequency of the resonator becomes $\omega_R \pm \chi$, depending on the state of the qubit. At the same time, the level separation in the qubit $\hbar(\omega_Q + \chi + 2\chi\hat{a}^\dagger\hat{a})$ also depends on the number of photons in the resonator, since $\hat{n} = \hat{a}^\dagger\hat{a}$ is the photon number operator. We call $\chi = j^2/\Delta$ the Lamb shift and $2\chi\hat{a}^\dagger\hat{a}$ the ac Stark shift.

1.2.7 Decoherence

When a quantum system interacts with its environment, it gradually loses its quantumness through a process known as decoherence. This process can be characterized

by two relaxation rates: the longitudinal relaxation rate $\Gamma_1 = 1/T_1$ and the transverse relaxation rate $\Gamma_2 = 1/T_2$.

The longitudinal relaxation rate Γ_1 describes the rate at which the population of the qubit's energy states decays, leading to energy dissipation to the environment. The transverse relaxation rate Γ_2 captures the combined effects of both longitudinal relaxation and pure dephasing, which results in the loss of coherence between quantum states. This rate is expressed as,

$$\frac{1}{T_2} = \frac{1}{2T_1} + \frac{1}{T_\varphi}, \quad (1.25)$$

where $\Gamma_\varphi = 1/T_\varphi$ represents the pure dephasing rate, indicating the rate at which phase coherence is lost without energy dissipation. In the ideal scenario where the qubit's transition frequency remains perfectly stable over time, and there is no photon shot noise[92] or other sources of dephasing present, we should observe that $T_2 = 2T_1$.

After decoherence, the qubit can no longer be represented as a pure state, or as a vector on the Bloch sphere's surface. Instead, the qubit's state falls inside the Bloch sphere, and it has become a mixed state due to interactions with the environment. In this case, the state can only be described by a density matrix ρ rather than a state vector. The density matrix provides a more general representation of the qubit's statistical state, for both pure state and mixed state of the qubit. The purity of a quantum state becomes less than 1, $\text{Tr}(\rho^2) < 1$ (for a pure state, the purity is 1). After time t , the density matrix of a qubit state initialized in $\alpha|0\rangle + \beta|1\rangle$ becomes [93] due to the relaxation,

$$\rho = \begin{pmatrix} 1 + (|\alpha|^2 - 1)e^{-\Gamma_1 t} & \alpha\beta^* e^{i\Delta t} e^{-\Gamma_2 t} \\ \alpha^*\beta e^{-i\Delta t} e^{-\Gamma_2 t} & |\beta|^2 e^{-\Gamma_1 t} \end{pmatrix}, \quad (1.26)$$

where the phase $e^{-i\Delta t}$ is introduced by the detuning between the qubit and the drive, $\Delta = \omega_Q - \omega_d$.

1.2.8 Waveguide

A waveguide quantum electrodynamics (wQED) system, where a qubit couples to a one-dimensional superconducting transmission line, enables strong and controllable interactions between quantum emitters and guided photonic modes. Unlike the readout resonator, which is a discrete harmonic oscillator designed for measuring the qubit's state, the waveguide in a wQED system acts as an open-ended, one-dimensional continuum that allows propagating photonic modes to travel through.

When considering one single mode in the waveguide, with the annihilation operator denoted as \hat{a} , we can write the Hamiltonian for the qubit-waveguide coupling system,

$$\hat{H} = \frac{\hbar\omega_Q}{2}\hat{\sigma}_Z + \hbar\Gamma\hat{\sigma}_Z(\hat{a} + \hat{a}^\dagger). \quad (1.27)$$

where Γ_1 is the relaxation decay rate of the qubit, defined as $\Gamma_1 = \Gamma_r + \Gamma_{nr}$, the sum of the radiative decay rate Γ_r and the non-radiative decay rate, Γ_{nr} , the rate of qubit decaying into the environment.

In a waveguide quantum electrodynamics (wQED) setup, the interaction between the qubit and the waveguide introduces dissipation, as photons emitted by the qubit can escape into the waveguide modes and travel away. This process can be effectively captured by a master equation in the Lindblad form [94], which describes the non-unitary dynamics of the qubit's density matrix, ρ , due to the coupling to the waveguide. The master equation for the qubit-waveguide system, assuming a Markovian environment, is given by,

$$\frac{d\rho}{dt} = -\frac{i}{\hbar} [\hat{H}, \rho] + \Gamma_1 \mathcal{D}[\hat{\sigma}_-]\rho + \frac{1}{2} \Gamma_\varphi \mathcal{D}[\hat{\sigma}_Z]\rho, \quad (1.28)$$

where the first term represents the evolution of the system governed by the Hamiltonian. The second term represents the dissipative dynamics due to the total excitation decay of the qubit, with $\mathcal{D}[\hat{X}]\rho = \hat{X}\rho\hat{X}^\dagger - \frac{1}{2}(\hat{X}^\dagger\hat{X}\rho + \rho\hat{X}^\dagger\hat{X})$. The last term considers the dissipation due to the pure dephasing rate Γ_φ .

When the qubit is driven by an external continuous wave at Rabi frequency Ω , by transforming into the rotating frame at the drive frequency, the Hamiltonian of the qubit-waveguide interaction can be expressed as,

$$\hat{H}_{\text{eff}} = \frac{\Delta}{2} \hat{\sigma}_Z + \frac{\Omega}{2} (\hat{\sigma}_+ + \hat{\sigma}_-), \quad (1.29)$$

where $\Delta = \omega_Q - \omega_d$ is the detuning between the qubit frequency and the drive frequency ω_d . To analyze this system, we use the master equation in the steady-state limit, describing the dynamics with the Lindblad operator $\mathcal{D}[\hat{\sigma}_-]$,

$$L\rho = \Gamma_1 \mathcal{D}[\hat{\sigma}_-]\rho + \frac{1}{2} \Gamma_\varphi \mathcal{D}[\hat{\sigma}_Z]\rho. \quad (1.30)$$

According to input-output theory [95–97], the outgoing field can be expressed in terms of the incoming field and the expectation value of the qubit's lowering operator $\langle \hat{\sigma}_- \rangle$, specifically,

$$\hat{a}_{\text{out}} = \hat{a}_{\text{in}} + \sqrt{\Gamma_r} \langle \hat{\sigma}_- \rangle. \quad (1.31)$$

Solving the master equation with the effective Hamiltonian for $\langle \hat{\sigma}_- \rangle$ and using the definition of the incoming field, $\hat{a}_{\text{in}} = \frac{\Omega}{2\sqrt{\Gamma_r}}$, we obtain the reflection coefficient,

$$S_{11} = \frac{\hat{a}_{\text{out}}}{\hat{a}_{\text{in}}} = 1 - \frac{2\Gamma_r (\Gamma_1 + \Gamma_\varphi - 2i\Delta)}{(\Gamma_1 + \Gamma_\varphi)^2 + 4\Delta^2 + \Omega^2}. \quad (1.32)$$

Chapter 2

Methods

This chapter provides an overview of the experimental setup and methodologies to achieve low-noise measurements of the generated propagating modes in our system. We begin by detailing the cryogenic setup and the calibration of the Travelling Wave Parametric Amplifier (TWPA), both of which are critical for minimizing thermal and amplifier noise. We then describe the device architecture, which serves as the foundational platform for all the experiments presented in the subsequent chapters. Next, we explore the techniques of temporal mode matching and moment denoising, which are crucial for characterizing the propagating photonic modes with minimal noise interference. Finally, photonic state tomography is introduced as a powerful tool for reconstructing the quantum states of light, allowing for the analysis of the performance of our system. Together, these elements create an optimal environment for the measurement and characterization of propagating microwave modes.

2.1 Cryogenic setup

In our experimental setup, the quantum device is prepared for testing within a cryogenic environment to achieve the ultra-low temperatures necessary for qubit operation. The device is cooled down to below 15 mK inside a dilution refrigerator [Fig. 2.1(a-b)]. To initiate the cooling cycle of a dilution refrigerator, a starting temperature close to that of liquid helium (4.2 K) or lower must first be achieved, typically using a pulse tube cooler. The dilution refrigerator then uses the heat of mixing between the two helium isotopes, ^3He and ^4He , to reach 15 mK or lower [98].

The cold temperature is crucial for enabling the superconductivity of the circuit. The critical temperature (T_c) for Aluminium is around 1.2 K, meaning that the elements on the devices become superconducting only below this temperature. Additionally, the low temperature creates a low-noise environment for the measurements, as it significantly reduces thermal noise. This is important because we require the condition $\hbar\omega_Q \gg k_B T$, where \hbar is the reduced Planck's constant, ω_Q is the angular frequency of the qubit transitions, k_B is Boltzmann's constant, and T is the temperature of the device. The ultra-low temperature of < 15 mK ensures that thermal energy remains much lower than the qubit transition energy, $\hbar\omega_Q$, thereby minimizing thermal excitations and reducing decoherence. This environment enables

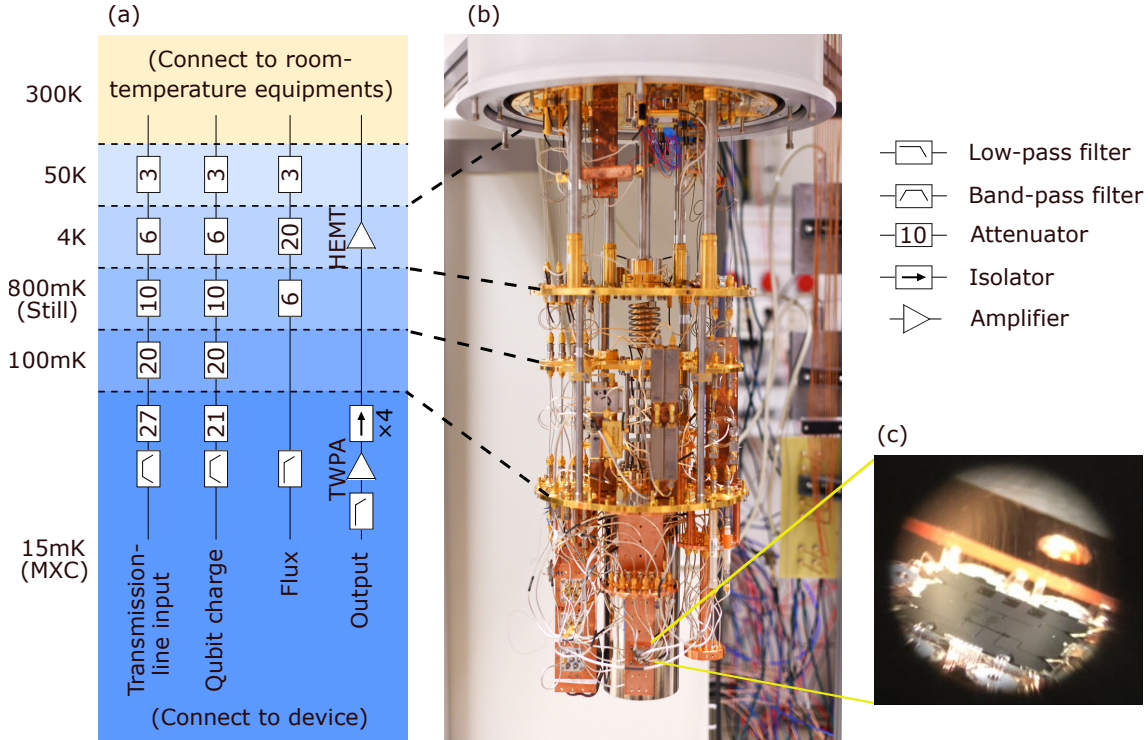


Figure 2.1: (a) Wiring diagram of the selected lines within the dilution refrigerator [98]. MXC stands for the mixing chamber layer. Other elements are defined in the legend on the right. (b) A picture of the Bluefors dilution refrigerator, named Wampa, where all measurements in this thesis are conducted. (c) One of our devices wire-bonded in the sample holder, and then mounted in the mixing-chamber layer of the fridge.

more accurate and reliable quantum measurements.

Figure 2.1(a) shows the wiring diagram inside the dilution refrigerator, including the transmission input line, qubit charge line, flux line, and output line (see Fig. 2.4 for how the device is connected to the lines). The transmission line is capacitively coupled to readout resonators that interact with the qubit and the coupler, allowing microwave signals to be delivered for qubit readout. The charge line is also capacitively coupled to the qubit, enabling the control of the qubit. The flux line, inductively coupled to the qubit or the coupler, modulates the magnetic flux, facilitating the tuning of the qubit or coupler’s energy levels alongside the SQUID loop.

The input of the transmission line is highly attenuated to reduce thermal photons propagating down the line from the room temperature environment, which helps minimize the thermal population of qubits and preserve their coherence. Additionally, attenuators are distributed across each layer of the refrigerator rather than concentrated at the coldest stages to prevent heat dissipation from significantly burdening the refrigerator’s cooling power [6]. On the output side, where signals are weaker, amplification is necessary to boost the qubit signals for analysis without adding significant noise, enabling assessment of the qubit states. Isolators and circulators are used to shield the sample from thermal noise photons along the output line and amplifier noise, without attenuating the output signal. For the same reasons, in

the input lines, the coaxial cables between each layer of the refrigerator are usually lossy to further dampen thermal noise. In contrast, the output lines use NbTi superconducting coaxial cables to preserve signal fidelity as they transmit amplified qubit signals from the coldest stage up to room temperature. The filters on both the input and output lines are selected with passbands centered around the qubit and resonator frequencies, while the stopbands provide additional suppression of thermal radiation.

The amount of attenuation in the three types of input lines follows: transmission input line (readout line) > qubit charge line > flux line. Because the qubit's decay rate into the charge line is much smaller than its total decay rate, $\Gamma_c \ll \frac{1}{T_1}$, thermal noise photons entering through the charge line have a negligible impact on qubit decoherence compared to the readout line. This allows for lower attenuation in the charge line, balancing the need to minimize thermal noise with the requirement to deliver high-power control signals to implement fast qubit rotations. The flux line has the least attenuation due to the weak magnetic coupling, enabling these lines to support higher signal powers for implementing desired operations while minimizing the current noise that can lead to qubit dephasing [6, 99].

When operating the flux line, both dc and ac signals are transmitted through the attenuated lines. Both components induce power dissipation as they flow through the resistive elements of the attenuators. However, the power dissipation from the ac signals is minimal and often negligible due to their low power and pulsed operation. To avoid excessive heating of the refrigerator, we focus on the dc component, calculating the power dissipation based on the resistive configuration of the attenuators at each stage of the dilution refrigerator. By comparing the calculated dissipation to the cooling capacity of each respective refrigerator layer, we verify that the power dissipation remains below the cooling power thresholds, ensuring there is no danger of heating up the fridge too much. An alternative method transmits dc signals through superconducting twisted-pair lines to minimize electromagnetic interference, while ac signals are sent through attenuated flux lines. Twisted-pair configurations cancel the magnetic fields generated by parallel conductors by twisting the lines, thereby reducing electromagnetic interference. Cryogenic bias tees can be employed to combine the separate dc and attenuated ac lines in the mixing chamber—the lowest layer—of the refrigerator.

2.2 TWPA calibration

The HEMT amplifier in the output line provides a high gain in excess of 40 dB but adds around 10 noise photons to the signal, which is problematic for measurements at the single-photon level. Therefore, we benefit from using a nearly quantum-limited amplifier, such as a Travelling-Wave Parametric Amplifier (TWPA) or Josephson Parametric Amplifier (JPA), for pre-amplification to measure the low-power propagating modes. These amplifiers add noise close to the quantum limit by employing non-linear parametric amplification techniques in superconducting circuits, enabling precise measurements at the single-photon level. In this thesis, a 4-wave-mixing TWPA amplifier with a pump signal is employed. The TWPA

is connected to the waveguide's output line via a circulator, allowing calibration through measurements of the qubit coupled to the waveguide (see Sec. 2.3 for further details on the device). The objective is to assess the gain and the noise photon number under various configurations of the TWPA pump signal, for the improvement of the readout of propagating modes.

The gain of the amplification chain (including the TWPA, HEMT, and the room-temperature amplifiers in the output line) is measured using a vector network analyzer (VNA). By comparing the reflection parameter S_{11} when the TWPA is on and off, the gain is determined (Fig. 2.2). This procedure overestimates the gain by a few dB, because a turned-off TWPA acts as a few dB attenuator.

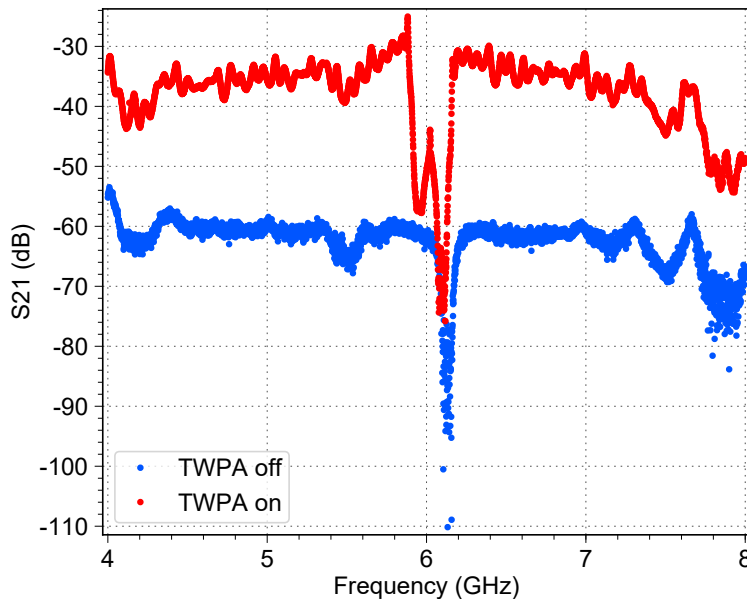


Figure 2.2: A single-tone spectroscopy measurement of the emitter qubit at the waveguide, with the qubit frequency shifted outside the bandwidth, is used to determine the on-off gain of the TWPA (details of the VNA measurement are provided in Sections 5.1.1 and 5.2.1). The stopband in the gain profile results from phase mismatching, while the ripples are caused by impedance mismatching.

In addition to the gain, it is important to assess the noise performance of the TWPA. We introduce three methods for calibrating the noise photon number; ultimately, we choose the third method as it aligns with our measurement requirements for quantum tomography.

The first method calibrates n_{noise} using the following relation,

$$n_{\text{noise}} = \frac{P_{\text{noise}}}{\hbar\omega_Q BG}, \quad (2.1)$$

where P_{noise} is the measured noise power at the output after the TWPA, which can be obtained through a power spectrum density (PSD) measurement by a spectrum analyzer. $\hbar\omega_Q$ is the power of a single photon at the frequency of interest. B is the resolution bandwidth of the measurement. G is the total system gain. Note that this differs from the on-off TWPA gain mentioned earlier. Here, $G = S_{11}^{\text{on}} + A$, where S_{11}^{on}

is the reflection parameter measured with the TWPA turned on, and A represents the total attenuation in the system.

The second method involves calibrating n_{noise} from the PSD measurement of the Mollow triplet [70], as follows,

$$n_{\text{noise}} = \frac{P_{\text{noise}}}{P_{\text{on, central}} - P_{\text{off, central}}}, \quad (2.2)$$

where P_{noise} is the measured noise power, and $P_{\text{on, central}}$ ($P_{\text{off, central}}$) represents the normalized on (off) power of the central peak in the Mollow triplet.

The third method leverages the measurements used in our quantum tomography experiments. In this thesis, we emit propagating modes from stationary qubits and use temporal mode matching and quantum tomography to characterize these modes. The same measurements can also be employed to calibrate the noise photon number. We measure the emitted photon in an interleaved manner, alternating between two cases: with and without the operating pulses [see Sec. 2.4 for more details]. In the case without operating pulses, we perform repeated single-shot measurements of the vacuum state, capturing both quadratures, \hat{X} and \hat{P} . These single-shot measurement results are then compiled into a two-dimensional (2D) histogram in the IQ plane, representing the quadrature space [Fig. 2.3(a)]. The histogram is normalized based on the operating-pulse-on histogram of the system, with the assumption that our system functions as a single-photon source. We can then model the histogram as a thermal state [100, 101], as shown in Fig. 2.3(b-d). The noise photon number can be extracted by taking a slice from the 2D histogram and then fitting the histogram to the convolution [102],

$$\int P_n^{\text{th}}(\alpha^* - \beta^*) Q(\beta) d^2\beta. \quad (2.3)$$

$Q(\beta)$ in the convolution is the Husimi Q function [103], and $P_n^{\text{th}}(\alpha)$ is the function of a thermal state [104],

$$P_n^{\text{th}}(\alpha) = \frac{1}{\pi n_{\text{noise}}} \exp\left[-\frac{|\alpha|^2}{n_{\text{noise}}}\right]. \quad (2.4)$$

The noise photon number, n_{noise} , is the only unknown parameter and can be determined through this fitting procedure. By measuring n_{noise} in this method at different settings of the TWPA, i.e., pump power and pump frequency, we can determine the optimal working point of the TWPA. In our case, the TWPA can reduce the added noise photon number to below 5.

The system's quantum efficiency, denoted by η , can be calculated from the noise photon number,

$$\eta = \frac{\frac{1}{2}}{n_{\text{noise}} + \frac{1}{2}}, \quad (2.5)$$

where the $\frac{1}{2}$ in the formula is due to the added photon number $n_{\text{noise}} = \frac{G+1}{2G}$. For a perfect gain $G \rightarrow \infty$, the added photon number is $\frac{1}{2}$.

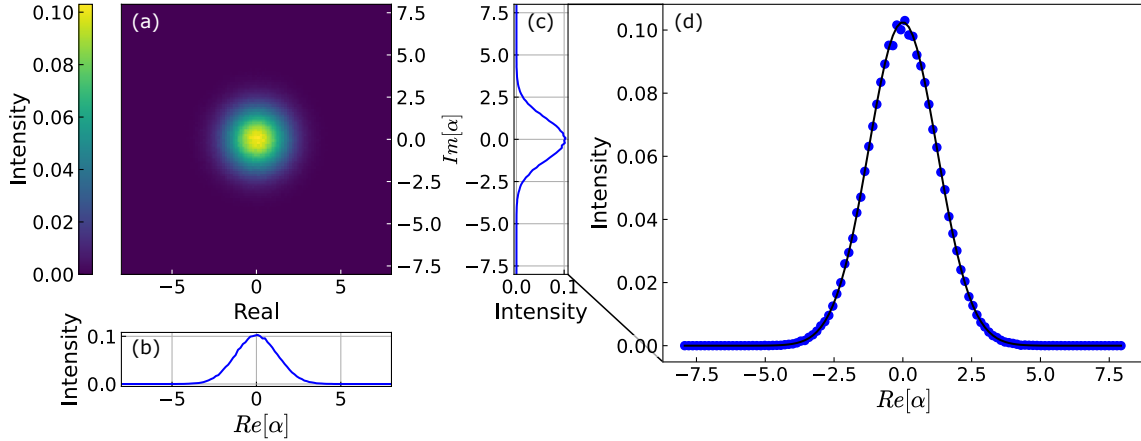


Figure 2.3: Calibration of the noise photon number n_{noise} in this thesis. (a) An example of a 2D histogram measured with the operating pulses turned off, leaving the target mode in a vacuum state, serves as a reference for the noise mode during measurement. (b-c) Horizontal and vertical linecuts taken through the center of the histogram in (a). (d) A zoom-in view of the vertical linecut in (c), fitted to the model of a thermal state to extract n_{noise} .

2.3 Device

In this work, we utilize two $6.6 \times 6.6 \text{ mm}^2$ superconducting devices, both with a similar capacitance layout as Fig. 2.4. The device is fabricated on a silicon substrate, and its ground plane consists of a single layer of Aluminium deposited on top of the substrate. Although this thesis does not contain any fabrication work, we briefly summarize the fabrication process as follows:

- Dip the silicon substrate in SC-1 (Standard Clean 1 [105]) and HF (hydrofluoric acid).
- Deposit the Aluminium layer with an electron-beam evaporator.
- Spin-coat the resist, followed by photolithography and development to create the desired pattern on the resist layer.
- Perform wet-etching to transfer the pattern from the developed resist layer to the substrate. After this step, the ground plane of the device is fabricated.
- Fabricate the Josephson junctions and the patches using electron-beam lithography, as the features are smaller than the resolution limit of photolithography, followed by deposition, in-situ oxidation, and lift-off.
- Airbridges are typically added to mitigate ground plane discontinuities, which can give rise to higher-order parasitic modes; however, this is not applied in this thesis, as wire bonds are used in places of airbridges.
- Dicing of the whole wafer into separate chips.

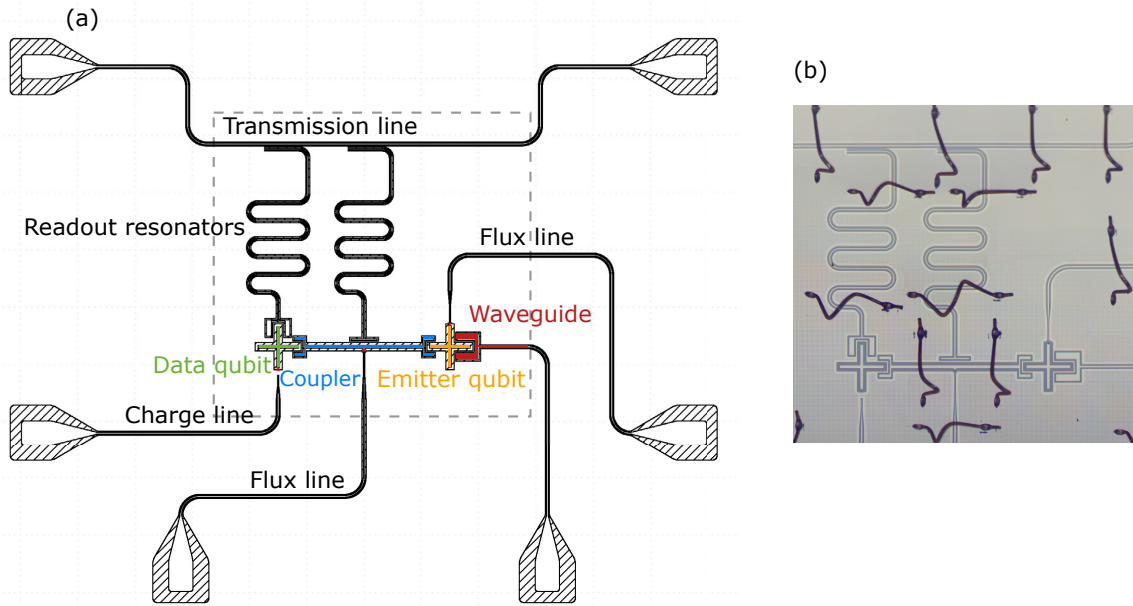


Figure 2.4: (a) Schematic design layout of Device 2, with key components highlighted in colors. The hatched regions represent the exposed silicon substrate. The three red dots are the three Josephson junctions or SQUIDs and their patches of the qubit or coupler. (b) Microscope photograph of Device 2, corresponding to the area within the grey dashed rectangle in (a). Device 1 has the same layout as Device 2, but the emitter qubit has a charge line instead of a flux line. The black wires in the picture are the Aluminium-bonded wires acting as airbridges.

After the device is fabricated, we wire-bond the device in a copper sample holder, which is then enclosed within a copper shield. To provide additional protection against magnetic interference, the copper shield is placed inside another μ -metal shield (cryoperm). The fully shielded assembly is installed in the mixing chamber layer of a dilution refrigerator, ensuring that all experimental measurements are conducted at temperatures below 15 mK.

We have used two devices in the experiments of this thesis. In our devices, we have a qubit-coupler-qubit structure, with one of the qubits, the emitter qubit [orange in Fig. 2.4(a)], strongly coupled to the waveguide (dark red). The coupler (blue) is frequency-tunable, enabled by the SQUID coupled to it. In Device 2, the emitter qubit is flux-tunable as well. The data qubit (green) and the coupler are coupled to their corresponding readout resonators. The readout resonator on the emitter qubit is omitted to ensure a larger claw-shaped capacitance for enhanced coupling to the waveguide. Since the emitter qubit is rarely occupied, direct measurement through the waveguide is sufficient, eliminating the need for a dedicated readout resonator. We adapt our devices from the device used in [106], which, however, did not include the coupling of a qubit to a waveguide.

Of the two devices we have, Device 1 is used for the following experiments:

- Deterministic single-rail photon emission (Paper 1, explained in Sec. 3.1)
- Photon reshaping for photon reabsorption (Paper 1, explained in Sec. 3.2)

- Generation of entangled photons from steady-state qubit (Paper 2, explained in Sec. 3.4)

Device 2 is used in the experiment:

- Dual-rail photon emission in frequency bins (Paper 3, explained in Sec. 3.3)

The measured parameters of both devices, listed in Table 2.1, are experimentally obtained according to the methods in Appendix 5.2. Among all parameters, the coupling rates are designed according to the capacitance matrix of the components on the device. The coupling rate between the qubit and their readout resonator j is designed according to [107],

$$j = \frac{C_j}{2\sqrt{C_{\Sigma_Q}C_{\Sigma_R}}} \sqrt{\omega_R\omega_Q}. \quad (2.6)$$

Here, C_j is the capacitance between the qubit and the resonator, C_{Σ_Q} is the total capacitance of the qubit, and C_{Σ_R} is the total capacitance of the readout resonator. Capacitance matrix simulations in this thesis are performed using the software Ansys HFSS [108]. Similarly, the coupling strength g between the qubit and the coupler can be designed in the same way, according to,

$$g = \frac{C_g}{2\sqrt{C_{\Sigma_Q}C_{\Sigma_C}}} \sqrt{\omega_Q\omega_C}, \quad (2.7)$$

with C_g the capacitance between the qubit and the coupler and C_{Σ_C} the total capacitance of the coupler. Moreover, the coupling rate between the emitter qubit and the waveguide, Γ_E , is determined by [109],

$$\Gamma_E = \omega_E^{ge2} C_{\Sigma_E} \beta^2 (N_0 + 1) Z_0, \quad (2.8)$$

where $\beta = \frac{C_{gE}}{C_{\Sigma_E}}$, with C_{gE} the capacitance between the emitter qubit and the waveguide, and C_{Σ_E} the total capacitance of the emitter qubit. Here, $N_0 = \frac{1}{\exp(\hbar\omega_E^{ge}/k_B T) - 1}$, approximated to 0 at low temperatures in the dilution refrigerator. Z_0 is the frequency-independent impedance. Design considerations for the remaining parameters are discussed in detail in the thesis [107].

We have also measured the relaxation rates of the data qubit (Table 2.2). In the ideal case, T_1^{ge} of a qubit should be the double of T_1^{ef} , however, we measure larger T_1^{ef} than T_1^{ge} , which can be attributed to the weaker coupling of the system to the environment at ω_D^{ef} compared to ω_D^{ge} .

2.4 Temporal mode matching and moment denoising

In this thesis, we explore propagating modes generated from the superconducting qubit. Temporal mode matching is used to isolate the emitted modes from the

Table 2.1: Experimentally measured parameter values for the devices. Regarding the readout resonators, f_R represents the frequencies of the readout resonators; κ are the decay rates of the resonator to the transmission line; j is the coupling rate between the data qubit (coupler) and their readout resonator. Without dc flux bias, the transition frequencies of qubits (coupler) are represented by ω^{ge} ; while with dc biases tuning the flux tunable qubit (coupler) into the operating points in the experiments, we represent the mode frequencies as $\omega^{ge'}$. α is the anharmonicity of qubit (coupler). The coupling strength between the qubit and the coupler is represented by g , while the radiative decay rate from the emitter qubit into the waveguide is Γ_E . The not-existing parameters are marked with $-$.

Parameter	Device 1			Device 2		
	Data qubit (fixed-freq)	Coupler (flux-tunable)	Emitter qubit (fixed-freq)	Data qubit (fixed-freq)	Coupler (flux-tunable)	Emitter qubit (flux-tunable)
$f_R/2\pi$ (GHz)	6.17	6.72	-	6.19	6.74	-
$\kappa/2\pi$ (kHz)	632	772	-	523	752	-
$j/2\pi$ (MHz)	66.75	43.34	-	69.33	42.34	-
$\omega^{ge}/2\pi$ (GHz)	4.771	7.735	4.953	5.05	8.46	6.17
$\omega^{ge'}/2\pi$ (GHz)	4.770	6.0	4.950	5.05	5.79	5.70
$\alpha/2\pi$ (MHz)	-224	-62	-	-215	-60	-215
$g/2\pi$ (MHz)	33.85	-	34.28	37.5	-	46
$\Gamma_E/2\pi$ (MHz)	-	-	8.0	-	-	8.0

Table 2.2: For both devices, the longitudinal relaxation time T_1^{ge} ($T_1^{ge'}$) of the data qubit is measured without (with) dc flux bias, and the transverse relaxation rate T_2^{ge} ($T_2^{ge'}$) of the qubit are also measured without (with) flux bias. We have also measured the relaxation rates between the second- and the first-excited states of the data qubit, for Device 2. For the coupler in Device 2, T_1^{ge} and T_2^{ge} are also measured. The relaxation rates that are not measured are marked with $/$.

Parameter	Device 1		Device 2	
	Data qubit	Data qubit	Data qubit	Coupler
T_1^{ge} (μ s)	25.6 ± 10.4	21.7 ± 3.6	2.3 ± 0.5	
$T_1^{ge'}$ (μ s)	28.3 ± 9.2	20.8 ± 2.5		$/$
T_2^{ge} (μ s)	15.6 ± 4.7	5.7 ± 0.7	1.4 ± 0.4	
$T_2^{ge'}$ (μ s)	13.3 ± 3.7	14.0 ± 3.4		$/$
T_1^{ef} (μ s)	$/$	27.0 ± 3.0		$/$
$T_1^{ef'}$ (μ s)	$/$	27.0 ± 3.0		$/$
T_2^{ef} (μ s)	$/$	4.4 ± 0.5		$/$
$T_2^{ef'}$ (μ s)	$/$	8.8 ± 1.4		$/$

continuum of modes in the waveguide [110]. To extract the time-independent photon mode, \hat{a} , from the time-dependent output field measured from the output line connected to the waveguide after all amplification, $\hat{a}_{\text{out}}(t)$, we apply digitally the

temporal filter $f(t)$,

$$\hat{a} = \int_{-\infty}^{\infty} dt f(t) \hat{a}_{\text{out}}(t), \quad (2.9)$$

where $\hat{a}_{\text{out}}(t)$ follows from the input-output relation outlined in Eq. (1.31). The function of the temporal filter $f(t)$ is defined as,

$$f(t) = v(t) \cdot e^{i(\omega_f t + \phi)}, \quad k = 1, 2. \quad (2.10)$$

Here, we use complex temporal filters $f(t)$, with $v(t)$ representing the real wavepacket profile and ϕ the constant phase. $v(t)$ should match the temporal shape of the photon field to achieve optimal matching efficiency. The frequency of the temporal filter, ω_f , is set to the carrier frequency of the emitted radiation. The extracted modes obey the bosonic commutation relations $[\hat{a}, \hat{a}^\dagger] = 1$, which are guaranteed by the normalization condition of the filter function, given by $\int_{-\infty}^{\infty} dt |f(t)|^2 = 1$. In our measurement, temporal mode matching is achieved through the FPGA-based Vivace microwave transceiver platform [111] in the room-temperature setup (see Sec. 5.1.2).

However, in the measurement, we cannot obtain the mode \hat{a} directly from the temporal mode matching, because it is affected by various noise sources, such as cable loss, added amplification noise, and the inefficiency of the mode matching. Thus, we denote the measured mode as \hat{S} , containing both quadratures \hat{X} and \hat{P} , and this mode \hat{S} includes both the desired photon field mode \hat{a} and the noise mode \hat{h}^\dagger ,

$$\hat{S} = \hat{X} + i\hat{P} := \hat{a} + \hat{h}^\dagger. \quad (2.11)$$

To remove the noise mode \hat{h}^\dagger , we operate an interleaved single-shot measurement, to sweep between two cases with and without the operating pulse used for propagating-mode generation. In the first case, we measure the total mode including both the targeted mode and the noise mode. In the second case, the target mode is left in the vacuum and the measurement can be served as a reference for the noise mode, which will be used in the denoising calculation. These two cases alternate in a loop, repeated for millions of cycles.

The first-order moment of the propagating mode can be simply calculated by subtracting the noise mode from the total mode \hat{S} , and averaging over the repetition,

$$\langle \hat{a} \rangle = \langle \hat{S} - \hat{h}^\dagger \rangle = \langle \hat{S} \rangle, \quad (2.12)$$

since $\langle \hat{h}^\dagger \rangle = 0$. Extending this analysis to the second-order moment, we calculate $\langle \hat{a}^\dagger \hat{a} \rangle$ as,

$$\langle \hat{a}^\dagger \hat{a} \rangle = \langle (\hat{S} - \hat{h}^\dagger)^\dagger (\hat{S} - \hat{h}^\dagger) \rangle = \langle \hat{S}^\dagger \hat{S} \rangle - \langle \hat{S}^\dagger \hat{h}^\dagger \rangle - \langle \hat{h} \hat{S} \rangle + \langle \hat{h} \hat{h}^\dagger \rangle. \quad (2.13)$$

A more general expression for the higher-order moments can be calculated with this linear expression,

$$\langle (\hat{S}^\dagger)^m \hat{S}^n \rangle = \sum_{i,j=0}^{m,n} \binom{m}{i} \binom{n}{j} \langle (\hat{a}^\dagger)^i \hat{a}^j \rangle \langle \hat{h}^{m-i} (\hat{h}^\dagger)^{n-j} \rangle. \quad (2.14)$$

When two propagating modes measured and temporally matched, Eq. (2.14) can be extended as [110],

$$\begin{aligned} \langle (\hat{S}_1^\dagger)^{m_1} \hat{S}_1^{n_1} (\hat{S}_2^\dagger)^{m_2} \hat{S}_2^{n_2} \rangle &= \sum_{i_1, j_1, i_2, j_2=0}^{m_1, n_1, m_2, n_2} \binom{m_1}{i_1} \binom{n_1}{j_1} \binom{m_2}{i_2} \binom{n_2}{j_2} \\ &\times \langle (\hat{a}_1^\dagger)^{i_1} \hat{a}_1^{j_1} (\hat{a}_2^\dagger)^{i_2} \hat{a}_2^{j_2} \rangle \langle (\hat{h}_1^\dagger)^{m_1-i_1} \hat{h}_1^{n_1-j_1} (\hat{h}_2^\dagger)^{m_2-i_2} \hat{h}_2^{n_2-j_2} \rangle, \end{aligned} \quad (2.15)$$

where \hat{S}_1 and \hat{S}_2 are the total modes of the two propagating modes; \hat{h}_1^\dagger and \hat{h}_2^\dagger are the noise modes. From these expressions, different moments of both a single propagating mode, $\langle (\hat{a}^\dagger)^m \hat{a}^n \rangle$, and two modes, $\langle (\hat{a}_1^\dagger)^{m_1} \hat{a}_1^{n_1} (\hat{a}_2^\dagger)^{m_2} \hat{a}_2^{n_2} \rangle$, can be calculated.

2.5 Photonic-state tomography

Tomography is a technique used to reconstruct the complete information of a quantum state or process, which is essential for validating quantum systems. In superconducting qubit setups, state tomography on propagating microwave modes presents additional challenges compared to stationary qubit states due to noise photons introduced by the amplification chain in the output line, leading to direct mixing of signal and noise. In our work, temporal mode matching and interleaved measurements are necessary to denoise photonic data, as discussed in the previous section, while stationary qubit states avoid this complexity, as their measurements can target the qubit's state directly. In this section, we detail the specific methods we used to reconstruct both photonic states and processes in our system, after we have obtained the denoised moments.

2.5.1 State tomography

In this thesis, we employ three distinct techniques for quantum state tomography on the propagating modes, including least-squares (LS) optimization, compressed-sensing (CS) optimization, and gradient-descent (GD) optimization, with the moments from temporal mode matching as input. In Table 2.3, we present a comparison of the benefits associated with each method, highlighting the paper where each method is applied and clarifying whether it performs state tomography on a single propagating mode or two.

Least-squares optimization

The first method, LS optimization [100, 112], reconstructs the optimal density matrix ρ from the moments of the propagating modes by solving the following convex optimization problem,

$$\min_{\rho} \quad \left\| (\vec{\mathcal{B}} - \mathcal{A}\vec{\rho}) \right\|_{\ell_2}, \quad (2.16a)$$

$$\text{subject to} \quad \rho \geq 0, \quad (2.16b)$$

$$\text{Tr}(\rho) = 1, \quad (2.16c)$$

Table 2.3: Comparison of tomography methods, highlighting their advantages and their applications in specific papers.

Method	Advantages	Applied in
LS	Most widely-used method among the three	Paper 1 (single-mode), Paper 2 (two-mode), Paper 3 (two-mode)
CS	Suitable for heavily-reduced datasets	Paper 2 (two-mode)
GD	Allows control over the rank of the reconstructed density matrix	Paper 3 (two-mode)

where $\vec{\rho}$ in Eq. (2.16a) denotes the vectorized form of the density matrix. In this equation, $\vec{\mathcal{B}}$ is a column vector containing the experimentally measured moments ($\langle (\hat{a}^\dagger)^m \hat{a}^n \rangle$ for single-mode tomography and $\langle (\hat{a}_1^\dagger)^{m_1} \hat{a}_1^{n_1} (\hat{a}_2^\dagger)^{m_2} \hat{a}_2^{n_2} \rangle$ for two-mode tomography). The matrix \mathcal{A} , often referred to as the sensing matrix [100], is defined using the operator basis set $\{\Omega_l\}_{l=0}^{N^2-1}$ and the measurement observable set $\{\Pi_k\}_{k=0}^{M-1}$. Each component of \mathcal{A} is calculated by,

$$A_{k,l} = \text{Tr}[\Pi_k \Omega_l] = \langle j | \Pi_k | i \rangle, \quad (2.17)$$

where $\Omega_l = \Omega_{i \times N + j} = |i\rangle\langle j|$ with $i, j = 0, \dots, N-1$, and $N \times N$ is the dimension of the density matrix ρ . The measurement observables Π_k are obtained from Sec. 2.4. For single-mode tomography, they are $\Pi_k = (\hat{a}^\dagger)^m \hat{a}^n$, and for two-mode tomography, they are $\Pi_k = (\hat{a}_1^\dagger)^{m_1} \hat{a}_1^{n_1} (\hat{a}_2^\dagger)^{m_2} \hat{a}_2^{n_2}$, where the exponents m, n (and m_1, n_1, m_2, n_2) correspond to the powers of each creation and annihilation operator in the k -th measurement observable.

The term $\|\cdot\|_{\ell_2}$ represents the ℓ_2 norm (Euclidean norm), calculated as the square root of the sum of the squared components of a vector. The constraints in Eq. (2.16b-2.16c) ensure that the density matrix is completely positive (CP) and trace-preserving (TP), thus preserving its physical validity. We can also add the standard deviation $\vec{\epsilon}$ of the moments as weights in Eq. (2.16a), so that the data with larger uncertainty can weigh less in the cost function $\|(\vec{\mathcal{B}} - \mathcal{A}\vec{\rho}) \oslash \vec{\epsilon}\|_{\ell_2}$, with \oslash representing the element-wise vector division. LS optimization is a widely used method, we thus used it in all three papers in this thesis.

Compressed-sensing optimization

The mathematical formulation for CS optimization [113] is as follows,

$$\min_{\rho} \quad \|\vec{\rho}\|_{\ell_1}, \quad (2.18a)$$

$$\text{subject to} \quad \|\vec{\mathcal{B}} - \mathcal{A}\vec{\rho}\|_{\ell_2} \leq \|\vec{\epsilon}\|_{\ell_2}, \quad (2.18b)$$

$$\rho \geq 0, \quad (2.18c)$$

$$\text{Tr}(\rho) = 1, \quad (2.18d)$$

where $\|\cdot\|_{\ell_1}$ denotes the ℓ_1 norm determined by the sum of the absolute values of the vector's components. In Eq. (2.18b), the vector \vec{c} , representing the standard deviation of the moments, corresponds to the uncertainty in the measurement. All other notations match those used in LS optimization. This method is particularly advantageous when working with a heavily reduced or noisy dataset, as it allows for accurate reconstruction by exploiting the sparsity of the density matrix, like our case in Paper 2 (Sec. 3.4).

Gradient-descent optimization

The last method employed is GD-based QST, which utilizes a rank-controlled ansatz to reconstruct the density matrix. In this method, Cholesky decomposition is employed to control the rank—the number of non-zero eigenvalues—of the reconstructed density matrix, as described in [114],

$$\rho(T) = \frac{T^\dagger T}{\text{Tr}(T^\dagger T)}, \quad (2.19)$$

where T is an arbitrary complex matrix of dimensions $r \times n$, with n being the dimension of Hilbert space. The parameter r , satisfying $1 \leq r \leq n$, acts as the rank of $\rho(T)$. The loss function is thus defined as,

$$\mathcal{L}[\rho(T)] = \sum_i \left| \mathcal{B}_i - \text{Tr} \left(\Pi_i \frac{T^\dagger T}{\text{Tr}(T^\dagger T)} \right) \right|^2, \quad (2.20)$$

where $\{\Pi_i\}$ is the set of moment operators and $\{\mathcal{B}_i\}$ is the set of experimentally measured moments. In GD, we find the optimal density matrix by iteratively minimizing the loss function $\mathcal{L}[\rho(T)]$ according to,

$$T_{i+1} = T_i - \lambda \nabla \mathcal{L}[\rho(T_i)], \quad (2.21)$$

where $\nabla \mathcal{L}[\rho(T_i)]$ denotes the gradient of the loss function with respect to T at the i th iteration, and λ represents the step size, commonly referred to as the learning rate. The Cholesky parameterization ensures that the reconstructed density matrix remains valid at each iterative step and that its rank is set to the specified value r . In particular, setting $r = 1$ forces the reconstructed density matrix to be pure. We employed this approach in Paper 3 (Sec. 3.3).

2.5.2 Process tomography

We perform Quantum Process Tomography (QPT) in Paper 1 and Paper 3, to reconstruct the fidelity of the process for the generated propagating modes from a static qubit. To do that, we initialize the qubit into at least four cardinal states, and ensure that they are linearly independent. Specifically, we use the states $\{|g\rangle, \frac{1}{\sqrt{2}}(|g\rangle + |e\rangle), |e\rangle, \text{ and } \frac{1}{\sqrt{2}}(|g\rangle - i|e\rangle)\}$. Four states are sufficient because the process matrix for a single qubit has only four unknown parameters. By measuring the outcomes resulting from these input states, we can determine the effect of the process

on any arbitrary qubit state. More detailed explanations will be provided in the following paragraphs.

After the state initialization, we then transfer the quantum state from the qubit to propagating modes and perform QST on these modes for each initial state, separately. Using the four reconstructed density matrices as input, we employ the Kraus-operator formalism to represent the quantum process [115, 116],

$$\rho_{\text{out}} = \Lambda(\rho_{\text{in}}) = \sum_{m,n=0}^{d^2-1} \chi_{mn} \sigma_m \rho_{\text{in}} \sigma_n^\dagger, \quad (2.22)$$

where $\Lambda(\cdot)$ represents the quantum map of the process. The process matrix χ characterizes Λ , and χ_{mn} are the elements of the matrix. The set $\{\sigma_i\}$ comprises fixed basis operators, specifically the Pauli operators: $\{\sigma_0, \sigma_1, \sigma_2, \sigma_3\} = \{I, \sigma_X, \sigma_Y, \sigma_Z\}$ [Eq. (1.11)]. In our case, we have the dimension of the process matrix to be $d = 2^n$, with n the dimension of the Hilbert space. In both Paper 1 and Paper 3, we encode the quantum state from a superconducting qubit into propagating modes. In Paper 1, the state is encoded into a single propagating mode as $\alpha|0\rangle + \beta|1\rangle$, with two-dimensional Hilbert space and resulting in a 4×4 process matrix χ . For Paper 3, the same state is encoded into two propagating modes as $\alpha|10\rangle + \beta|01\rangle$, where the quantum information is confined to a two-dimensional subspace of the four-dimensional Hilbert space. Consequently, the process matrix χ remains 4×4 in this case, as only the subspace spanned by $|10\rangle$ and $|01\rangle$ carries the relevant quantum information used in the QPT analysis.

Using Eq. (2.22) with the four cardinal states (input probe states) and corresponding photonic states (output states) we can form a system of linear equations of the form $\mathcal{M}\vec{\chi} = \vec{\mathcal{D}}$, where $\vec{\mathcal{D}}$ is constructed from ρ_{out} and $\vec{\chi}$ represents the vectorized form of the χ matrix. The coefficient matrix \mathcal{M} —analogous to the sensing matrix \mathcal{A} in Eq. (2.16a)—depends solely on the set of probe states and measurement observables; in our case, the cardinal states and the moment operators. The method to reconstruct \mathcal{M} can be found in [117].

To calculate a physically valid χ matrix characterizing an underlying CPTP map, we formulate an LS optimization problem, similar to that in QST,

$$\min_{\chi} \quad \left\| (\vec{\mathcal{D}} - \mathcal{M}\vec{\chi}) \right\|_{\ell_2}, \quad (2.23a)$$

$$\text{subject to} \quad \chi \geq 0, \quad (2.23b)$$

$$\sum_{m,n=0}^3 \chi_{mn} \sigma_m \sigma_n = I, \quad (2.23c)$$

where Eq. (2.23b) ensures the complete positivity (CP) of the process, and Eq. (2.23c) enforces the trace-preserving (TP) condition.

We encode the quantum state from a superconducting qubit into propagating modes in both papers, so they share the same ideal process matrix (χ), which characterizes a perfect identity channel that preserves the quantum state during the encoding process. For such an ideal state-preserving process, the χ matrix expected

to be $\chi_{\text{ideal}} = \begin{bmatrix} 1 & 0 & 0 & 0 \\ 0 & 0 & 0 & 0 \\ 0 & 0 & 0 & 0 \\ 0 & 0 & 0 & 0 \end{bmatrix}$. However, in Paper 1, we use the Pauli transfer matrix

(R) to denote the process, which is another common representation of the process, and can be transferred from χ as [115],

$$R = \sum_{m,n=0}^3 \chi_{m,n} (\sigma_m \otimes \sigma_n). \quad (2.24)$$

In our case, the Pauli transfer matrix is expected to be $R_{\text{ideal}} = \begin{bmatrix} 1 & 0 & 0 & 0 \\ 0 & 1 & 0 & 0 \\ 0 & 0 & 1 & 0 \\ 0 & 0 & 0 & 1 \end{bmatrix}$.

2.5.3 Analysis of the reconstructed matrix

The fidelity between the reconstructed state and the target state is defined as [118]

$$F(\rho_{\text{ideal}}, \rho) = \left(\text{Tr} \sqrt{\sqrt{\rho_{\text{ideal}}} \rho \sqrt{\rho_{\text{ideal}}}} \right)^2, \quad (2.25)$$

where ρ_{ideal} is the target density matrix and ρ is the reconstructed density matrix from the measurement. This formula similarly applies to the process matrix obtained through QPT,

$$F(\chi_{\text{ideal}}, \chi) = \left(\text{Tr} \sqrt{\sqrt{\chi_{\text{ideal}}} \chi \sqrt{\chi_{\text{ideal}}}} \right)^2, \quad (2.26)$$

with χ_{ideal} (χ) the target (experimentally obtained) process matrix. Additionally, the purity P of a density matrix ρ is given by,

$$P = \text{Tr}(\rho^2). \quad (2.27)$$

The contributors to infidelity in our system are the coherent and incoherent errors:

- **Coherent errors:** These result from factors such as miscalibration of the π -pulse, template mismatching, and other systematic imperfections in control operations. Coherent errors can be mitigated by refining characterization methods, applying precise modelling, and implementing optimal control techniques [119, 120].
- **Incoherent errors:** These are primarily due to the decoherence of the qubits and the coupler, including T_1 and T_2 decay, thermal excitation in the qubit state, and noise from the environment. We can reduce the effects of decoherence by eliminating sources of decoherence during sample fabrication and loading, or by applying faster pulses to minimize interaction time and outrun the decoherence. Thermal excitation can be mitigated through active or passive qubit reset [121, 122].

Chapter 3

Experiments

This chapter presents experiments from the three appended papers. In Sec. 3.1, we demonstrate deterministic quantum state transfer from a superconducting qubit to a propagating microwave mode, by encoding the qubit as a superposition of vacuum and single-photon Fock states. Although photon shaping enables reabsorption to be a time-reversed process of the emission (Sec. 3.2), photon loss remains a major challenge in distributed quantum networks. To address this (Sec. 3.3), we propose frequency-bin encoding by deterministically encoding qubit information into two simultaneous photonic modes at different frequencies, enabling effective error detection by excluding the vacuum state. Finally, in Sec. 3.4, we generate entangled photonic modes by continuously driving a quantum emitter, showing that temporally filtered sideband modes are entangled.

3.1 Deterministic single-rail photon emission

Deterministic emission of microwave single photons is an important building block for realizing distributed quantum computing. In this section, we explain the experiment to encode quantum information from a superconducting qubit into a single-rail microwave photon [Paper 1], specifically the transformation $(\alpha |g\rangle + \beta |e\rangle) \otimes |0\rangle \rightarrow |g\rangle \otimes (\alpha |0\rangle + \beta |1\rangle)$. Here, $\alpha |g\rangle + \beta |e\rangle$ represents an arbitrary qubit state, with $|g\rangle$ and $|e\rangle$ denoting the ground and excited states of the qubit, respectively, while $|0\rangle$ and $|1\rangle$ are the photon number states corresponding to the vacuum and single-photon states of the emitted photon, the propagating mode.

Figure 3.1 shows the structure of the device for emitting single-rail photons. We have a qubit, referred to as the emitter qubit, that is strongly coupled to a coplanar waveguide, enabling the encoding of quantum states from superconducting qubits into emitted microwave photons. While this strong coupling facilitates efficient photon emission and absorption, it presents challenges in preparing the quantum state using the emitter qubit alone. To address this issue, we introduce an additional qubit, referred to as the data qubit, for state preparation. The data qubit and the emitter qubit are interconnected via a flux-tunable coupler, allowing on-demand population transfer between the two qubits via an iSWAP-like operation.

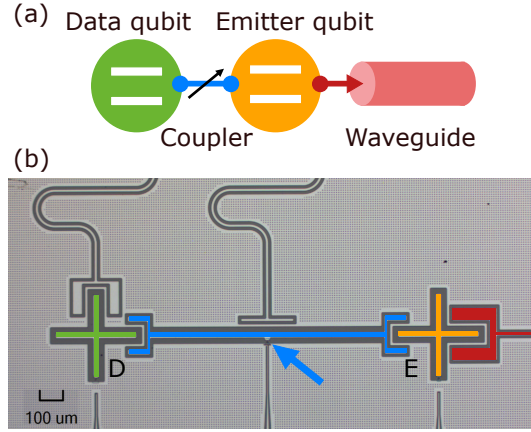


Figure 3.1: Setup for single-rail photon emission. (a) Schematic diagram of the device designed for generating single-rail photon emission. (b) False-color optical micrograph of the device.

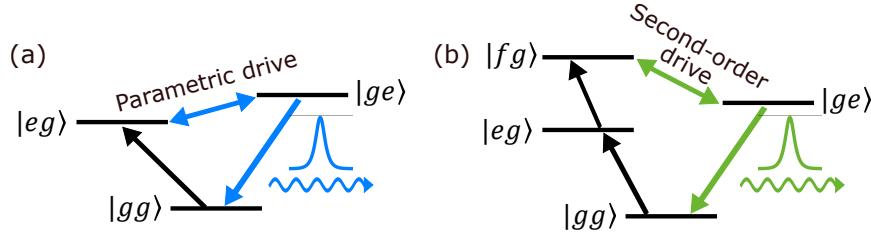


Figure 3.2: Two distinct methods for achieving single-rail photon emission using the device in Fig. 3.1, (a) by applying a parametric drive to the coupler qubit, and (b) by inducing a second-order transition drive on the data qubit.

With this structure, there are two methods to map quantum information from the qubit state to the photon state. The first method uses a parametric drive to induce an excitation-preserving transition between the excited states of two qubits [Fig. 3.2(a)]. The second method involves a second-order transition between the qubit's second excited state ($|f\rangle$) and ground state ($|g\rangle$), in a process that is not excitation-preserving [Fig. 3.2(b)]. These two methods are described in detail in the following.

3.1.1 Method 1 – Parametric drive emission

In Method 1, single-rail photons are emitted by applying a parametric drive to the coupler [Fig. 3.2(b)]. In this case, the coupler, built with a flux-tunable transmon, is a special qubit that we do not read out. The state to be transferred is initially prepared in the data qubit as $\alpha|g\rangle + \beta|e\rangle$. The parametric drive is then applied through the coupler's flux line, implementing an iSWAP-type gate between the qubits (referred to as iSWAP-type rather than iSWAP because the dissipation channel prevents the gate from swapping the excitation back, making it a one-way operation). This operation transfers the excitation from the data qubit to the emitter qubit, leaving the data qubit in the ground state while the emitter qubit enters the superposition state

$\alpha|g\rangle + \beta|e\rangle$. The emitter qubit simultaneously decays into the waveguide, emitting a photon in the state $\alpha|0\rangle + \beta|1\rangle$ as the qubit returns to its ground state. This transition is the same one used in our work [Paper 1] and in references [39, 40].

Theoretical model

The photon emission process results from both the system's Hamiltonian and its effective non-Hermitian Hamiltonian, which account for dissipative interactions and decoherence mechanisms. In the entire photon emission process, the coupler remains nearly unexcited, and we work in the dispersive regime where $\Delta \gg g$, with Δ the detuning between the coupler and the qubits and g the coupling rate. As a result, the static Hamiltonian of the simplified system, consisting only of the two qubits, is given by [39],

$$\frac{H}{\hbar} = \underbrace{\frac{1}{2}\omega_D\hat{\sigma}_D^Z}_{\text{Data qubit}} + \underbrace{\frac{1}{2}\omega_E\hat{\sigma}_E^Z}_{\text{Emitter qubit}} + \underbrace{J_{dc}(\hat{\sigma}_D^+\hat{\sigma}_E^- + \hat{\sigma}_D^-\hat{\sigma}_E^+)}_{\text{Coupling}}, \quad (3.1)$$

where ω_D and ω_E are the angular frequency of the data and emitter qubits, and J_{dc} is the coupling strength between the data and emitter qubits,

$$J_{dc}(\Phi_{dc}) = \frac{g_D g_E}{2} \left(\frac{1}{\Delta_D} + \frac{1}{\Delta_E} \right), \quad \Delta_i = \omega_C(\Phi_{dc}) - \omega_i, \quad (3.2)$$

with $i = D, E$. The coupler frequency ω_C follows a square-root cosine dependence on the applied dc flux, as described in Eq. (1.21). g_D (g_E) is the coupling strength between the data (emitter) qubit and the coupler.

To operate the iSWAP-type gate between the qubits, we apply an ac sinusoidal flux pulse to the coupler, on top of the dc flux bias,

$$\Phi(t) = \Phi_{dc} + \underbrace{A\cos(\omega_m t)}_{\Phi_{ac}(t)}, \quad (3.3)$$

with $\omega_m = |\omega_D - \omega_E|$, compensating the frequency detuning between the qubits. By Taylor expanding the ac flux term and working in a rotating frame of the qubit frequencies, the Hamiltonian becomes [39],

$$\frac{\hat{H}}{\hbar} = \frac{A}{2} \frac{\partial J_{dc}(\Phi)}{\partial \Phi} (\hat{\sigma}_D^X \hat{\sigma}_E^X + \hat{\sigma}_D^Y \hat{\sigma}_E^Y). \quad (3.4)$$

Thus, the effective coupling between the two qubits, denoted as J , is proportional to both the driving strength A and the slope of the coupling tuning curve.

Upon considering the decay rate of the emitter qubit and the two qubits in the rotating frame, we obtain an effective non-Hermitian Hamiltonian,

$$\hat{H}_{\text{eff}}/\hbar = \begin{pmatrix} 0 & J \\ J & -i\Gamma_E/2 \end{pmatrix}. \quad (3.5)$$

The radiative decay rate of the amplitude, rather than the power, is taken into account in the element of the emitter qubit by using $\Gamma_E/2$.

We start by preparing the data qubit in the state $\alpha|g\rangle + \beta|e\rangle$ and the emitter qubit in the ground state, $|\Psi(0)\rangle = \alpha|g, g\rangle + \beta|e, g\rangle$, where α and β are complex coefficients satisfying $|\alpha|^2 + |\beta|^2 = 1$. After evolving for time t , the state of the data qubit becomes,

$$|\Psi(t)\rangle = e^{-i\frac{\hat{H}_{\text{eff}}t}{\hbar}}|\Psi(0)\rangle. \quad (3.6)$$

The expected output field $\langle\hat{a}_{\text{out}}(t)\rangle$ of the emitted photon from the emitter qubit can thus be calculated by,

$$\begin{aligned} \langle\hat{a}_{\text{out}}(t)\rangle &= \sqrt{\Gamma_E} \langle g, e | \Psi(t) \rangle \\ &= -\frac{2i\beta}{\sqrt{-16J^2 + \Gamma_E^2}} \left(e^{-t(\Gamma_E - \sqrt{-16J^2 + \Gamma_E^2})/4} - e^{-t(\Gamma_E + \sqrt{-16J^2 + \Gamma_E^2})/4} \right). \end{aligned} \quad (3.7)$$

We will discuss more regarding this expression, in connection with the experimental results.

Photon emission

The photon emission is facilitated by driving the coupler parametrically, which induces an excitation exchange between qubits. As shown in Eq. (3.2) and (3.3), we apply both dc and ac flux to the coupler. The dc flux adjusts the coupler frequency from its sweet spot, the highest frequency, toward the frequencies of the two qubits, which enhances the coupling between the qubits. When selecting the dc flux, we balance the following trade-offs: Increasing Φ_{dc} lowers the coupler's frequency, bringing it closer to the qubit modes and thereby enhancing the coupling rate between the qubits. However, if Φ_{dc} becomes too large, the Purcell decay of the data qubit may increase due to the high decay rate of the emitter qubit. Taking both factors into account, we opted to shift the coupler frequency from its highest value, the sweet spot 7.735 GHz, to approximately 6 GHz (see Sec. 5.2.2 for the Purcell decay analysis at this point), while the data and emitter qubits have fixed frequencies at 4.771 GHz and 4.953 GHz, respectively (Fig 3.3).

The ac flux pulse, the parametric drive added on the dc flux bias, is a sinusoidal wave modulated by an envelope $A(t)$,

$$\Phi_{\text{ac}}(t) = A(t) \cos(\omega_m t) \quad (3.8)$$

Once the ac flux tone is applied, the population in the data qubit starts to transfer to the emitter qubit and decays into the waveguide, thus we can characterize the pulse by measuring the emitted photon field from the waveguide.

We first analyze the case where the ac flux pulse envelope, $A(t)$, remains constant over time, resulting in a square pulse shape. We initialize the data qubit in the state $\frac{1}{\sqrt{2}}(|g\rangle + |e\rangle)$, and then apply the parametric drive to the coupler. We implement three different drive amplitudes in the modulation pulse, ranging from low to high, and measure the amplitude of the emitted photons, $|\hat{a}_{\text{out}}(t)|$ (Fig. 3.4). The amplitude of the photon field exhibits a fast initial increase followed by an exponential decay, which can be described as Eq. (3.7), the difference between two exponential decays. Initially,

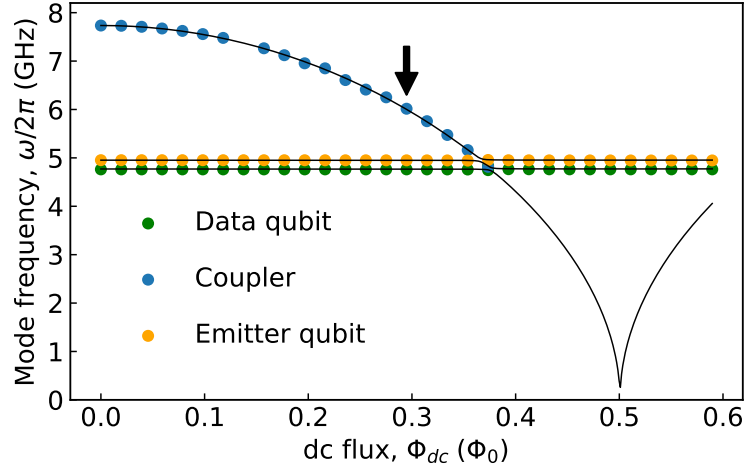


Figure 3.3: Mode frequencies of the data and emitter qubits, and the coupler as a function of the applied dc flux, Φ_{dc} . Φ_{dc} is in the unit of one flux quanta Φ_0 , which is calibrated by measuring the coupler resonator while sweeping the applied flux (see Sec. 5.2.1 for details). The solid curves are the theoretical prediction of the mode frequencies. The black arrow in the figure marks the operating point of the coupler.

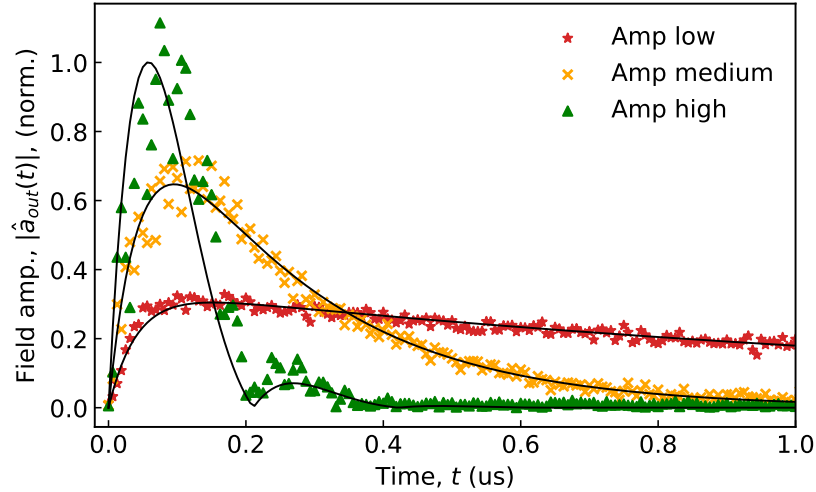


Figure 3.4: The amplitude of the emitted photon output field, when the data qubit is initialized in an equal superposition state of the ground and excited states. The applied parametric flux pulse to the coupler has a constant driving amplitude over time. We present three different cases with different driving amplitudes. The solid black curves represent theoretical fits to the data using Eq. (3.7), with the coupling strength between qubits, J , as the only adjustable parameter.

when t is near 0, the dominant decay occurs at a rate of $\frac{1}{4}(\Gamma_E + \sqrt{-16J^2 + \Gamma_E^2})$. However, over longer durations, the decay rate of $\frac{1}{4}(\Gamma_E - \sqrt{-16J^2 + \Gamma_E^2})$ becomes more dominant and ultimately defines the photon field amplitude's decay rate.

In the third scenario (green curve in Fig. 3.4), a second peak emerges because the Rabi oscillation between the two qubits becomes more dominant than their emission into the waveguide. This regime is less relevant to our purpose, since our aim is to route the excitation into the waveguide. The maximum coupling rate J to stay below this region can be obtained from Eq. (3.7), with $\Gamma_{\text{eff}} = \frac{1}{4}(\Gamma_E - \sqrt{-16J^2 + \Gamma_E^2})$. From this expression, we deduce that the effective decay rate simplifies to $\Gamma_{\text{eff}} = 4J^2/\Gamma_E$ when $J \ll \Gamma_E$. The fastest effective decay rate $\Gamma_{\text{eff}} = \Gamma_E/2$ is reached when $J = \Gamma_E/4$. For $J > \Gamma_E/4$, a second peak in the emitted photon field starts to appear. In later measurements, we always stay at lower coupling $J \leq \Gamma_E/4$. The relation between J and the applied ac flux amplitude is shown in Fig. 3.5, obtained by fitting the photon amplitude curves.

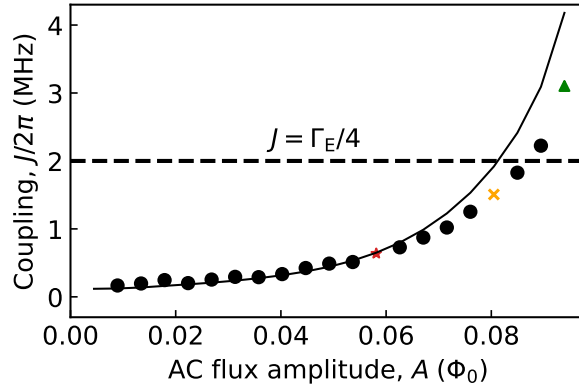


Figure 3.5: The coupling J between the qubits as a function of the parametric drive modulation amplitude, extracted from the fits to photon amplitude curves using Eq. (3.7). The red, yellow and green points correspond to the three curves shown in Fig. 3.4. The solid curve represents the expected values from the theoretical model, while the dashed line indicates the maximum coupling rate beyond which Rabi oscillations between the qubits become more prominent than the emission.

In summary, we employ a coupler parametric drive to facilitate the state exchange between the qubits. This ac flux pulse is similar to an iSWAP gate; however, different from an iSWAP gate, the state cannot be swapped from the emitter qubit back to the data qubit due to the photon decaying into the waveguide. Moreover, by modulating the strength of the ac flux drive, we can adjust the coupling rate between the two qubits, ultimately allowing us to control the temporal envelope of the emitted photon, which will be explained in Sec. 3.2.

Moments of the single-rail photon

By applying temporal mode matching to the emitted photon as described in Sec. 2.4, we obtain selected-order moments of the output field. We prepare our data qubit in different superposition states $\alpha |g\rangle + \beta |e\rangle$, parameterized by the Rabi angle θ , where

$\alpha = \cos(\theta/2)$ and $\beta = \sin(\theta/2)$, and then apply the parametric drive [Fig. 3.6(a)]. When the data qubit is prepared in an equal superposition of ground and excited states ($\theta = \pi/2$), the first-order moment $\langle \hat{a} \rangle$, representing the mean field amplitude, reaches its maximum value [blue curve in Fig. 3.6(b)]. When the data qubit is prepared in the fully excited state ($\theta = \pi$), corresponding to the emission of a full photon, the second-order moment $\langle \hat{a}^\dagger \hat{a} \rangle$, representing the mean photon number, reaches its maximum [orange curve in Fig. 3.6(b)]. However, at this point, the mean photon amplitude $\langle \hat{a} \rangle$ is zero because the emitted state is a statistical mixture with zero coherence (the off-diagonal elements in the density matrix are zero), leading to a zero amplitude measurement. The fourth-order moment $\langle \hat{a}^\dagger \hat{a}^\dagger \hat{a} \hat{a} \rangle$ is expected to be zero for all θ since a single photonic mode is emitted.

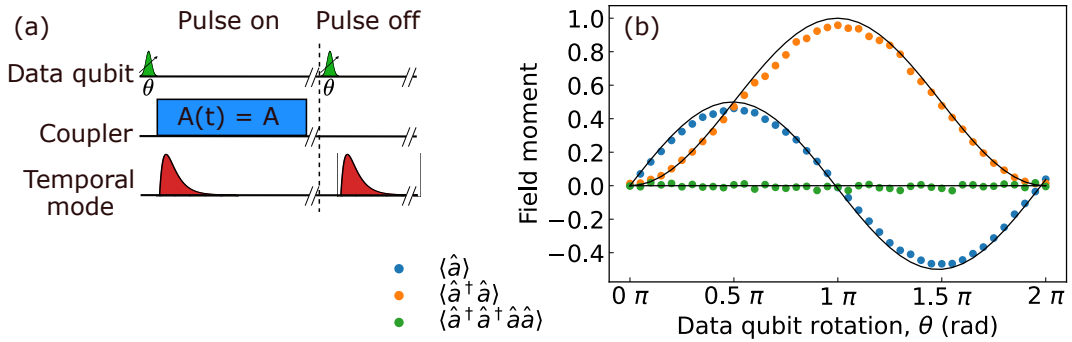


Figure 3.6: (a) Pulse sequence used for measuring the moments of the propagating mode. The measurement is done interleavedly by sweeping between two cases, with and without the parametric drive. (b) The first-, second-, and fourth-order moments of the output field of the emitted photon in the single rail, plotted as functions of the Rabi angle θ used to initialize the data qubit. The solid curves represent the ideal theoretical values, which are $\sin(\theta)/2$, $\sin(\theta/2)^2$ and 0 for the three moments respectively.

The normalized Glauber second-order correlation function at zero time delay is defined as,

$$g^{(2)}(0) \equiv \frac{\langle \hat{a}^\dagger \hat{a}^\dagger \hat{a} \hat{a} \rangle}{\langle \hat{a}^\dagger \hat{a} \rangle^2}, \quad (3.9)$$

which is measured to be 0.024 ± 0.027 for the state $\frac{1}{\sqrt{2}}(|0\rangle + |1\rangle)$ and -0.01 ± 0.001 for the state $|1\rangle$. These values are very close to zero within experimental uncertainties, indicating that the probability of simultaneously detecting two photons is negligible. This demonstrates that both states exhibit strong antibunching behaviour, confirming that the multiphoton component is significantly suppressed compared to the single-photon component.

The moments are normalized under the assumption that when the parametric drive is activated, the decay of the data qubit occurs through two independent channels: the detected mode of the waveguide and the intrinsic loss mechanisms of the data qubit, with decay rates Γ_{eff} and Γ_D^{ge} , respectively. Accordingly, when the data qubit is initialized in state $|e\rangle$ with $\theta = \pi$, we assume that the second-order moment is,

$$\langle \hat{a}^\dagger \hat{a} \rangle = \frac{\Gamma_{\text{eff}}}{\Gamma_{\text{eff}} + \Gamma_D^{ge}}, \quad (3.10)$$

where $\Gamma_{\text{eff}} = \Gamma_E/2$ is the effective decay rate of the emitted photon into the waveguide mode, and Γ_D^{ge} is the longitudinal relaxation rate of the data qubit due to intrinsic losses, calculated as $\Gamma_D^{ge} = 1/T_1^{ge} = 35$ kHz.

3.1.2 Method 2 – Second-order transition emission

The second approach for single-rail photon emission leverages the multi-level structure of the qubits. As illustrated in Fig. 3.2(b), the data qubit is first transferred from the arbitrary state $\alpha|g\rangle_D + \beta|e\rangle_D$ to $\alpha|g\rangle_D + \beta|f\rangle_D$, by accessing the second excited state $|f\rangle_D$. Subsequently, a second-order drive is applied between the states $|f\rangle_D|g\rangle_E$ and $|g\rangle_D|e\rangle_E$ via the charge line of the data qubit, facilitating the transfer of the data qubit's state from $\alpha|g\rangle_D + \beta|f\rangle_D$ to the emitter qubit's state $\alpha|g\rangle_E + \beta|e\rangle_E$. Due to the emitter qubit's strong coupling to the waveguide, it immediately decays to the ground state in a coherent way, deterministically emitting a photon with state $\alpha|0\rangle + \beta|1\rangle$ into the waveguide. This type of transition is consistent with the Raman process described in [25, 35, 52, 53].

Building on this described method, we make a slight modification in our experiments by transferring between different states while still utilizing the second-order transition. Specifically, instead of driving transitions directly between $|f\rangle_D|g\rangle_E$ and $|g\rangle_D|e\rangle_E$, we drive transitions between $|f\rangle_D$ and one of the hybridized modes coupled to the waveguide, denoted as $|S\rangle$ with frequency ω_S . This hybridized mode is formed by the coupling between the coupler and the emitter qubit. This approach yields results similar to transferring the state to the bare excited state of the emitter qubit $|e\rangle_E$, but with differences in the mode frequency and the decay rate into the waveguide. The reason for this adjustment, including a detailed explanation of the hybridized modes, will be discussed further in Sec. 3.3.

Photon emission

The second-order transition drive applied to the data qubit induces an ac Stark shift in the qubit's frequency [25]. The stark shift at different driving strengths ζ can be measured through the population of the data qubit in the state $|f\rangle_D$, while applying the second-order-transition drive with different frequencies and strengths (Fig. 3.7). The reduction of the population of the data qubit in $|f\rangle_D$ indicates the transition of the excitation into the propagating modes. As the drive strength increases, the dip is broadened, as well as becomes smaller in frequency compared to the dip frequency with low driving amplitude, $\omega_D^{ge} + \omega_D^{ef} - \omega_S$ due to the Stark shift.

After accounting for the ac-Stark shift at various drive amplitudes, we adjust the drive frequency accordingly and measure the emitted photon output field. Again, we present the amplitude photon output field, $|\hat{a}_{\text{out}}(t)|$, with various constant driving amplitudes over time (Fig. 3.8). By temporal mode matching the emitted photon, the moments can be derived in the same manner as for the parametric drive (Sec. 3.1.1), yielding similar results. Therefore, we do not repeat a similar plot as Fig. 3.6.

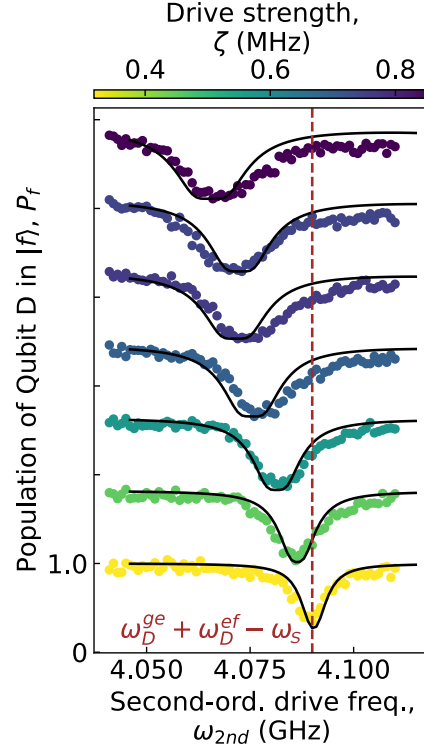


Figure 3.7: The population of the data qubit in state $|f\rangle_D$, while sweeping the frequency and amplitude of the second-order-transition drive. The filled circles represent the measured data and the solid black curve is the fitting from numerical simulation. The dips in each curve indicate the optimal drive frequency to use for the corresponding drive amplitude. Each curve is offset by 0.82 compared to the curve below it.

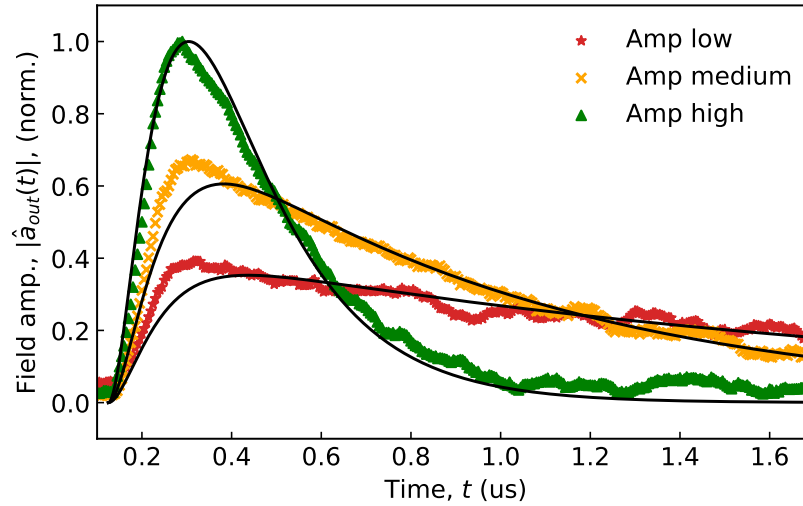


Figure 3.8: The amplitude of the emitted photon output field when the data qubit is initialized in an equal superposition of the ground ($|g\rangle_D$) and second-excited ($|f\rangle_D$) states, followed by the application of a second-order-transition pulse. The figure presents three different cases corresponding to different driving amplitudes of the second-order transition pulse. The solid black curves represent the theoretical model.

3.2 Photon shaping to facilitate reabsorption

To facilitate potential photon reabsorption in a receiver quantum node, we explore photon shaping during the emission process. Photon shaping is crucial because, with a constant amplitude in the photon emission drive, the emitted photon profile initially exhibits a rapid rise, followed by an exponential decay. However, for future reabsorption by an identical quantum processor, the process should ideally be the time-reverse of the emission, meaning the photon's shape would need to be exponentially increasing, demanding a lot from the receiver side. By dividing the reshaping process for achieving a time-reversed shape equally between the emitter and receiver nodes, the entire process transforms into emitting a time-symmetric photon from one quantum processor and receiving an exponentially increasing photon at the other, by replicating the emission process in reverse (Fig. 3.9). According to [34], theoretically, transmitting a time-symmetric photon, compared to without photon shaping, can increase the reabsorption efficiency from 54% to over 99%.

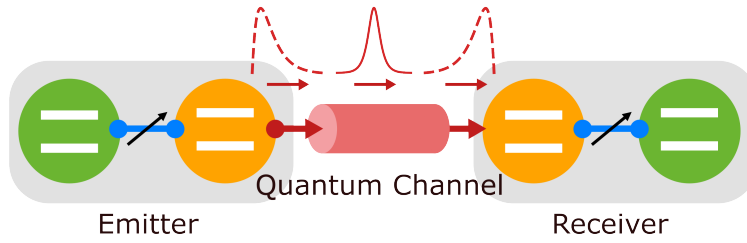


Figure 3.9: The reshaping process in a distributed QC system including quantum circuits for both photon emission and reabsorption.

Reshaping the photon envelope involves adjusting both the photon's amplitude and phase to achieve time symmetry. In this section, we present our method for accomplishing both, based on parametric-drive photon emission as explained in Sec. 3.1.1. The photon's amplitude is reshaped into a symmetric profile, by tuning the amplitude of the parametric flux drive applied to the coupler. The photon phase is compensated to remain nearly zero over time using the I and Q quadratures of the parametric drive, thereby achieving the time-symmetric shape.

3.2.1 Photon envelope reshaping

In this section, we detail the process of shaping the photon amplitude. As previously mentioned, the photon emission rate is governed by the strength of the ac flux pulse driving the coupler. Thus, in principle, an arbitrary photon shape can be realized by defining the ac flux pulse as a time-dependent function. For instance, by controlling the pulse to emit more slowly at the beginning and more rapidly later, we can control the profile of the emitted photon accordingly.

To achieve the desired photon shaping, we first select the target shape for the photon envelope. We aim for a hyperbolic cosine profile, $1/\cosh(t/\tau)$, where τ represents the timescale of photon emission. A shorter τ results in faster photon emission into the waveguide. Based on this choice, the corresponding expression

for the coupler pulse is then back-calculated [109], resulting in the derived pulse function,

$$A(t) = \frac{\Gamma_{\text{eff}}}{4\cosh(\Gamma_{\text{eff}}t/2)} \frac{1 - e^{\Gamma_{\text{eff}}t} + (1 + e^{\Gamma_{\text{eff}}t})\Gamma_E/\Gamma_{\text{eff}}}{\sqrt{(1 + e^{\Gamma_{\text{eff}}t})\Gamma_E/\Gamma_{\text{eff}} - e^{\Gamma_{\text{eff}}t}}}, \quad (3.11)$$

which leads to the desired shape of the emitted photon,

$$f(t) = \frac{\sqrt{\Gamma_{\text{eff}}}}{2 \cosh(\Gamma_{\text{eff}}t/2)}, \quad (3.12)$$

indicating that the timescale of the photon profile is given by $\tau = 1/\Gamma_{\text{eff}}$. In this expression, we set the effective decay rate $\Gamma_{\text{eff}}/2\pi \approx 0.5\Gamma_E/2\pi = 4\text{ MHz}$. The chosen Γ_{eff} corresponds to the maximum emission rate to encode information from the data qubit into the propagating mode for this device (see Sec. 3.1.1 for the derivation). Exceeding this value would result in the emergence of a secondary peak in the emitted photon amplitude, caused by Rabi oscillations between the qubits becoming more dominant than photon emission, as demonstrated in the previous Sec. 3.1.1. Subsequent research has explored alternative approaches for reshaping flying qubits, including methods like gradient-descent optimization [123] and reinforcement learning [33], which build upon and extend the reshaping techniques used in this work.

By adjusting the coupler's ac flux pulse from a square template to the custom template given by Eq. (3.11), we reshape the emitted photon from an exponentially decaying profile [Fig. 3.10(a)] to a time-symmetric one [Fig. 3.10(b)]. We obtain $\tau = 50.5\text{ ns}$ from the fitting, which is close to the fastest case that can be achieved with $\Gamma_{\text{eff}} = \Gamma_E/2$. An additional advantage of this custom pulse with Eq. (3.11) is its long tail, which ensures a complete reset of the qubit.

We assess the symmetry of the emitted photon $\hat{a}_{\text{out}}(t)$ using the parameter s , defined as [35],

$$s = \max_{t_0} \frac{\int |\langle \hat{a}_{\text{out}}(2t_0 - t) \rangle^* \langle \hat{a}_{\text{out}}(t) \rangle| dt}{\int |\langle \hat{a}_{\text{out}}(t) \rangle|^2 dt}, \quad (3.13)$$

which computes the overlap between the photon wavepacket and its time-reversed counterpart. The parameter t_0 represents a reference time that is swept to find the optimal time-reversed wavepacket to maximize the overlap. This parameter allows us to verify whether the photon envelope $\langle \hat{a}_{\text{out}}(t) \rangle$ is indeed time-symmetric. A fully symmetric photon envelope will result in $s = 1$. However, we observe a decrease in the s parameter. This result, unexpected if we only consider the envelope of the signal, can be attributed to the presence of a time-varying phase within the system. Achieving time symmetry in the photon requires not only a symmetric amplitude but also a symmetric phase in the emitted photon. We will discuss this phase symmetry requirement and implementation in more detail in the next section.

3.2.2 Photon phase compensation

In this section, we outline the process for compensating the time-varying phase to achieve a time-symmetric phase profile. We choose to bring it to zero over time,

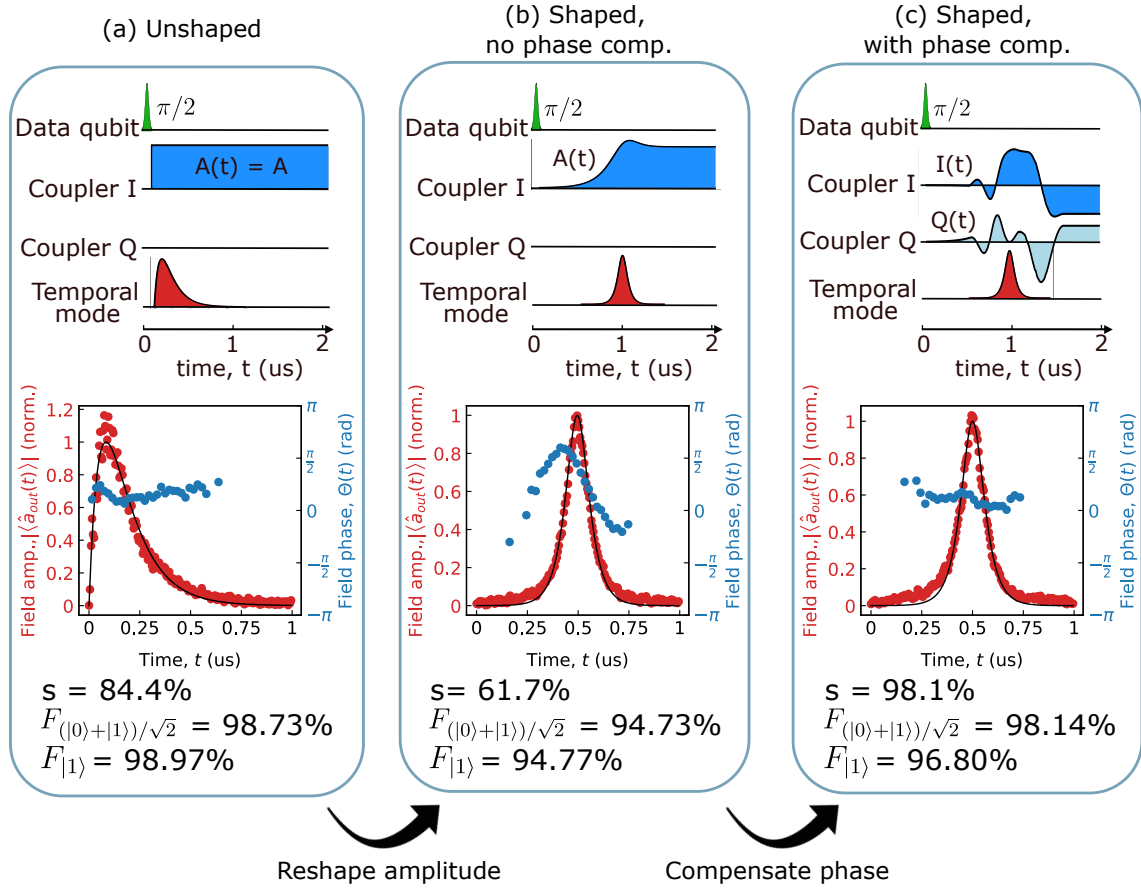


Figure 3.10: The pulse sequence for the photon generation and the emitted photon output field, including both the photon amplitude and the phase. Here we present the results for three different cases: (a) unshaped, (b) shaped but without phase compensation, and (c) shaped with phase compensation. We also show the symmetry parameter s and the fidelity F after reconstructing the density matrix through quantum state tomography. For each case, the measurement is done interleavedly by sweeping between two cases, with and without the parametric drive, but is not shown in the pulse sequence for simplicity.

which is a straightforward case of achieving time-symmetric. Before delving into the compensation method, we first discuss the source of the time-variation in the phase observed in Fig. 3.10(b). As shown in Fig. 3.3 and explained in Sec. 3.1.1, a parametric flux pulse is introduced at the selected dc flux operating point. When shaping the photon, this parametric pulse slowly varies in amplitude over time, causing a varying shift in the coupler's mean frequency due to the nonlinear flux-frequency relationship. Because of the coupling between the coupler and the qubits, the qubit frequencies also vary over time [124]. The varying qubit frequencies lead to a phase shift in the emitted photon, whose frequency is determined by the sum of the varying data qubit frequency and the constant frequency of the parametric drive applied to the coupler. The phase variation over time is denoted as $\Theta(t) = \arg[\langle \hat{a}_{\text{out}}(t) \rangle]$. To solve this slow variation of phase, in principle, we can make the frequency of the parametric pulse ω_m dependent on the amplitude $A(t)$, resulting in an ac flux pulse dependent on

time, given by,

$$\Phi_{ac}(t) = A(t) \cos [\omega_m(t) t] . \quad (3.14)$$

In our work, we achieve simultaneous temporal variation of both the pulse amplitude and frequency by encoding the frequency shift information into the I and Q quadratures of the coupler's parametric drive using vector modulation. This process begins by decomposing the time-dependent frequency $\omega_m(t)$ into two parts: one that remains constant at our fixed coupler drive frequency ω_m , and the other that varies with time $\delta\omega(t)$. The pulse can then be split into I and Q components,

$$\begin{aligned} \Phi_{ac}(t) &= A(t) \cos [\omega_m(t) t] , \\ &= A(t) \cos [(\omega_m + \delta\omega_m(t)) t] , \\ &= A(t) \left[\cos (\omega_m t) \cos (\delta\omega_m(t) t) - \sin (\omega_m t) \sin (\delta\omega_m(t) t) \right] , \\ &= \underbrace{A(t) \cos (\delta\omega_m(t) t)}_{I(t)} \cos (\omega_m t) + \underbrace{A(t) \sin (\delta\omega_m(t) t)}_{Q(t)} \cos \left(\omega_m t + \frac{\pi}{2} \right) . \end{aligned} \quad (3.15)$$

Thus, the original ac flux pulse in Eq. (3.8), which consists of only one quadrature, can be decomposed into a pulse with the same high frequency component ω_m but containing two slowly varying quadratures, I and Q, with a $\pi/2$ phase shift between them. The two quadratures in the coupler parametric drive, $I(t)$ and $Q(t)$, can be used to compensate for the varying phase [$\Theta(t)$ in Fig. 3.10(b)], through the encoding process as,

$$I(t) = A(t) \cos \left(-2\pi \Theta(t) \right) , \quad (3.16)$$

$$Q(t) = A(t) \sin \left(-2\pi \Theta(t) \right) . \quad (3.17)$$

Any linear phase roll in $\Theta(t)$ can be moved by a shift of the high-frequency component $\omega_m \rightarrow \omega_m + \omega_{roll}$.

After applying the phase-compensation approach, we obtained nearly a constant phase over time, while maintaining the photon amplitude unchanged [Fig. 3.10(c)]. The symmetry of the emitted photon increased from 69% to 98%. The fidelity of shaped, phase-compensated photons is slightly lower than that of unshaped photons. This reduction is primarily due to coherent errors introduced by time-dependent pulse operations and the longer time delays associated with shaped photons, as there is more decay of the data qubit during this period. For this phase compensated case, we perform quantum process tomography (QPT) (Sec. 2.5.2) by preparing the data qubit in the six cardinal states, $|g\rangle$, $|e\rangle$, $(|g\rangle + |e\rangle)/\sqrt{2}$, $(|g\rangle - |e\rangle)/\sqrt{2}$, $(|g\rangle + i|e\rangle)/\sqrt{2}$, and $(|g\rangle - i|e\rangle)/\sqrt{2}$, exchanging the state to the emitter qubit and measuring the density matrices of the propagating modes with quantum state tomography. The optimized Pauli transfer matrix is derived from the six density matrices of the cardinal states, with process fidelity turned out to be 94.5%.

In future work, this phase compensation method could be improved by quantitatively modelling the system and operations to calculate the optimal phase, eliminating the need for an initial measurement to determine $\Theta(t)$.

3.3 Dual-rail photon emission in frequency bins

This section focuses on encoding quantum information into two photonic modes to enable error detection in distributed QC systems. In Sec. 3.1, we deterministically encode the quantum information from a superconducting qubit to single-rail emitted photons. However, the photons can easily get lost during propagation in the quantum channel, which is one of the main limitations of the performance of a distributed QC system [22, 25, 33]. Dual-rail photon emission, by introducing an additional degree of freedom to the single-photon output field, enables error-detection heralding protocols to identify photon loss during transmission. In our approach, frequency bins of photonic modes serve as the way to introduce this extra degree of freedom, specifically the transformation $(\alpha |g\rangle + \beta |e\rangle) \otimes |0\rangle_{\omega_1} |0\rangle_{\omega_2} \rightarrow |g\rangle \otimes (\alpha |1\rangle_{\omega_1} |0\rangle_{\omega_2} + \beta |0\rangle_{\omega_1} |1\rangle_{\omega_2})$, encoding the quantum state from a transmon to two propagating modes with different frequencies. In this section, we explain our experiment for generating frequency-bin-encoded photons.

3.3.1 Setup

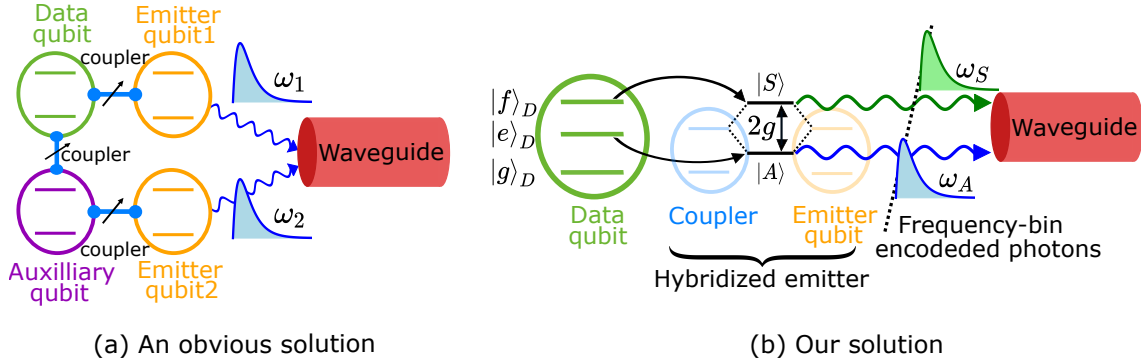


Figure 3.11: (a) An obvious solution for generating frequency-bin encoded photons, which needs two emitter qubits coupled to the waveguide. (b) Our hardware-efficient solution based on the qubit-coupler-qubit architecture.

To implement frequency-bin encoding for photons, where two photonic modes are emitted simultaneously but at different frequencies, we require two emission states and two concurrent transitions. An obvious solution to meet this requirement is to extend the qubit-coupler-qubit system discussed in Section 3.1 by doubling it, resulting in the four-qubit structure depicted in Fig. 3.11(a). Initially, we use the parametric coupler to generate an entangled state between the data and auxiliary qubits, yielding the process from the initial state $(\alpha |g\rangle_D + \beta |e\rangle_D) |g\rangle_A$ to $\alpha |e\rangle_D |g\rangle_A + \beta |g\rangle_D |e\rangle_A$. The data qubit then transfers its state to emitter qubit 1 via the coupler between them, which emits a photon at the qubit frequency ω_1 . Simultaneously, the auxiliary qubit transfers its state to emitter qubit 2, which emits a photon at a different frequency ω_2 [Fig. 3.13(a)]. This results in the simultaneous emission of two photons at distinct frequencies, fulfilling the requirements of frequency-bin encoding.

In our work, instead, we employ the same qubit-coupler-qubit structure as in Section 3.1 for single-photon emission, where only one emitter qubit is coupled to a

waveguide. This approach works by forming a hybridized emitter, created by bringing the coupler and emitter qubit into resonance through proper dc flux biasing. Since these two qubits are coupled, they form hybridized modes consisting of a symmetric state $|S\rangle$ and an antisymmetric state $|A\rangle$, both of which are strongly coupled to the waveguide for propagating mode emission. Additionally, both of these states are coupled to the data qubit, enabling the transfer of quantum information. The energy gap between the two hybridized modes is twice the static coupling rate between the emitter qubit and the coupler, g (Fig. 3.12).

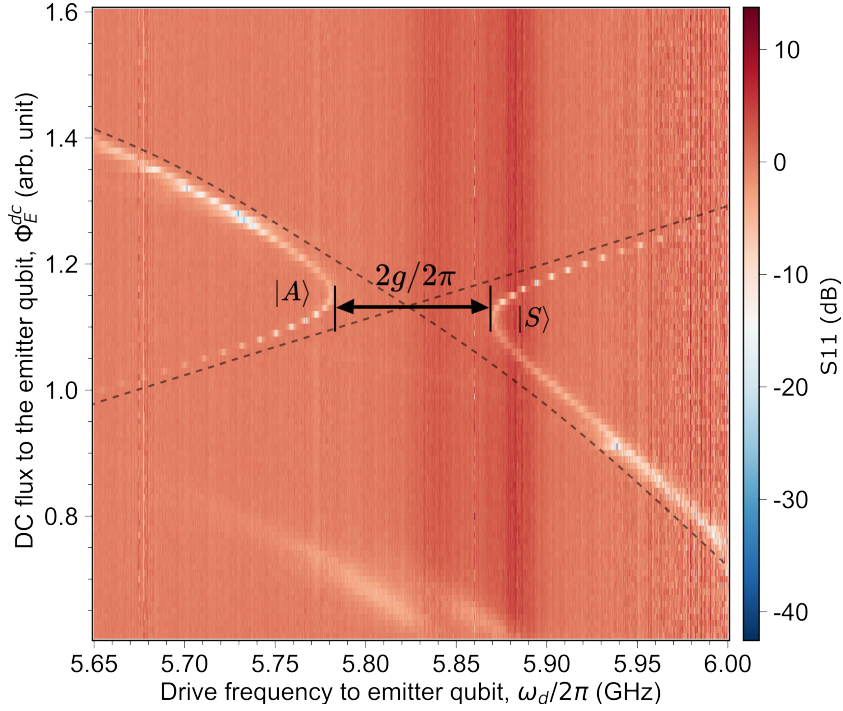


Figure 3.12: Measurement of the hybridized modes from the S21 emitter qubit spectroscopy (see Appendix 5.1.1 and 5.2.1 for details). By applying a dc flux of $\Phi_C^{dc} = 0.355\Phi_0$ to the coupler and sweeping the dc flux to the emitter qubit around $\Phi_E^{dc} = 0.177\Phi_0$, we observe the avoided crossing between the two modes.

By leveraging the multi-level structure of the data qubits, two simultaneous transitions can occur between the data qubit and the hybridized emitter: one that preserves excitation and another that does not. In our implementation, the excitation-preserving transition occurs from the $|e\rangle_D$ state of the data qubit to the antisymmetric state $|A\rangle$, while the non-excitation-preserving transition is from the $|f\rangle_D$ state of the data qubit to the symmetric state $|S\rangle$. However, it is worth noting that, depending on the specific energy levels and coupling configurations, these transitions could be reversed, with $|f\rangle_D$ transitioning to $|A\rangle$ and $|e\rangle_D$ transitioning to $|S\rangle$.

This approach enables the simultaneous emission of two photonic modes at different frequencies while reducing the number of required qubits, compared to the obvious method. As depicted in Fig. 3.13, the process starts by preparing the data qubit in a superposition of the ground and first excited states, followed by two pulses, π_{ef} and π_{ge} , to bring the qubit into a superposition of its first and second

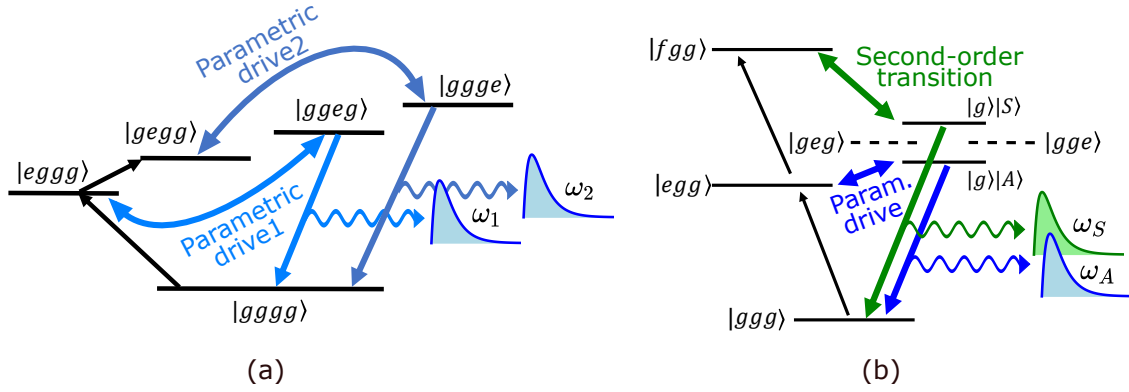


Figure 3.13: Energy diagrams of the system for two configurations: (a) the obvious solution, employing two excitation-preserving drives to control photon emission to two separate couplers and emission qubits, and (b) our approach, utilizing one excitation-preserving drive and one non-preserving drive, with only one coupler and one emission qubit.

excited states. In our work, the excitation-preserving drive is a parametric drive applied via the coupler (Section 3.1.1), exchanging population from $|e\rangle_D$ to $|A\rangle$. This allows the population to decay into the waveguide, emitting a photon at frequency ω_A . Conversely, the non-excitation-preserving drive is a second-order transition (Sec. 3.1.2), applied through the charge line of the data qubit, enabling the transfer of population from $|f\rangle_D$ to $|S\rangle$. This transition also results in a decay into the waveguide, emitting a photon at a different frequency ω_S . Together, this process allows for the emission of two photonic modes with distinct frequencies at the same time.

We use the notations $(\hat{d}, \hat{d}^\dagger)$, $(\hat{c}, \hat{c}^\dagger)$, and $(\hat{e}, \hat{e}^\dagger)$ to represent the annihilation and creation operators of the data qubit, coupler, and emitter qubit, respectively. The hybridized emitter, formed through the interaction of the coupler and the emitter qubit, can be described using the symmetric mode $\hat{a}_S = (\hat{e} + \hat{c})/\sqrt{2}$ and the antisymmetric mode $\hat{a}_A = (\hat{e} - \hat{c})/\sqrt{2}$. In the rotating frame defined by $\omega_D \hat{d}^\dagger \hat{d} + \omega_S \hat{a}_S^\dagger \hat{a}_S + \omega_A \hat{a}_A^\dagger \hat{a}_A$, and restricting to the two lowest energy levels of the coupler and emitter qubit due to their anharmonicity, the effective Hamiltonian of the system is given by,

$$\hat{H}_{\text{eff}} = (\eta \hat{d}^\dagger \hat{a}_A + \eta^* \hat{d} \hat{a}_A^\dagger) + (\zeta \hat{d}^{\dagger 2} \hat{a}_S + \zeta^* \hat{d}^2 \hat{a}_S^\dagger) + \frac{\alpha}{2} \hat{d}^{\dagger 2} \hat{d}^2, \quad (3.18)$$

where η and ζ denote the amplitudes of the parametric gate ($\hat{d}^\dagger \hat{a}_A$) and the second-order transition ($\hat{d}^{\dagger 2} \hat{a}_S$), respectively. Note that η corresponds to the same physical parameter represented by J in Sec. 3.1, both indicating the strength of the parametric drive. We retain both notations for consistency with their respective papers.

3.3.2 Experiments

In this section, we present the experimental results for the generation and characterization of frequency-bin-encoded photons. In the experimental realization, we first prepare the states and then simultaneously apply the two transitions via the

parametric drive and the second-order-transition drive. The parametric and the second-order drives cause dispersive and ac-Stark shifts on qubit frequencies, respectively, as shown in Sec. 3.1. The frequency shift from the parametric drive is minimal and barely noticeable, whereas the Stark shift is significantly larger and needs to be accounted for when setting the drive frequency for the second-order transition (Fig. 3.7). The generated photonic modes are matched through two temporal mode filters with their corresponding frequencies (Sec. 2.4).

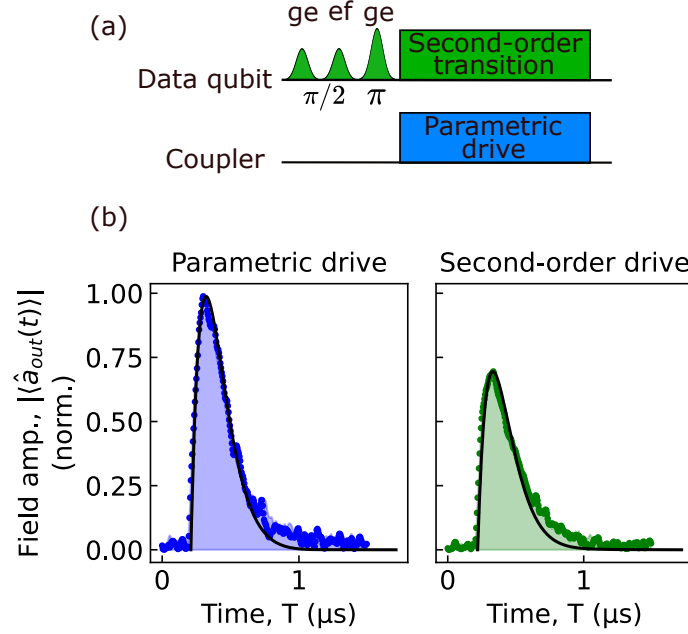


Figure 3.14: (a) Pulse sequence for generating a frequency-bin-encoded photon with a non-zero amplitude. (b) Amplitude of the frequency-bin-encoded photonic modes. Filled circles indicate the measured data with both drives applied simultaneously, while the shaded area corresponds to the measured data with the drives applied individually. The solid black curves represent the theoretical predictions. The relative amplitude difference between the two photonic modes is calculated according to the assumption in Eq. 3.19.

We then proceed to present the photon amplitude by examining the first-order output field of each propagating mode. As explained in Sec. 3.1.1, during parametric drive photon emission, the amplitude (first-order moment) of a full photon is zero, while the mean photon number (second-order moment) remains positive. This occurs because the reduced density matrix of each mode lacks coherence (see Fig.S3 in the supplementary material of Paper 3 for the reduced density matrices), resulting in zero first-order moments. To illustrate the amplitude of the emitted photon field as a function of time, we thus introduce some proportion of ground state into the state of the data qubit. By applying a sequence of $\pi/2$ -ge, $\pi/2$ -ef, and π -ge pulses, and then simultaneously the parametric drive and the second-order-transition drive [see Fig. 3.14(a) for the pulse sequence], we generate a frequency-bin-encoded photon described by the state $\frac{1}{2}|0\rangle_{\omega_A}|0\rangle_{\omega_S} + \frac{1}{\sqrt{2}}|1\rangle_{\omega_A}|0\rangle_{\omega_S} + \frac{1}{2}|0\rangle_{\omega_A}|1\rangle_{\omega_S}$. In this expression, i (j) in the state $|i\rangle_{\omega_A}|j\rangle_{\omega_S}$ represents the number of photons in the antisymmetric (symmetric) mode. The emitted photon amplitude for both modes is shown in

Fig. 3.14(b), and the field amplitude difference is attributed to the coefficients before $|1\rangle_{\omega_A} |0\rangle_{\omega_S}$ and $|0\rangle_{\omega_A} |1\rangle_{\omega_S}$ in the target state. By tuning the drive strengths of the parametric drive (η) and the second-order transition (ζ) to fulfil $\eta = \sqrt{2}\zeta$, we achieve the same speed for the emission of both photonic modes, as the two drives correspond to one-photon and two-photon transitions, respectively. The observed waveform exhibits the same shape as the single-rail emission in Fig. 3.4 and Fig. 3.10(a), with a high rise at the beginning, and then followed by an exponential decay.

3.3.3 Tomography results

After displaying the field amplitude, we remove the vacuum component in the subsequent measurements to transfer the arbitrary state $\alpha|g\rangle_D + \beta|e\rangle_D$. Temporal mode filters are then digitally applied to the measured signal to match the generated propagating modes, which are subsequently analyzed via quantum state tomography. The pulse sequence for the state without the vacuum component is shown in Fig. 3.15(a), incorporating the interleaved measurements for mode denoising as detailed in Fig. 2.4.

Furthermore, we analyze the moments of the photon field for different initial qubit states [Fig. 3.15(b)]. The second-order moments correspond to the mean photon number in the two modes. When the qubit is fully prepared in the excited state $|e\rangle_D$, it ideally emits a full photon at the antisymmetric-state frequency, resulting in an average photon number $\langle \hat{a}_A^\dagger \hat{a}_A \rangle \sim 1$, with \sim indicating the experimental imperfections. While for the prepared state $|f\rangle_D$, ideally, a full photon is emitted at the symmetric-state frequency, resulting in $\langle \hat{a}_S^\dagger \hat{a}_S \rangle \sim 1$ in Fig. 3.15(b). If we prepare the state in the equal superposition of both excitations, $\frac{1}{\sqrt{2}}(|e\rangle_D + |f\rangle_D)$, we end up with a maximum entanglement between the two photonic modes [$\langle \hat{a}_A^\dagger \hat{a}_S \rangle$ in Fig. 3.15(b)]. As expected, the fourth-order moments remain zero, indicating the emission of a single photon.

The moments are normalized in the same way as in Eq. (3.10), where we assume that the decay of the data qubit occurs via two channels, the detected modes of the waveguide with Γ_{eff} and the intrinsic losses of the data qubit with Γ_D , respectively. Accordingly, when the data qubit is prepared in the state $|e\rangle_D$ or $|f\rangle_D$ for photon emission at frequencies ω_A and ω_S , respectively, we assume the second-order moments to be

$$\langle \hat{a}_A^\dagger \hat{a}_A \rangle = \frac{\Gamma_{\text{eff}}^A}{\Gamma_{\text{eff}}^A + \Gamma_D^{ge}} \quad \text{and} \quad \langle \hat{a}_S^\dagger \hat{a}_S \rangle = \frac{\Gamma_{\text{eff}}^S}{\Gamma_{\text{eff}}^S + \Gamma_D^{ef}}, \quad (3.19)$$

where Γ_{eff}^A and Γ_{eff}^S are the effective decay rates of the propagating modes obtained by exponentially fitting the emitted photon envelopes in Fig. 3.14(b). $\Gamma_D^{ge} = 1/T_1^{ge'} = 48$ kHz and $\Gamma_D^{ef} = 1/T_1^{ef'} = 37$ kHz are the longitudinal relaxation rates of the data qubit. The other moments are normalized accordingly.

Additionally, we perform joint quantum state tomography on four cardinal states using two optimization methods, least squares (LS) (Sec. 2.5.1) and gradient descent (GD) (Sec. 2.5.1). The states investigated are $|1\rangle_{\omega_A} |0\rangle_{\omega_S}$, $\frac{1}{\sqrt{2}}(|1\rangle_{\omega_A} |0\rangle_{\omega_S} + |0\rangle_{\omega_A} |1\rangle_{\omega_S})$, $|0\rangle_{\omega_A} |1\rangle_{\omega_S}$, and $\frac{1}{\sqrt{2}}(|1\rangle_{\omega_A} |0\rangle_{\omega_S} - i|0\rangle_{\omega_A} |1\rangle_{\omega_S})$. Subsequently, we perform quantum

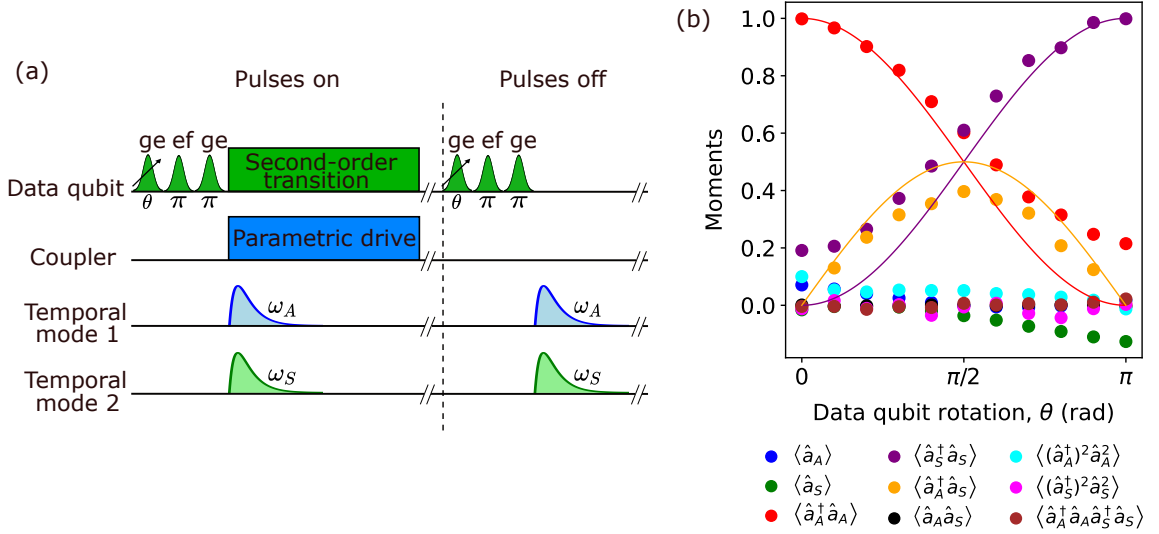


Figure 3.15: (a) Pulse sequence for tomography measurements. The measurement is done in an interleaved manner by sweeping between two cases, with and without the transition pulses, for moment denoising. (b) Moments of the emitted frequency-bin encoded photon, with coloured dots representing the measured data and the solid curves representing the ideal case. The red solid line, denoting the ideal value of $\langle \hat{a}_A^\dagger \hat{a}_A \rangle$, is given by $\cos(\theta/2)^2$; the purple solid line, denoting the ideal value of $\langle \hat{a}_S^\dagger \hat{a}_S \rangle$, is given by $\sin(\theta/2)^2$; and the orange solid line, representing the ideal value of $\langle \hat{a}_A^\dagger \hat{a}_S \rangle$, is $\sin(\theta)/2$.

process tomography using the LS optimization, utilizing the reconstructed density matrices of these four cardinal states as input to determine the process matrix χ [116]. For both optimization methods, the average fidelity of the four states reconstructed from QST and the fidelity of the process matrix obtained from quantum process tomography are presented in Table 3.1. In the LS optimization method, the infidelity of the reconstructed density matrix arises from both coherent and incoherent errors. In contrast, the GD optimization with a rank-1 ansatz ($r = 1$) constrains the reconstructed density matrix to be a pure state (see Sec. 2.5.1 for details). This constraint effectively mitigates noise and other incoherent errors, resulting in a higher state fidelity relative to the ideal pure state. By comparing the fidelities obtained from both optimization methods, we find that our system is primarily limited by incoherent errors, including qubit decoherence and thermal excitations.

Table 3.1: Average fidelity of the four reconstructed states from QST and process fidelity from QPT, using LS and GD optimization methods.

Optimization method	Averaged QST fidelity	QPT fidelity
LS	86.2%	90.4%
GD	97.7%	98.5%

Compared to the single-rail photon emission discussed in Sec. 3.1.1, the fidelity of the dual-rail emission is lower. One factor contributing to this reduced fidelity

is the coherent errors in the control pulses used to drive transitions between the data qubit and the hybridized emitter. Since dual-rail emission involves two pulses simultaneously, it introduces more errors. Although these coherent errors are not dominant, they contribute around 2% of the total infidelity. Another significant factor is the behaviour of the parametric coupler: in single-rail emission, the coupler remains mostly unexcited, whereas in dual-rail emission, it forms a hybridized system with the emitter qubit. Specifically, the relaxation of the coupler and the decay rate of the data qubit during photon emission contributes approximately 5% infidelity to the overall system performance of the dual-rail emission, with the coupler contributing more significantly due to its shorter coherence times ($T_1 = 2.3 \pm 0.5 \mu\text{s}$ and $T_2 = 1.4 \pm 0.4 \mu\text{s}$). Thermal excitation of the data qubit also contributes to the infidelity, accounting for a portion of the remaining errors.

3.4 Generation of entangled photons from continuously-driven TLS

In this section, we present our experimentally demonstrated approach for generating time-frequency entangled photonic states from the steady-state emission of a quantum emitter coupled to a waveguide. By using a coherent drive and selecting photonic modes with digitally applied temporal mode filters, our method provides a simple and effective way to generate entanglement between two temporally overlapping but spectrally orthogonal modes from the emitter's continuum emission.

3.4.1 Experimental setup

In this experiment, we use the same superconducting device as in Sec. 3.1 and 3.2. However, only the emitter qubit (acting as a two-level system, TLS) and the waveguide coupled to it are utilized. The emitter qubit is also coupled to a coupler (not used), which is positioned at its sweet spot and remains far detuned from the emitter qubit, ensuring that it does not affect the system's performance. We have the transmon-type superconducting qubit strongly coupled to a coplanar waveguide, enabling it to interact with the propagating microwave modes (Fig. 3.16). The waveguide is connected with a reflection setup, where the coherent and continuous drive is sent to the qubit through the waveguide, while from the output we can measure the propagating modes, and characterize the entanglement between the two modes. The qubit is coupled to the waveguide with a decay rate of $\Gamma_E = 8 \text{ MHz}$, making the T_1 of the qubit to be around 20 ns.

The pulse sequence employed in our experiment is illustrated in Fig. 3.17. We continuously drive the qubit at its resonant frequency, $\omega_d = \omega_E^{ge}$, with Ω representing the Rabi frequency of the coherent drive, which is proportional to the driving amplitude. After initiating the qubit drive for 200 ns, a duration significantly longer than the qubit's T_1 , we ensure that the qubit reaches the steady state. At this point, we apply two temporal mode filters, $f_1(t)$ and $f_2(t)$, on the reflected time trace, in post-processing.

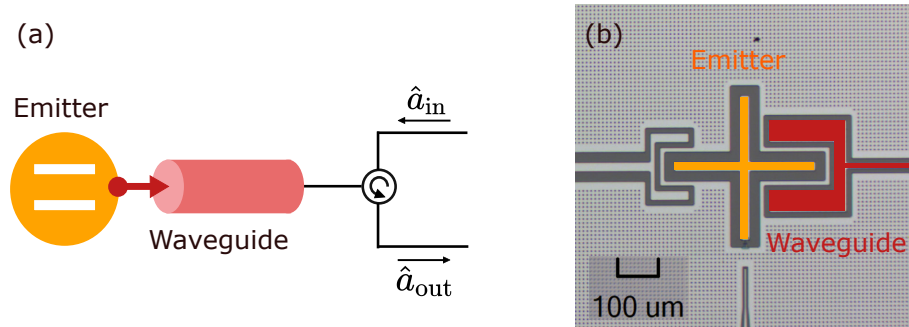


Figure 3.16: The superconducting device used for the entanglement generation from the qubit driven into the steady state. (a) Schematic representation of the device and the reflection measurement setup. (b) False-color optical micrograph of the device. A transmon qubit (orange) is capacitively coupled to a waveguide (red).

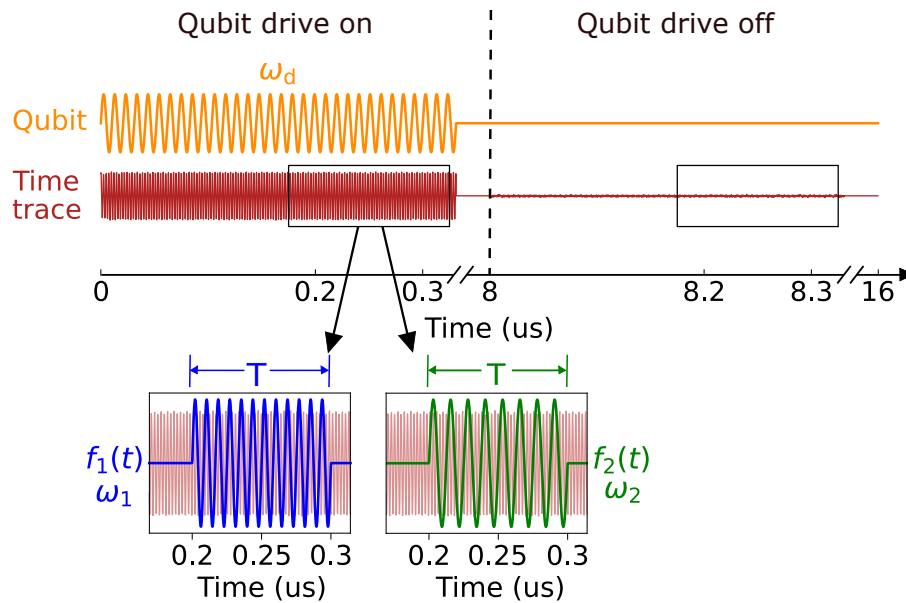


Figure 3.17: Pulse sequence for entanglement generation. An on-resonance drive is applied to the waveguide qubit to bring it into the steady state. Two temporal filters, $f_1(t)$ and $f_2(t)$, are then applied simultaneously to match with the reflected time trace in post-processing, as shown in the insets. As described in Fig. 2.4, the measurement is done in an interleaved manner by sweeping between two cases, with and without the drive to the qubit. The same temporal filters are used to match both cases. For simplicity, the insets corresponding to the case without the qubit drive have been omitted.

We determine the conversion between the qubit drive amplitude and the Rabi frequency Ω through a power calibration of the qubit (Fig. 5.5 in Appendix 5.2.1). This calibration is essential because it acts as a normalization between the experimental data and the model. By varying the drive amplitude and measuring the qubit's single-tone spectroscopy through the waveguide reflection setup, we identify the critical driving power. At this power level, the input pulse strength satisfies the condition $\Omega = \Gamma_E/\sqrt{2}$ [125]. The driving amplitude corresponding to the largest dip in the magnitude quadrature of the qubit spectroscopy, denoted as A_{critic} , represents this condition. Given the proportional relationship between the drive rate Ω and the driving amplitude A_{in} , the drive strength can be expressed in terms of the input power P_{in} of the driving pulse as follows,

$$\Omega = \frac{A_{\text{in}}}{A_{\text{critic}}} \frac{\Gamma_E}{\sqrt{2}}. \quad (3.20)$$

3.4.2 Theoretical model

In this experiment, the emitter qubit coupled to the waveguide can be described by a two-level system (TLS), with transition frequency between $|g\rangle$ and $|e\rangle$ being ω_E^{ge} . In the frame that rotates with the frequency of the TLS, the Hamiltonian of the TLS driven by Rabi frequency Ω is given by

$$\hat{H}_Q = -i\Omega(\hat{\sigma}_+ - \hat{\sigma}_-)/2. \quad (3.21)$$

Compared to Eq. (1.29), we omit the detuning term, and add a phase shift in the imaginary driving term to facilitate fitting to the measured data. Knowing the decay rate Γ_E from the emitter qubit into the waveguide, the dissipative dynamics of the qubit is described by the master equation [126–128],

$$d\hat{\rho}/dt = -i[\hat{H}_Q, \hat{\rho}] + \frac{\Gamma_E}{2}\mathcal{D}[\hat{\sigma}_-]\hat{\rho}, \quad (3.22)$$

where the Lindblad superoperator is defined as $\mathcal{D}[\hat{A}] \equiv 2\hat{A}\hat{\rho}\hat{A}^\dagger - \{\hat{A}^\dagger\hat{A}, \hat{\rho}\}$.

A diagonalization of \hat{H}_Q yields two eigenstates $|\pm\rangle \equiv (|g\rangle \pm |e\rangle)/\sqrt{2}$ with corresponding eigenenergies $\pm\Omega$, which in the dressed-atom picture can be understood as hybrid light-matter states between the qubit and the drive. In the strong driving regime ($\Omega > \Gamma_E/4$), these eigenenergies can be resolved, and the emission spectrum of resonance fluorescence acquires the Mollow-triplet structure [70, 71, 129], with two side peaks emerging around a central peak at the drive frequency (see Fig. 3.18). This structure can be understood as transitions between the dressed eigenstates, the central peak at ω_E^{ge} corresponding to the doubly-degenerate transition $|\pm\rangle \rightarrow |\pm\rangle$, and the two side peaks at frequencies $\omega_E^{ge} \pm \Omega$ corresponding to transitions $|+\rangle \rightarrow |-\rangle$ and $|-\rangle \rightarrow |+\rangle$, respectively.

In the experiment, there are two temporal filters applied simultaneously to match the photonic modes. Reference [130] introduces a method based on the input-output theory, where the system can be treated as a cascaded quantum system [97], and the temporal filter can be modelled as a virtual cavity coupled non-reciprocally

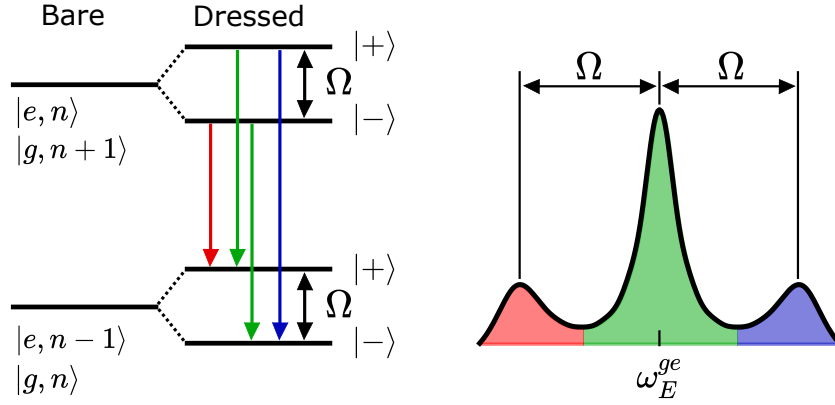


Figure 3.18: Origin of the peaks in the Mollow triplet. The three peaks result from four transitions between the dressed states of a two-level atom interacting with a strong resonant driving field.

to the system with a time-dependent coupling. Here, we extend this approach to capture simultaneously two temporal modes by introducing two virtual cavities (with annihilation operator \hat{a}_k , for $k = 1, 2$), resulting in the following cascaded master equation in the rotating frame of the drive,

$$\begin{aligned} \frac{d\hat{\rho}}{dt} = & -i[\hat{H}, \hat{\rho}] + \frac{\Gamma}{2}\mathcal{D}[\hat{\sigma}_-]\hat{\rho} + \sum_{k=1}^2 \frac{|g(t)|^2}{2}\mathcal{D}[\hat{a}_k]\hat{\rho} \\ & - \sum_{k=1}^2 \sqrt{\Gamma} \left(g_k^*(t)[\hat{a}_k^\dagger, \hat{\sigma}_-\hat{\rho}] + g_k(t)[\hat{\rho}\hat{\sigma}_+, \hat{a}_k] \right), \end{aligned} \quad (3.23)$$

where $g_k(t)$ is the time-dependent coupling encoded by the temporal filters,

$$g_k(t) = -\frac{f_k(t)}{\sqrt{\int_0^t dt' |f_k(t')|^2}}. \quad (3.24)$$

In our implementation, the profile $v(t)$ of the temporal filters [Eq. (2.10)] is defined as a normalized boxcar function $v(t) = \frac{1}{\sqrt{T}}[\Theta(t - t_0) - \Theta(t - t_0 - T)]$, with $\Theta(t)$ the Heaviside step function and t_0 the start time of the temporal filters. This results in the time-dependent couplings $g(t) = -1/\sqrt{t - t_0}$.

The condition for the two temporal filters to be orthogonal is

$$\int f_1^*(t)f_2(t)dt = 0. \quad (3.25)$$

For our case with two filters of the form Eq. (2.10), the orthogonality condition reduces to $(\omega_2 - \omega_1)/2\pi = m/T$, where m is an arbitrary integer. In this work, we use $T = 100$ ns, so the condition for orthogonality between the two modes is $(\omega_2 - \omega_1)/2\pi = m \cdot 10$ MHz. Additionally, modes that are separated by a large frequency detuning can also be considered orthogonal to a good extent.

3.4.3 Single-mode measurement results

To calibrate the measurement settings, we start from the results from one-dimensional measurements that characterize the system by matching only a single mode. The

frequency of the temporal filter, ω_1 , is swept around the down-converted intermediate frequency (IF) of the qubit. We conduct two sets of measurements. In the first case [Fig. 3.19(a)], the template matching duration is held constant while the drive amplitude to the qubit is varied. During this process, we observe the second-order moment $\langle \hat{a}_1^\dagger \hat{a}_1 \rangle$, corresponding to the mean photon number. This measurement is analogous to the Mollow triplet experiment, where increasing power results in the emergence of side peaks (Fig. 3.18). The separation between the central peak and the side peaks corresponds to the Rabi frequency, Ω .

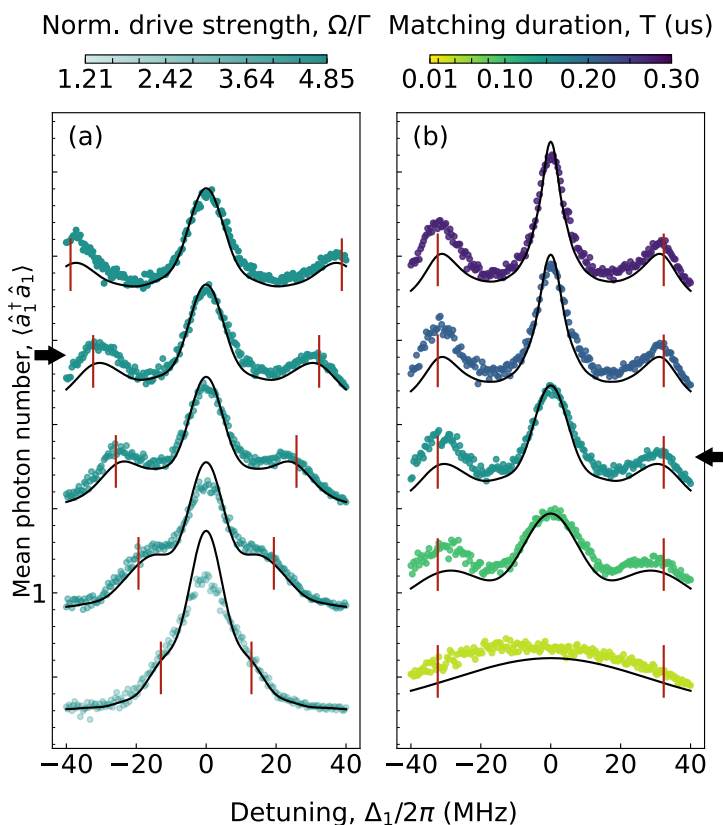


Figure 3.19: Moment $\langle \hat{a}_1^\dagger \hat{a}_1 \rangle$ from the single-mode measurement where (a) the template-matching duration is fixed at $T = 100$ ns while the drive Rabi frequency Ω is swept, and (b) $\Omega = 4.04\Gamma$ while T is swept. Each curve is vertically offset by 0.3 relative to the one below it. The black solid curve is the theoretical prediction. The red vertical lines mark the positions of $\pm\Omega$, which match the location of the side peaks of the corresponding curves.

In the second case, the Rabi frequency of the qubit drive is fixed [Fig. 3.19(b)], and the template matching duration is varied. When the duration is too short, the side peaks become indistinguishable due to the broadening of the frequency domain as a result of the reduced time window. The second curve from the top in Fig. 3.19(a) and the third curve from the top in Fig. 3.19(b) (marked with black arrows in the figure) are measured under the same condition, with Rabi frequency set to $\Omega = 4.04\Gamma$ and the duration of the temporal modes set to $T = 100$ ns.

The relation between the input and output modes follows input-output theory

(Eq. 1.31),

$$\sqrt{\Gamma_E} \hat{\sigma}_1^- = \hat{a}_1^{\text{out}} - \hat{a}_1^{\text{in}}. \quad (3.26)$$

The qubit's emission operator, $\sqrt{\Gamma_E} \hat{\sigma}_1^-$, is the difference between the output and input fields. In Fig. 3.19 and the subsequent measurements, we present results for the qubit's emission after subtracting the coherent input field. Reference [131] implements this subtraction experimentally via a cancellation pulse. Here, we perform the subtraction by post-processing the measured output mode.

We evaluate the reflected input mode captured by the temporal filter using the following expression,

$$\langle \hat{a}^{\text{in}} \rangle = \frac{\Omega}{\sqrt{\Gamma}} \cdot \int_0^T e^{i(\omega_1 t + \phi)} \cos(\omega_{\text{IF}} t) dt. \quad (3.27)$$

To isolate the qubit's emission, we fit the model to the measured output field, subtracting this expression. This process effectively removes the coherent background from the output field. This allows us to align the measured and simulated moments, ensuring consistent normalization and phase across both. The emission operator $\sqrt{\Gamma} \hat{\sigma}_1^-$ is isolated, but for simplicity, we denote it as $\hat{a}_1 = \sqrt{\Gamma} \hat{\sigma}_1^-$ in the results. In the following 2D measurement, we subtract the coherent background for both modes \hat{a}_1 and \hat{a}_2 in the same way.

3.4.4 Two-mode measurement results

To verify entanglement between the two selected propagating modes, we match the measured time trace using two simultaneously applied temporal filters, $f_1(t)$ and $f_2(t)$, and the frequencies of the filters are swept. We fix the Rabi frequency of the qubit drive at $\Omega = 4.04\Gamma$ and the duration of the temporal modes at $T = 100$ ns, which is a working point where the side peaks are well-resolved according to Fig. 3.19, and start the 2D mode matching. At this working point, each moment is calculated in each pixel of a 2D map, where the x- and y-axes correspond to the frequencies of the swept temporal filters, ω_1 and ω_2 . Figure 3.20(a, b) show the first-order moments, with results for both the simulation and the measured data, and Figure 3.20(c-h) show the second-order moments (calculated according to Sec. 2.4). For all moments, the data are normalized relative to the simulated value of the central peak of the second-order moments of the two modes, $\langle \hat{a}_1^\dagger \hat{a}_1 \rangle$ and $\langle \hat{a}_2^\dagger \hat{a}_2 \rangle$, which physically represent the mean photon number.

In the frequency regions around $(\Delta_1, \Delta_2) = (-\Omega, +\Omega)$ or $(+\Omega, -\Omega)$, near the anti-diagonal corners of the 2D maps, the moments $\langle \hat{a}_1 \rangle$ and $\langle \hat{a}_2 \rangle$ are close to zero [Fig. 3.20(a, b)], while the cross-second-order moment $\langle \hat{a}_1 \hat{a}_2 \rangle$ exhibits a peak [yellow circles in Fig. 3.20(g)]. This indicates the presence of two-mode-squeezing type entanglement. Conversely, in the region around $(\Delta_1, \Delta_2) = (+\Omega, +\Omega)$ or $(-\Omega, -\Omega)$, along the diagonal of the 2D moment maps, the cross-second-order moment $\langle \hat{a}_1^\dagger \hat{a}_2 \rangle$ shows a peak [green circles in Fig. 3.20(h)], which suggests a beam-splitter type of entanglement. In this case, the two modes overlap in both time and frequency, indicating they are identical states and generally non-orthogonal.

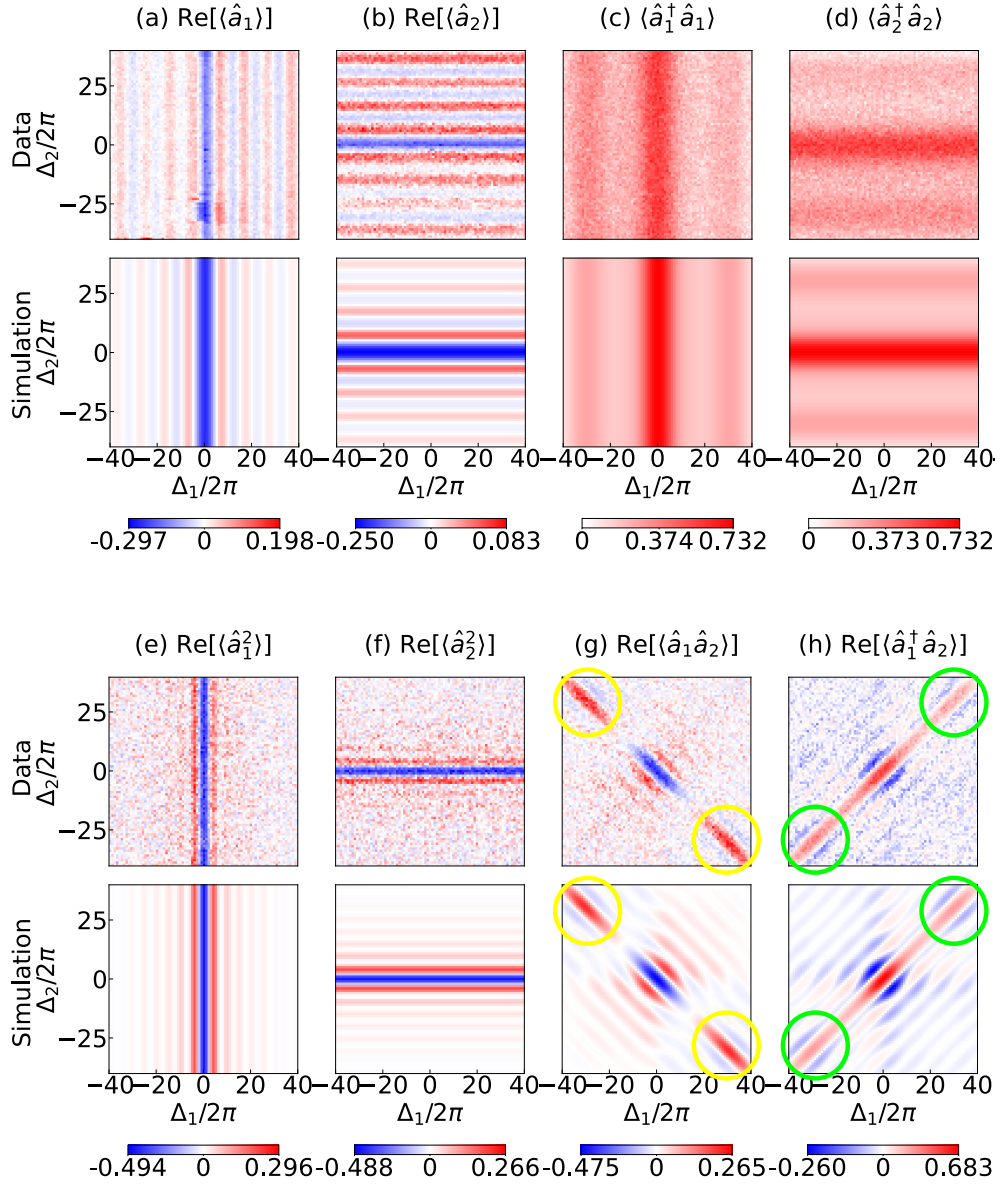


Figure 3.20: First- and second-order moments of the temporally matched modes. The first row of each subplot shows the measured moment, while the second row of each subplot shows the simulation.

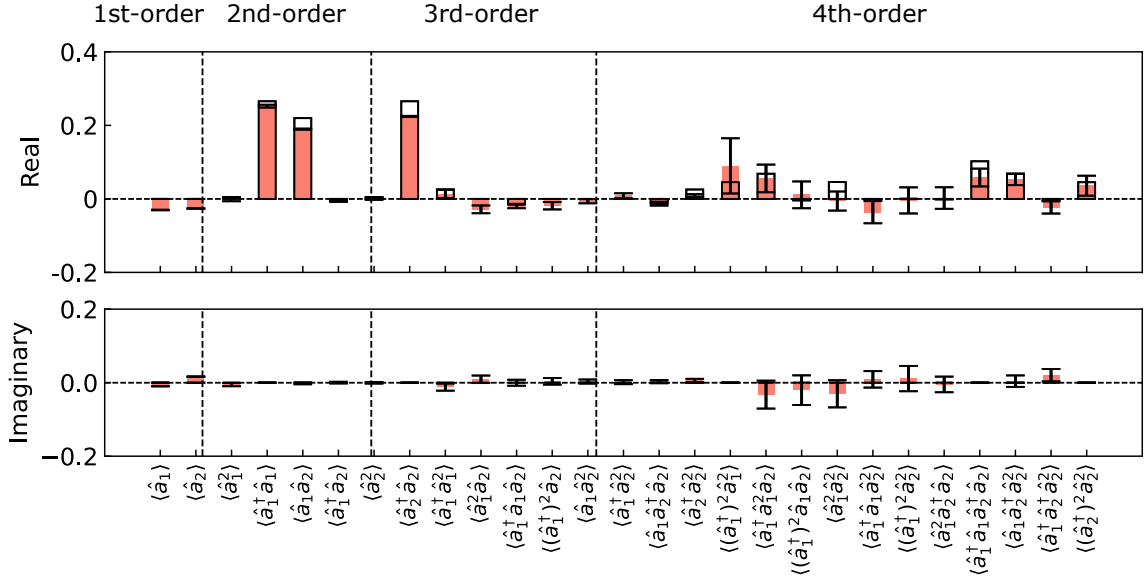


Figure 3.21: First- to fourth-order moments of the temporally matched modes at the selected point $(\Delta_1, \Delta_2) = (-\Omega, +\Omega)$. The red bar is from the measurement, and the black wireframe is from the simulation.

We focus on the frequency point $(-\Omega, +\Omega)$, where the two modes belong to opposite side peaks of the Mollow triplet and satisfy the frequency orthogonality condition in Eq. 3.25. At this frequency point, we compute and show moments $\langle (\hat{a}_1^\dagger)^{m_1} \hat{a}_1^{n_1} (\hat{a}_2^\dagger)^{m_2} \hat{a}_2^{n_2} \rangle$ for $m_1, n_1, m_2, n_2 \in \{0, 1, 2\}$ and $m_1 + n_1 + m_2 + n_2 \leq 4$, resulting in 27 moments excluding conjugation redundancy (Fig. 3.21), which will be further used for quantum state tomography in the next section.

3.4.5 Tomography result and logarithmic negativity

In this work, we employ two methods to perform joint quantum state tomography on the two measured photonic modes, described in the following. For each frequency point within the regions $\Delta_1 \in [-40, -10]$ MHz and $\Delta_2 \in [10, 40]$ MHz, we compute the 27 moments up to fourth order (as listed in Fig. 3.21). We then reconstruct the density matrices at each point using least-squares (LS) optimization and compressed-sensing (CS) optimization, with the 27 measured moments as input (see Sec. 2.5.1 for details). The density matrices obtained from LS optimization and CS optimization at the frequency point $(-\Omega, +\Omega)$ are shown in Fig. 3.22(a) and Fig. 3.22(b), respectively. We quantify the degree of entanglement between the two temporal modes using the logarithmic negativity $E_{\mathcal{N}}$, a commonly used entanglement measure for bipartite systems [132]. Given a general bipartite state composed of subsystems A and B , the logarithmic negativity is defined as,

$$E_{\mathcal{N}} \equiv \log_2 \left(\left\| \rho^{\text{T}A} \right\|_1 \right), \quad (3.28)$$

where $\rho^{\text{T}A}$ denotes the partial transpose of the density matrix ρ with respect to subsystem A , and $\|\cdot\|_1$ is the trace norm. For each frequency point, we calculate the

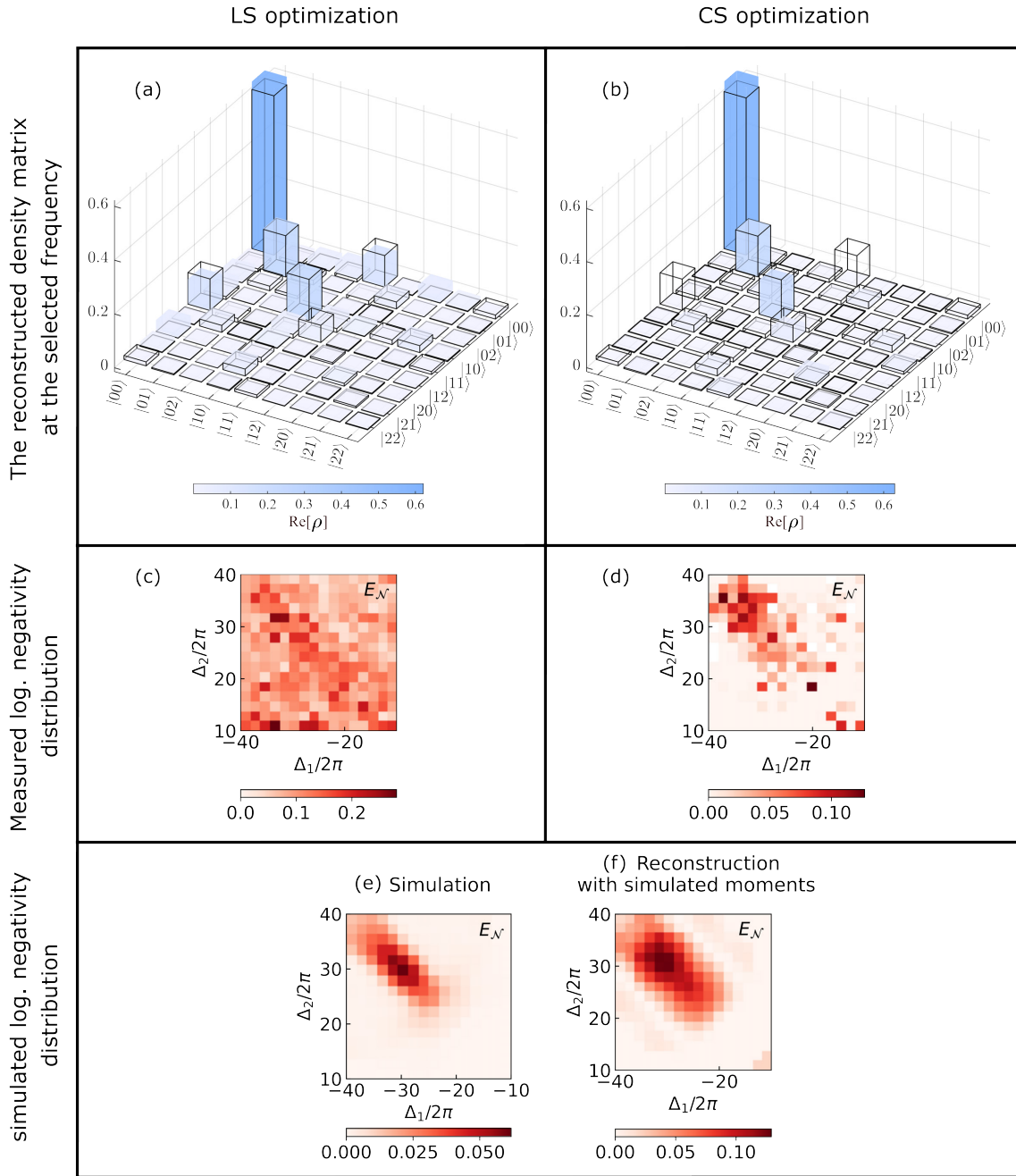


Figure 3.22: Tomography result of the entangled photonic modes and the entanglement witness. (a-b) Reconstructed density matrices at the point of maximum logarithmic negativity E_N , obtained using LS and CS optimization-based quantum state tomography, respectively. (c-d) Measured distributions of logarithmic negativity E_N , calculated from the density matrices reconstructed via LS and CS optimizations. (e) Simulated logarithmic negativity distribution E_N . (f) Logarithmic negativity distribution E_N derived from the density matrices reconstructed using the 27 simulated moments.

corresponding logarithmic negativity from the reconstructed density matrix, from quantum state tomography.

While LS optimization effectively reconstructs the density matrix of the two propagating modes [Fig. 3.22(a)], the resulting $E_{\mathcal{N}}$ distribution over the frequency ranges $\Delta_1 \in [-40, -10]$ MHz and $\Delta_2 \in [10, 40]$ MHz is very noisy [Fig. 3.22(c)]. This noise is attributed to the limited number of moments used for reconstruction and the sparsity of the dataset. To overcome these challenges, we employ CS optimization, which is better suited for sparse datasets and limited moment data. Using CS optimization, we perform the reconstruction [Fig. 3.22(b)] and compute the $E_{\mathcal{N}}$ distribution [Fig. 3.22(d)]. The $E_{\mathcal{N}}$ distribution obtained through CS optimization shows good agreement with the $E_{\mathcal{N}}$ distribution derived from the reconstruction using the selected simulated moments [Fig. 3.22(f)]. CS optimization effectively minimizes the noisy coherent components in the reconstructed moments, resulting in a cleaner $E_{\mathcal{N}}$ distribution. However, it also tends to overly suppress the peaks of $\langle 00|\rho|11\rangle$, potentially underrepresenting certain entanglement features.

As explained in the previous paragraph, we compare the measured $E_{\mathcal{N}}$ distribution to the distribution reconstructed using 27 simulated moments, rather than to the directly simulated distribution. This is due to observed discrepancies between the reconstructed $E_{\mathcal{N}}$ derived from the simulated moments [Fig. 3.22(f)] and the directly simulated $E_{\mathcal{N}}$ [Fig. 3.22(e)]. This discrepancy arises because the reconstruction process includes only the 27 simulated moments, corresponding to the ones measured in the experiment. However, when all moments in the Fock space up to a cutoff of $N = 5$ are included, the reconstructed distribution from the simulated moments aligns closely with the simulation, showing the correctness of our optimization methods. Based on these considerations, we conclude that the maximum $E_{\mathcal{N}}$ observed in our experiment is close to the simulation value of 0.062.

From the positive logarithmic negativity—a recognized measure of entanglement—that aligns with theoretical predictions, we demonstrate that this method successfully generates entangled photonic states through the application of digital temporal filters to the continuum field. This approach is hardware-efficient, requiring only a single emitter, and operates without strict timing constraints due to the steady-state nature of the driven qubit. Furthermore, the entanglement generation rate is limited solely by the emitter’s linewidth, enabling high-speed entanglement production.

Chapter 4

Conclusions

4.1 Summary

In Paper 1, we demonstrated the deterministic transfer of a qubit state into a propagating microwave photon using a qubit–coupler–qubit device, achieving a process fidelity of 94.5%. By employing a time-dependent parametric drive, we shape the temporal profile of the emitted photon to ensure time symmetry and a constant phase, which allows the receiving processor to implement the reabsorption process as a time-reversed version of the emission. In Paper 3, instead of encoding information in the Fock basis of a single propagating mode, we deterministically generate frequency-bin encoded microwave photons in two modes with a process fidelity of 90.4%. The use of frequency bins as an additional degree of freedom serves as a heralding protocol for detecting photon loss.

In Paper 2, we generate entanglement between photonic modes generated by temporally selected signals reflected from a continuously driven qubit into the steady state. The resulting entangled photonic modes could be transferred to quantum memories for quantum information processing and entanglement distribution. This approach is relevant for the quantum computing, communication, and sensing communities, enhancing the scalability and practicality of entanglement generation across distributed QC systems.

While the experiments in the papers employ transmon-qubit-based systems, the approaches are platform-agnostic and can be extended to other systems, such as trapped-ion qubits [9, 133, 134], neutral atoms [10, 11, 135], semiconductor quantum dots [12, 13, 136, 137], and color-center qubits [14, 15, 138, 139].

4.2 Outlook

In a distributed QC system, our goal is to establish quantum communication channels between remotely separated quantum chips using travelling microwave photons (Fig. 4.1). The quantum information is carried by a photon emitted from one quantum circuit, which travels through the quantum channel and is subsequently reabsorbed by the receiving circuit. This process facilitates quantum state transfer

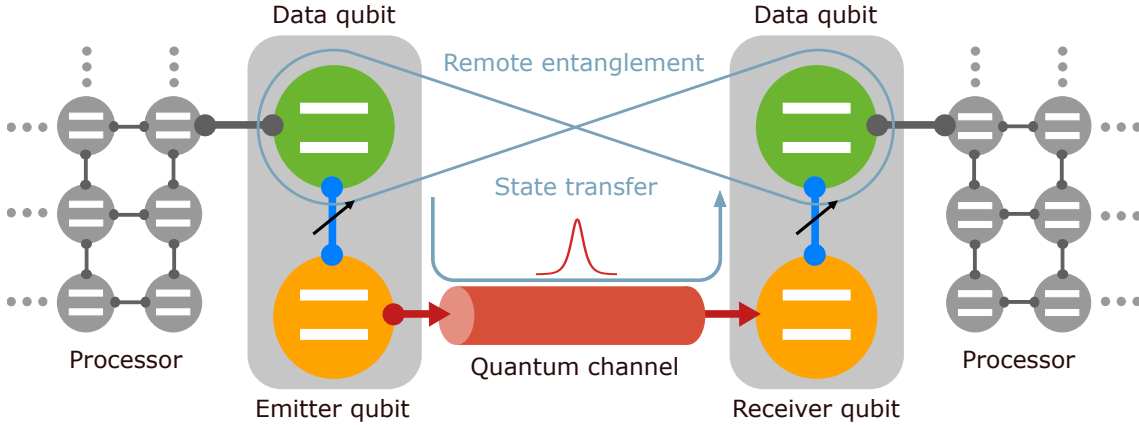


Figure 4.1: The potential distributed quantum computing system utilizing modular building blocks implemented by this thesis.

and enables the creation of remote entanglement between qubits in both circuits. Additionally, by coupling more qubits to this system, it can be scaled to solve larger computational tasks.

In this thesis, we present a photon emission system capable of both state transfer and entanglement generation using single-rail and dual-rail propagating modes, both implementable on the same device. The dual-rail scheme, utilizing frequency-bin encoding, supports error detection, while the single-rail scheme operates without it. This system thus supports photon emission with or without frequency-bin encoding, providing flexibility to integrate or bypass error detection protocols within the same device. Although photon reabsorption is not covered in the thesis, it can be implemented through a time-reversed version of the emission process. Note that in the receiver device, the receiver qubit should have the same frequency as the emitter qubit. This frequency alignment can be achieved by making the qubits flux-tunable using a SQUID. The quantum channel, which physically links the coplanar waveguides of the emitter and receiver, can be implemented with a coaxial cable [41] and may include a circulator, as referenced in Sec. 1.1. This provided system has the potential to serve as a critical building block for future distributed quantum computing and quantum networks.

In the following sections, we explain the whole process of implementing quantum state transfer, including both photon emission and reabsorption, with single-rail or dual-rail propagating modes. For the dual-rail case, we explain why it can function as an error detection protocol for photon loss. Additionally, we discuss potential applications of a distributed QC system.

4.2.1 Potential distributed QC system

Single-rail distributed QC without error detection

Building on the single-rail photon emission described in Sec. 3.1 and the photon shaping technique outlined in Sec. 3.2, we can implement quantum state transfer and establish remote entanglement between two quantum devices by employing the

same hardware and utilizing a time-reversed process for photon reception. Figure 4.2 illustrates the gate sequence used to perform quantum state transfer. It is important to note, however, that with single-rail photons, the system cannot detect errors in the event of photon loss during transmission.

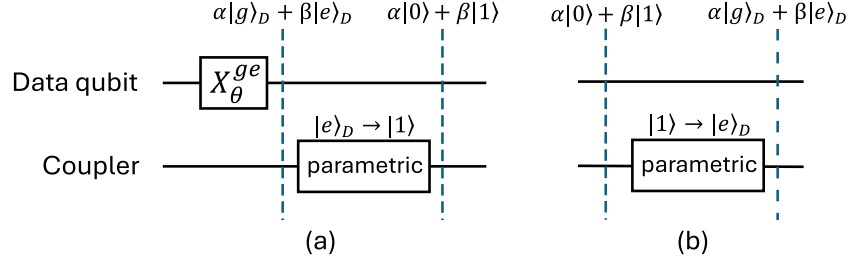


Figure 4.2: Gate sequence for quantum state transfer in a distributed quantum computing system (without error detection), including (a) the emitter processor, and (b) the receiver processor. The X_{θ} gate initializes the data qubit into an arbitrary superposition state between states $|g\rangle$ and $|e\rangle$.

Dual-rail distributed QC with error detection

In this section, we explore the quantum state transfer with frequency-bin-encoding protocol in a distributed QC system, which consists of two quantum processors: a photon-mode emitter (explained in Sec. 3.3) and a photon-mode receiver. The distributed QC system can be demonstrated by reshaping the frequency-bin photonic modes as in Sec. 3.2 and using an identical device for photon re-absorption. In the emission process, after state preparation, by applying the parametric and second-order-transition drives simultaneously, the frequency-bin-encoded photon is generated [Fig. 4.3(a)]. After the transmission of the photon through the quantum channel, the receiver re-absorbs the photon in the reversed process [Fig. 4.3(b)]. In time-bin encoding [52, 53], the two time bins are released by sequentially applying the identical pair of drives. Conversely, in the frequency-bin encoding we utilize, the two frequency bins are generated at the same time. Thus, in principle, frequency-bin encoding is twice as fast as time-bin encoding, under the same hardware condition.

If the photon is transmitted successfully, the data qubit at the receiver's processor ends in the expected superposition state $\alpha|g\rangle_D + \beta|e\rangle_D$. However, if any part of the photon state is lost, similar to time-bin encoding [52, 53], the qubit state will end up in the $|f\rangle_D$ state due to the last two quantum gates in the reabsorption process [Fig. 4.4 and Table 4.1]. A quantum non-demolition measurement [140–142] can be used to distinguish between the $|f\rangle_D$ state and the subspace of $|e\rangle_D$ and $|g\rangle_D$, without disturbing the superposition within the subspace itself. This enables the detection of photon loss without disturbing the successfully transferred quantum state, preserving it for further computation.

4.2.2 Applications of distributed QC systems

The distributed QC system can serve as a foundation for modular quantum computing architectures [143]. Using circuit cutting techniques [144], the system allows dividing

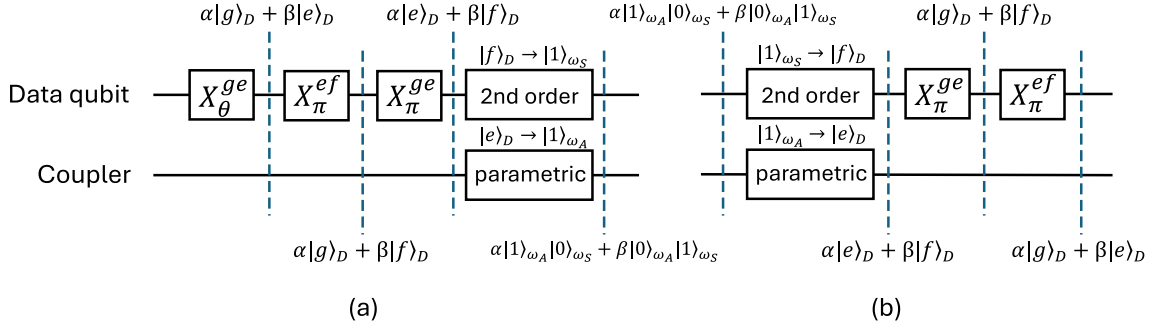


Figure 4.3: Gate sequence for quantum state transfer using frequency-bin encoded photon in a distributed quantum computing system, including (a) the emitter processor, and (b) the receiver processor. The X_θ gate initializes the data qubit into an arbitrary superposition state between states $|g\rangle$ and $|e\rangle$. The X_π gates represent the Pauli- \bar{X} gate, implemented by π -pulses at the transition frequencies of data qubit ω_{ge} and ω_{ef} .

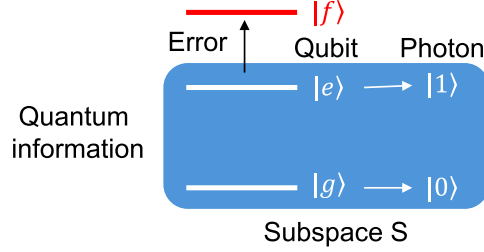


Figure 4.4: By adding another degree of freedom (frequency-bin), the error will lead to leaving the subspace S of the quantum information mapping.

Table 4.1: Frequency-bin encoding as an error-detection protocol for photon loss. If any of the two photonic modes is lost during the transmission, we will end up in the transition of $|0\rangle_{\omega_A}|0\rangle_{\omega_S}$ state. Specifically, applying photon annihilation operator $\hat{a}_A \otimes \hat{I}$ or $\hat{I} \otimes \hat{a}_S$ on the success state results in state $|0\rangle_{\omega_A}|0\rangle_{\omega_S}$. Consequently, this leads to the collapse of the data qubit into the $|f\rangle_D$ state in the receiver processor, instead of the desired superposition state in the information-mapping subspace $\{|g\rangle_D, |e\rangle_D\}$.

	Transmitted photon state	Qubit at the receiver
Success	$\alpha 1\rangle_{\omega_A} 0\rangle_{\omega_S} + \beta 0\rangle_{\omega_A} 1\rangle_{\omega_S}$	$\alpha g\rangle_D + \beta e\rangle_D$
Photon loss	$ 0\rangle_{\omega_A} 0\rangle_{\omega_S}$	$ f\rangle_D$

complex circuits into smaller, manageable segments that are processed and integrated efficiently within the distributed QC framework, enabling scalable and flexible quantum processing. Its capabilities can be further extended by incorporating microwave-to-optical transducers [17, 18, 21], which facilitate quantum information transfer over long distances. This extended distributed QC system supports a variety of applications, including quantum key distribution [145, 146] and quantum networking [147].

Distributed QC systems offer a promising platform for Ericsson to scalably explore complex telecommunications challenges such as antenna tilt optimization,

peak-to-average-power-ratio minimization, feature selection, and compressed feature representation [148–150]. To effectively leverage these systems, we at Ericsson, identify relevant telecom use cases, develop quantum/hybrid algorithms, map these algorithms to the multi-chip QC system, and execute them with the quantum channel facilitating the inter-chip communication.

Chapter 5

Appendix

This chapter presents an overview of the measurement setups and characterization techniques employed in this work. Section 5.1 details the room-temperature measurement setups, including the continuous-wave and pulsed configurations. These setups form the basis for the device characterization procedures discussed in Sec. 5.2, as well as the experiments shown in Chapter 3.

5.1 Room-temperature measurement setup

This section describes the room-temperature measurement setup used in the experiments, including both continuous-wave and pulsed configurations. Note that all room-temperature equipment is connected to the same 10 MHz external clock to ensure phase synchronization.

5.1.1 Continuous-wave setup

In the experiment, when we use the continuous-wave setup, the quantum device is connected to the room-temperature measurement equipment as shown in Fig. 5.1. In this configuration, the transmission line of the device is connected to the input and output ports of a vector network analyzer (VNA). By sweeping the VNA's probing frequency around the resonant frequencies of the resonator or qubit, we record the transmission coefficient S_{21} , defined as

$$S_{21} = \frac{V_{\text{out}}}{V_{\text{in}}}, \quad (5.1)$$

where V_{out} and V_{in} represent the voltage amplitudes at the VNA's output and input ports, respectively. Similarly, the reflection coefficient S_{11} is measured by connecting the VNA to the input and output ports of a circulator connected to the waveguide probe line, with S_{11} defined in the same manner.

This continuous-wave setup allows us to perform single-tone and two-tone spectroscopy of the readout resonators and qubits. Single-tone spectroscopy involves applying a continuous-wave signal at varying frequencies to the readout resonators, enabling us to observe the resonator's response and determine parameters including

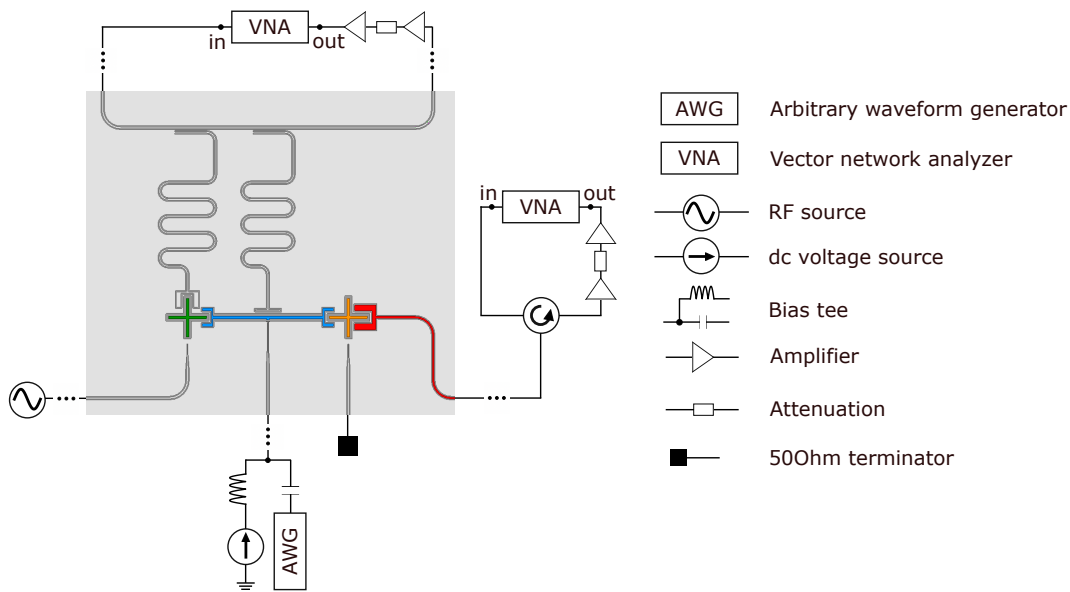


Figure 5.1: Continuous-wave setup. The cryogenic components are omitted for simplicity (indicated by the three dots along each line).

the resonance frequency and the quality factor. Two-tone spectroscopy, on the other hand, involves sending a second signal to drive the qubit while fixing the first continuous-wave signal at the resonator's frequency. This technique helps in probing the interactions between qubits and readout resonators, and can be used to extract information about qubit transition frequency, anharmonicity, and coupling strengths.

5.1.2 Pulsed setup

In the pulsed setup [Fig. 5.2], up-conversion and down-conversion techniques play a critical role in controlling signal frequencies and phases, as well as enabling precise measurements on the devices. Up-conversion is required to shift low-frequency signals generated by the arbitrary waveform generator (AWG) to higher frequencies suitable for driving tones on the device, as typical AWGs cannot directly generate signals at such high frequencies. This is achieved by mixing the low-frequency signal with a high-frequency tone from the local oscillator (LO). Conversely, down-conversion is used to shift high-frequency response signals back to a lower frequency range, enabling measurement and analysis by producing signals slow enough to be digitized without the risk of under-sampling. By using the same LO for both up-conversion and down-conversion, we ensure phase coherence and frequency consistency between the transmitted and received signals. The IQ mixer plays a central role in facilitating both up- and down-conversions.

Up-conversion and mixer calibration

In the up-conversion process, an intermediate frequency (ω_{IF}), typically a few hundred MHz and generated by an AWG, is combined with a LO signal at frequency ω_{LO} through a mixer. This process produces a radio frequency (RF) signal, which we

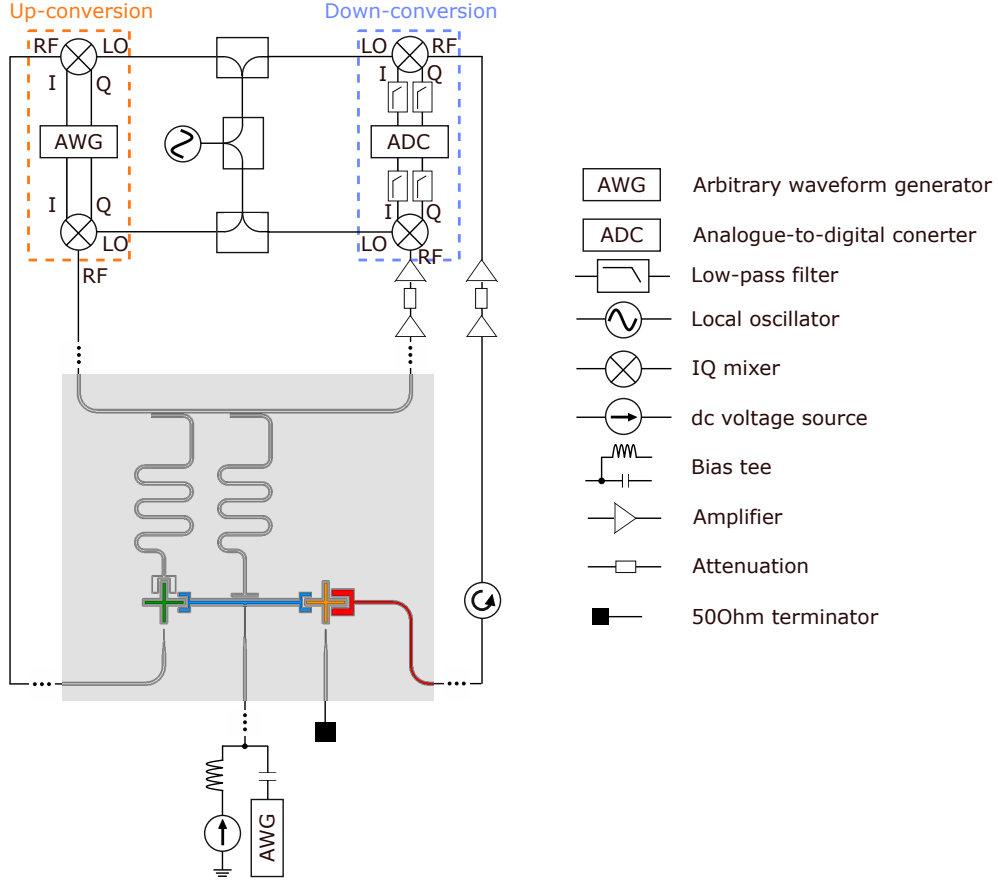


Figure 5.2: Pulsed setup. The cryogenic components are omitted for clarity (indicated by the three dots along each line). Using the Vivace microwave transceiver platform [111], the Vivace AWG delivers microwave control pulses to drive the emitter, while the analog-to-digital converter (ADC) samples the data during readout.

typically chose to be in the range of 4 GHz to 8 GHz, described as,

$$s_{\text{RF}}(t) = \cos(\omega_{\text{IF}}t) \cos(\omega_{\text{LO}}t) = \frac{1}{2} [\cos((\omega_{\text{LO}} - \omega_{\text{IF}})t) + \cos((\omega_{\text{LO}} + \omega_{\text{IF}})t)], \quad (5.2)$$

which results in two sidebands at the frequencies of $\omega_{\text{RF}} = \omega_{\text{LO}} + \omega_{\text{IF}}$ (right sideband) and $\omega_{\text{LO}} - \omega_{\text{IF}}$ (left sideband). However, we aim to isolate a single sideband and use it as the input to our device. Therefore, an IQ mixer, a combination of two normal mixers with a $\pm\pi/2$ phase shift between their LO ports, is employed. The signal then becomes,

$$s_{\text{RF}}(t) = \cos(\omega_{\text{IF}}t) \cos(\omega_{\text{LO}}t) \mp \sin(\omega_{\text{IF}}t) \sin(\omega_{\text{LO}}t) = \cos((\omega_{\text{LO}} \pm \omega_{\text{IF}})t). \quad (5.3)$$

We are only left with one single sideband, the left sideband with frequency $\omega_{\text{LO}} - \omega_{\text{IF}}$ or the right sideband with frequency $\omega_{\text{LO}} + \omega_{\text{IF}}$. Note that the resulting sideband is influenced not only by the phase shift at the IQ mixer's LO port, which is fixed, but also by how the two IQ IF signals are connected to the mixer and their relative phase shifts. This provides us with the flexibility to effectively select the desired sideband for further processing according to our needs.

In our experiments, the selected sideband cannot be obtained perfectly as described before, due to the inidealities of the physical IQ mixer. LO leakage occurs when a portion of the strong local oscillator signal bypasses the mixing process and directly propagates to the sample. Additionally, if the I and Q channels are not perfectly balanced in phase and amplitude, the unselected sideband can also appear. We thus need to calibrate the IQ mixers at the frequencies of the device tones. The calibration is performed on the IQ mixers used for up-conversion to ensure the purity of the signals transmitted into the device. This calibration is performed by measuring the RF port of the IQ mixer using a spectrum analyzer while the IQ ports are driven by an arbitrary waveform generator (AWG) and the local oscillator (LO) is engaged. Prior to calibration, the frequency spectrum exhibits three distinct peaks: $\omega_{\text{LO}} - \omega_{\text{IF}}$, ω_{LO} , and $\omega_{\text{LO}} + \omega_{\text{IF}}$. To eliminate the undesired peak at the LO frequency (ω_{LO}), we adjust the DC bias of the IQ pulses generated by the AWG. Additionally, the unwanted sideband peak can be suppressed by fine-tuning the amplitude scaling and phase difference between the IQ pulses. After completing the mixer calibration, only the desired sideband peak remains in the frequency domain, with the unwanted peaks effectively suppressed.

Down-conversion and demodulation

In the down-conversion process, the high-frequency RF signal measured at frequency ω_{RF} is converted to a lower-frequency IF signal (ω_{IF}) using another IQ mixer and the same local oscillator (LO) signal at frequency ω_{LO} , for the IF signal to be processed by an analogue-to-digital converter (ADC). In the IQ mixer, the RF signal is mixed with LO which are propagating out from the I and Q ports of the mixer at (ideally) $\pm\pi/2$ phase shift, given by,

$$I(t) = \cos(\omega_{\text{RF}}t) \cos(\omega_{\text{LO}}t) = \frac{1}{2} [\cos((\omega_{\text{RF}} + \omega_{\text{LO}})t) + \cos((\omega_{\text{RF}} - \omega_{\text{LO}})t)] , \quad (5.4)$$

$$Q(t) = \cos(\omega_{\text{RF}}t) \sin(\pm\omega_{\text{LO}}t) = \pm\frac{1}{2} [\sin((\omega_{\text{RF}} + \omega_{\text{LO}})t) - \sin((\omega_{\text{RF}} - \omega_{\text{LO}})t)] . \quad (5.5)$$

After applying low-pass filters to remove the high-frequency components at $\omega_{\text{RF}} + \omega_{\text{LO}}$, the I and Q components become,

$$I_{\text{LPF}}(t) = \frac{1}{2} \cos((\omega_{\text{RF}} - \omega_{\text{LO}})t) , \quad (5.6)$$

$$Q_{\text{LPF}}(t) = \mp\frac{1}{2} \sin((\omega_{\text{RF}} - \omega_{\text{LO}})t) . \quad (5.7)$$

When $\omega_{\text{RF}} > \omega_{\text{LO}}$, it corresponds to the right sideband. When $\omega_{\text{LO}} > \omega_{\text{RF}}$, it corresponds to the left sideband. Combining the I and Q components, we form a complex signal. Similar to the up-conversion process, the configuration of the IQ mixer allows us to select the desired sideband during down-conversion.

The filtered I and Q components $I_{\text{LPF}}(t)$ and $Q_{\text{LPF}}(t)$ are then sent to the ADC module for sampling. The sampled signal, denoted as $s_{\text{DC}}(t) = I_{\text{DC}}(t) + iQ_{\text{DC}}(t)$, where DC indicates down-converted, is subsequently demodulated digitally on the computer. The demodulation process involves down-converting this signal at the

demodulation frequency $\omega_{\text{demod}} = \omega_{\text{IF}} = |\omega_{\text{RF}} - \omega_{\text{LO}}|$. This is achieved by multiplying by treating the IQ parts of $s(t)$ separately,

$$s_{\text{demod}_{1I}}(t) = I_{\text{DC}}(t) \cos(\omega_{\text{IF}}t), \quad (5.8)$$

$$s_{\text{demod}_{1Q}}(t) = I_{\text{DC}}(t) \sin(\omega_{\text{IF}}t), \quad (5.9)$$

$$s_{\text{demod}_{2I}}(t) = Q_{\text{DC}}(t) \cos(\omega_{\text{IF}}t), \quad (5.10)$$

$$s_{\text{demod}_{2Q}}(t) = Q_{\text{DC}}(t) \sin(\omega_{\text{IF}}t). \quad (5.11)$$

Since $I_{\text{DC}}(t)$ and $Q_{\text{DC}}(t)$ also have a frequency of ω_{IF} , each of the four components in Eqs. (5.9)–(5.11) contains two frequency components after the demodulation: one at zero frequency and another at $2\omega_{\text{IF}}$. Digital low-pass filters are used to remove the double-frequency component, leaving only the zero-frequency component for all four traces, which represent the baseband information as a function of time. Denoting the filtered traces as $\{s_{\text{filter}_{1I}}(t), s_{\text{filter}_{1Q}}(t), s_{\text{filter}_{2I}}(t), s_{\text{filter}_{2Q}}(t)\}$, corresponding to $\{s_{\text{demod}_{1I}}(t), s_{\text{demod}_{1Q}}(t), s_{\text{demod}_{2I}}(t), s_{\text{demod}_{2Q}}(t)\}$ respectively, the desired baseband signal $s_{\text{BB}}(t) = I_{\text{BB}}(t) + iQ_{\text{BB}}(t)$ is given by,

$$I_{\text{BB}}(t) = s_{\text{filter}_{1I}}(t) \pm s_{\text{filter}_{2Q}}(t), \quad (5.12)$$

$$Q_{\text{BB}}(t) = s_{\text{filter}_{2I}}(t) \mp s_{\text{filter}_{1Q}}(t), \quad (5.13)$$

where the \pm and \mp signs depend on the selected sideband.

5.2 Device characterization measurements

In this section, we outline the device characterization process, primarily conducted on Device 1, with the exception of the measurements of longitudinal and transverse relaxation time, which are specifically performed on Device 2.

5.2.1 From continuous-wave setup

Single-tone spectroscopy of readout resonators

For the continuous-wave step of the measurement, we connect the device transmission line to the input and output port of a VNA and record S_{21} . When the VNA power is set to a low level, the qubit-resonator system is in the dressed state, as illustrated by the blue curve in Fig. 5.3(a). In this configuration, we operate in the dispersive regime, where the system dynamics are governed by Eq. (1.24). At high power, the qubit becomes effectively decoupled from the resonator, and the system is described by Eq. (1.22), resulting in a shift of the resonator frequency to the bare state basis, as shown by the red curve in Fig. 5.3(a). The frequency shift of the resonator between the bare and dressed modes reads $\chi/2\pi = (\omega_R^{\text{dressed}} - \omega_R^{\text{bare}})/2\pi = 3 \text{ MHz}$.

In both cases, the resonator dip exhibits asymmetric shapes, primarily attributed to impedance mismatching, as discussed in [151]. To model the complex S_{21} spec-

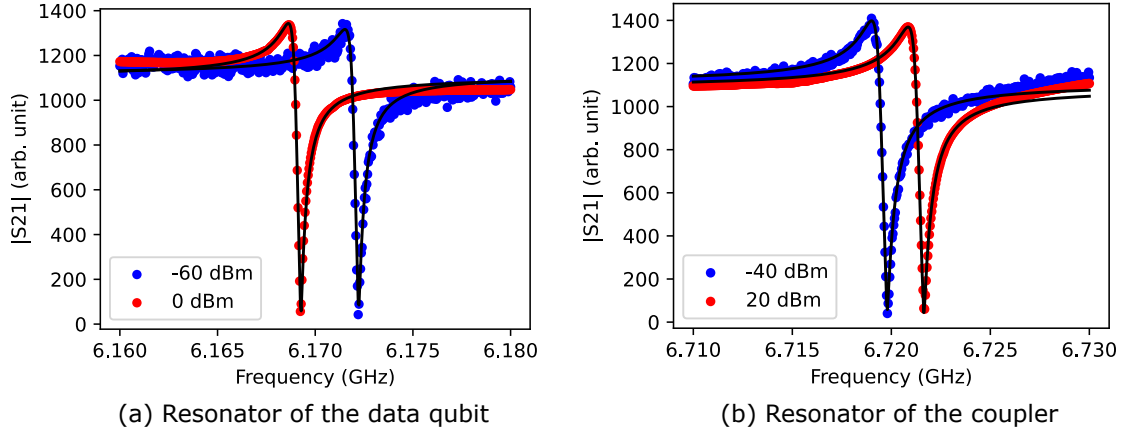


Figure 5.3: Single-tone spectroscopy of the readout resonator of (a) the data qubit and (b) the coupler, showing the magnitude quadrature. The blue (red) curve represents the resonator in a dressed (bare) state. The solid black curves are from the fitting with Eq. (5.14).

troscopy of the resonator, we use the following expression [151, 152],

$$S_{21}(\omega_p) = \underbrace{ae^{i\alpha}e^{-i\omega_p\tau}}_{\text{environment}} \underbrace{\left[1 - \frac{(Q_l/|Q_c|)e^{i\phi}}{1 + 2iQ_l\left(\frac{\omega_p}{\omega_R} - 1\right)} \right]}_{\text{ideal resonator}}, \quad (5.14)$$

where the first term counts for contributions from the environment. In the second term, $\omega_p(\omega_R)$ is the probe (resonator) frequency. Q_l is the loaded quality factor and $|Q_c|$ is the absolute value of the coupling quality factor, following $Q_l^{-1} = Q_i^{-1} + \text{Re}\{Q_c^{-1}\}$, where Q_i is the internal quality factor. ϕ quantifies the impedance mismatching. The total decay rate of the resonator can be calculated through $\kappa = \omega_R/Q_l$.

The spectroscopy of the coupler resonator is measured in the same way, when the resonator and the coupler are in the dressed (bare) state when applying low (high) power [blue (red) curve in Fig. 5.3(b)]. Similarly, we compute the frequency shift between the bare and dressed modes of the coupler's resonator, $\chi/2\pi = (\omega_R^{\text{dressed}} - \omega_R^{\text{bare}})/2\pi = -2$ MHz. Note that the sign of the dispersive shift χ is determined by the sign of the detuning $\Delta = \omega_R - \omega_Q$, with ω_R the resonator frequency and ω_Q the qubit or coupler frequency. Specifically, the positive χ indicates the resonator frequency is higher than the data qubit. In contrast, a negative χ indicates that the frequency of the resonator is lower than the frequency of the coupler.

The flux quanta of the coupler is calibrated by observing the single-tone spectroscopy of the coupler resonator as we sweep the dc voltage on the coupler flux line (Fig. 5.4), which is proportional to the applied dc flux.

Single-tone spectroscopy of the emitter qubit

Unlike the data qubit and the coupler, the emitter qubit is not connected to a readout resonator, but to an open-ended, one-dimensional waveguide. Therefore, we

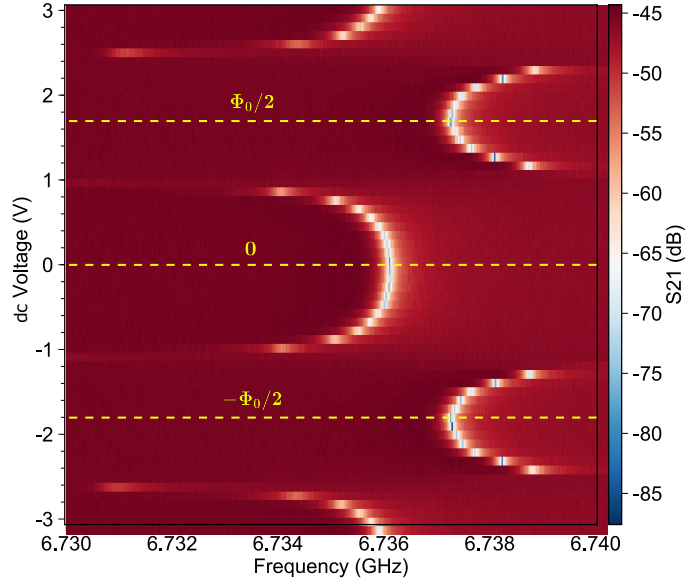


Figure 5.4: Calibration of the flux quanta of the flux-tunable coupler, with the dc voltage values corresponding to $\pm\Phi_0/2$ and 0 highlighted by yellow dashed lines. The remaining applied voltage levels are normalized based on these reference points. The avoided crossing observed in the figure arises from the interaction between the coupler and its resonator during the flux sweep.

characterize it through single-tone measurement obtained from the reflection setup attached to the waveguide to which the qubit is coupled. The S_{11} from the reflection measurement can be modelled by Eq. (1.32), by assuming the pure dephasing rate Γ_φ is zero. In the equation, Ω is the drive strength, following [125],

$$\Omega = 2\sqrt{\frac{P_{\text{in}}A\Gamma_E}{\hbar\omega_E}}, \quad (5.15)$$

where P_{in} is the input power from VNA and A is the total attenuation in the line. Utilizing Eq. (1.32) and (5.15) for a global fitting on all curves, the experimentally obtained S_{11} can be modelled by employing the detuning Δ , the decay rate Γ_E , the non-radiative decay rate Γ_{nr} , and attenuation A as adjustable parameters. Note that in Eq. (1.32), the radiative decay rate Γ_E is denoted as Γ for simplicity.

Two-tone spectroscopy of qubit

To estimate the qubit's frequency, we read out at the dressed resonator frequency while applying an additional signal from a local oscillator, tuned around the qubit's frequency, through the charge line of the data qubit. A peak in the measured S_{21} is expected at the qubit's frequency, due to the qubit-state-dependent shift [$\delta\omega_r = -\frac{j^2 E_C}{\Delta(\Delta - E_C)}$, not shown as a figure in this thesis] in the resonator frequency when the drive signal matches the qubit's frequency.

As illustrated in Fig. 5.6, when the power applied to the charge line is low, two distinct peaks are observed (blue curve). The first peak (right) corresponds to the transition from the ground state to the first excited state of the qubit (ω_D^{ge}), while the

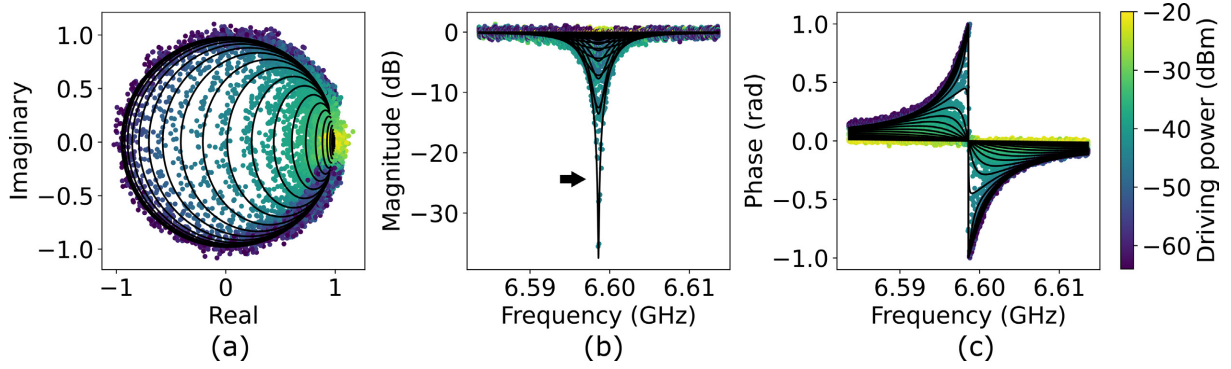


Figure 5.5: Single-tone spectroscopy of the emitter qubit, while sweeping the drive power. The solid black curve is from the global fit. The black arrow marks the S_{11} magnitude measured at the critical power, which shows the deepest dip compared to the other powers.

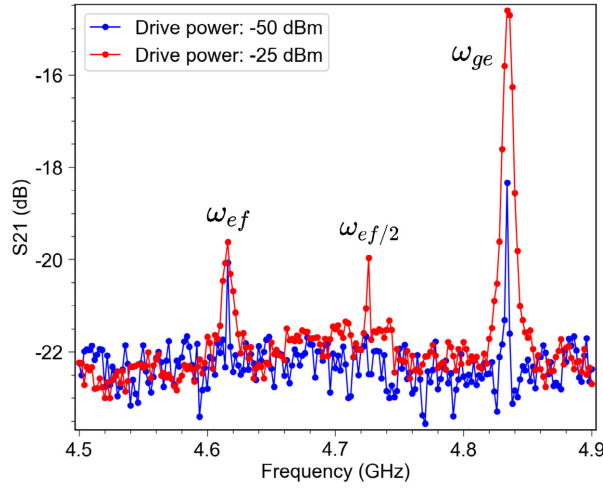


Figure 5.6: Two-tone spectroscopy of the data qubit, with the blue (red) curve representing the low (high) power.

second peak (left) represents the transition from the first excited state to the second excited state (ω_D^{ef}). Upon increasing the power (red curve), while the broadening of the mentioned two peaks, an additional peak emerges in the middle, which is associated with the two-photon transition between the ground state $|g\rangle$ and the second excited states $|f\rangle$, mediated by a virtual state. From these observations, the anharmonicity of the data qubit can be obtained by $\alpha = \omega_D^{ef} - \omega_D^{ge}$.

What is more, knowing the qubit transition frequency ω_D^{ge} , we can calculate the coupling between qubit and resonator, j , through

$$\chi = \frac{j^2}{\Delta}. \quad (5.16)$$

Here, χ denotes the frequency shift associated with the state measured above, while Δ signifies the detuning between the qubit and the resonator.

Two-tone spectroscopy of the flux-tunable coupler

The coupler on this processor is connected to a SQUID and an inductively-coupled flux line, allowing its frequency ω_C to be tuned by adjusting the flux, following Eq. (1.21),

$$\omega_C(\Phi) = \omega_{C,0} \sqrt{|\cos(\pi\Phi/\Phi_0)|}, \quad (5.17)$$

where $\omega_{C,0}$ is the coupler frequency with zero dc flux bias, and Φ is the applied external flux and Φ_0 is the flux quantum. By adjusting the dc voltage applied to the coupler flux line, which is proportional to the flux flows in the SQUID, we tune the coupler frequency accordingly. Figure 3.3 shows the coupler frequency as a function of the dc flux, which is obtained from the two-tone spectroscopy of the coupler. We drive the coupler resonator at its dressed frequency and pump the coupler through the charge line of the data qubit, as the coupler itself does not have a directly coupled charge line. Again, we can obtain the coupling strength j between the coupler and its resonator through Eq. (5.16).

5.2.2 From pulsed setup

Using a pulsed setup, we can measure the single-tone and two-tone spectroscopy of qubits and resonators; however, to avoid redundancy, we will not present these results again. In this section, we demonstrate the characterization of the data qubit by measuring its relaxation and coherence times and evaluating the impact of Purcell decay.

Time-resolved measurement of the data qubit

In the experiment, we measure the Rabi oscillation, longitude relaxation time (T_1), and transverse relaxation time (T_2) of the data qubit between the first-excited and the ground states, and that between the second- and the first-excited states.

The Rabi oscillation measurement enables us to find the π -pulse for driving the qubit. A π -pulse is created by combining a sinusoidal signal oscillating at the qubit's frequency with an envelope, where the pulse power is controlled by adjusting either the amplitude or the duration of the pulse. In this experiment, we fix the length and change the amplitude of the π -pulse, which we will then use to measure T_1 and T_2 in the following experiments.

Consistent with our previous experiment, we perform readout at the dressed resonator frequency after resonantly driving the qubit through the charge line. As illustrated in Fig. 5.7(a-b), we maintain a constant duration (100 ns) and shape (Gaussian) for the qubit drive pulse while varying its amplitude. This approach allows us to observe oscillations in the qubit population between the ground and excited states. From these Rabi oscillations, we determine the pulse amplitude that corresponds to a π -pulse of the qubit. Additionally, in Fig. 5.7(c-d), we extend the measurement by sweeping the drive frequency alongside the pulse amplitude, thereby acquiring the Chevron pattern.

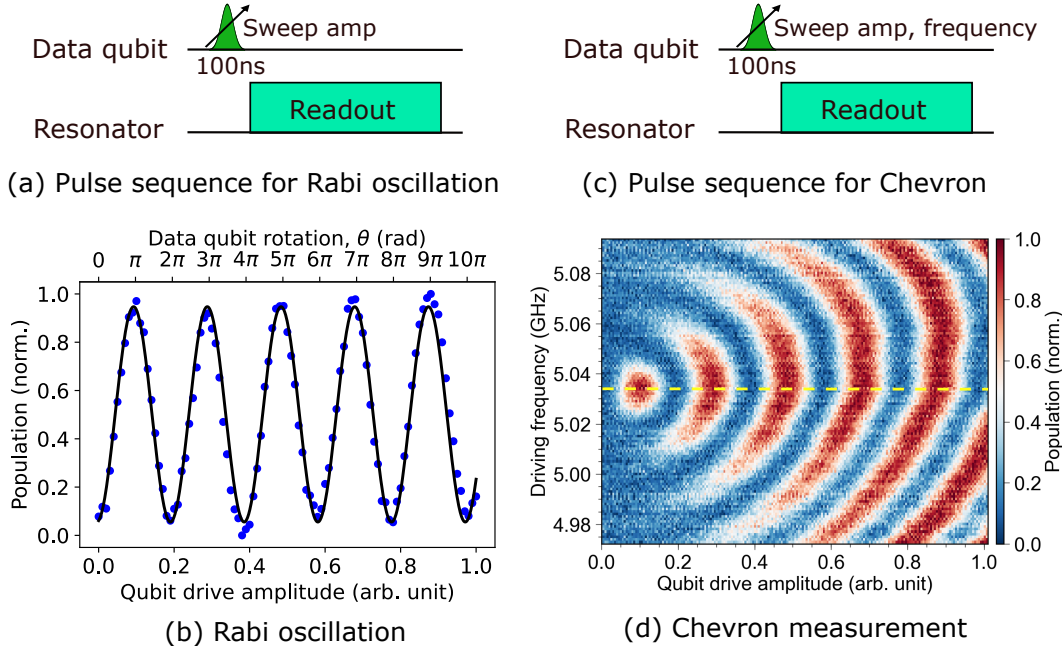


Figure 5.7: (a-b) Pulse sequence and corresponding measured results of Rabi oscillations when the drive pulse frequency is on resonance with the data qubit frequency. The blue dotted points in (b) represent the measured data, while the solid black line corresponds to the sinusoidal fit. (c-d) Pulse sequence and measured results of Rabi oscillations while sweeping the drive pulse frequency, commonly referred to as Chevron measurements. The case highlighted with the yellow dashed line corresponds to panel (b).

To accurately determine the π -pulse amplitude, we perform a calibration procedure aimed at identifying the optimal pulse amplitude for subsequent time-resolved measurements. As illustrated in Fig. 5.8(a), we apply an odd number of π -pulses to the data qubit and subsequently perform qubit readout. The amplitude of each π -pulse is finely adjusted within a narrower range, as determined from Fig. 5.7(b). Regardless of the number of π -pulses applied, a consistent peak emerges at the same amplitude, indicating the calibrated π -pulse. This optimal amplitude is highlighted by the yellow dashed line in Fig. 5.8(b).

We then measure the longitudinal relaxation time, T_1 , of the data qubit, by reading out the qubit after applying a π -pulse and waiting a certain amount of time τ [Fig. 5.9(a)]. The π -pulse excites the qubit, which relaxes exponentially during the time τ . By measuring qubit population at different τ , we can draw the exponential decay and extract the relaxation time $T_1 = 19.9 \mu\text{s}$ [Fig. 5.9(b)], by fitting it according to $y = A \exp(-t/T_1) + B$, with A and B the constant scaling and offset.

Similarly, by following the pulse sequence in Fig. 5.9(c), we operate Ramsey measurement and obtain the transverse relaxation time T_2 . A Ramsey measurement involves applying two $\pi/2$ pulses separated by a variable delay τ . By measuring the population of the qubit at different τ , we obtain a series of oscillations that decay exponentially due to decoherence, and this decay yields T_2 . By fitting it according to $y = A \cos(Bt + \phi) \exp(-t/T_2) + C$, we extract $T_2 = 13.9 \mu\text{s}$, with A, B, C and ϕ representing the constants for scaling, detuning, offset and phase, respectively.

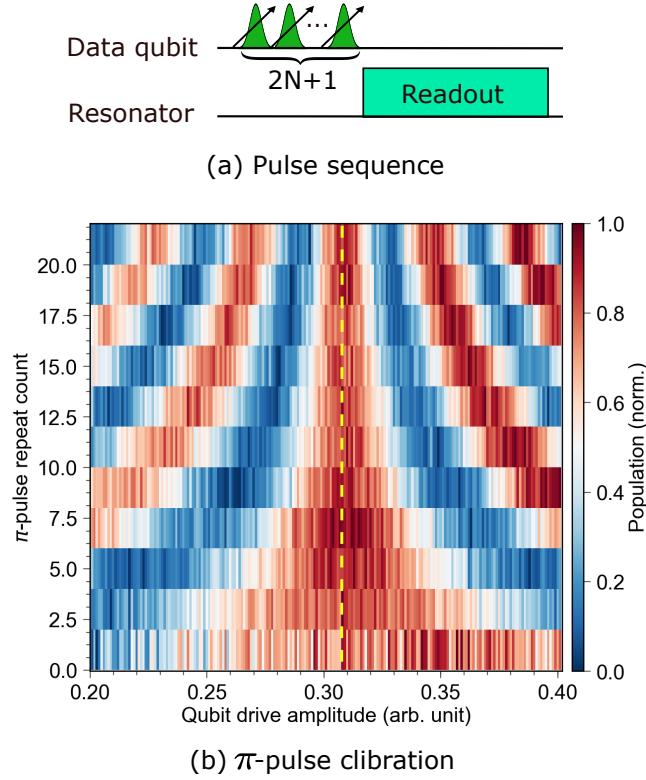


Figure 5.8: π -Pulse amplitude calibration for the data qubit. (a) Pulse sequence applying an odd number ($2N + 1$, with N ranges from 1 to 10) of π -pulses to the qubit while sweeping the pulse amplitude. (b) Measured qubit population as a function of pulse amplitude. The yellow dashed line indicates the optimal amplitude corresponding to a π -pulse.

Ramsey interferometry is a more accurate way of measuring the qubit frequency than qubit two-tone spectroscopy. When the drive pulse is on the resonance of the qubit frequency, we can see an exponential-decaying curve [Fig. 5.9(d), red curve]; however, if they are off-resonance, we can see cosine oscillation, which oscillates with the detuning frequency $|\omega_D^{ge} - \omega_d|$, together with the decay [Fig. 5.9(d), blue curve]. Note that Table 2.2 presents the T_1 and T_2 statistics, including their means and standard deviations, obtained from repeated measurements.

In the above paragraphs, we introduce, by default, the measurement of the relaxation time between the first-excited state and the ground state of the data qubit. Figure 5.10 illustrates the relaxation time measured between the second- and first-excited states of the data qubit. Although the decay from the second-excited state involves sequential relaxation from $|f\rangle$ to $|e\rangle$ and then to $|g\rangle$, we can still fit the decay curves using the same single exponential expressions as before, when the readout is selective enough for the $|f\rangle$ state. By doing so, we extract $T_1^{ef} = 25.3 \mu\text{s}$ and $T_2^{ef} = 4.9 \mu\text{s}$. We measure larger T_1^{ef} than T_1^{ge} , which can be attributed to the weaker coupling of the system to the environment at ω_D^{ef} compared to ω_D^{ge} .

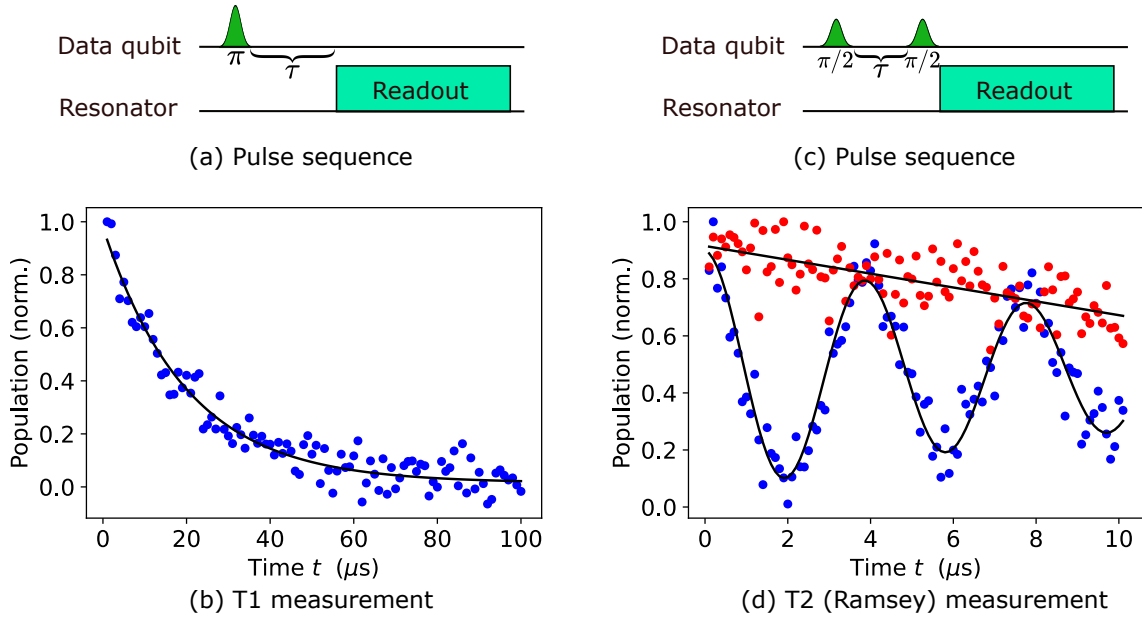


Figure 5.9: Measurement of the T_1 and T_2 of the data qubit between the first excited state and the ground state. (a-b) Pulse sequence and corresponding measured time trace of T_1 . (c-d) Pulse sequence and corresponding measured time traces of T_2 . Note that we measure at two different cases, when the data qubit is driven on resonance (red) and when the data qubit is driven with detuning 0.25 MHz. The solid black curves are the fit.

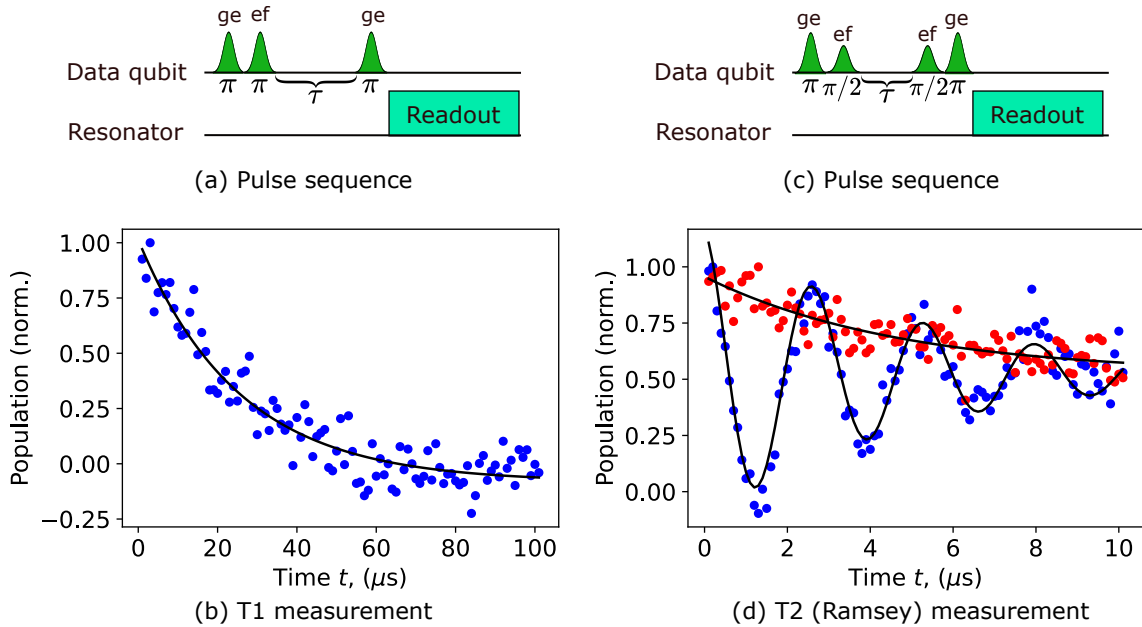


Figure 5.10: Measurement of the T_1^{ef} and T_2^{ef} , relaxation time between the second and the first excited states of the data qubit. (a-b) Pulse sequence and corresponding measured time trace of T_1^{ef} . (c-d) Pulse sequence and corresponding measured time traces of T_2^{ef} . Note that we measure at two different cases, when the data qubit is driven on resonance (red) and when the data qubit is driven with detuning 0.4 MHz. The solid black curves are the fit.

Purcell decay from the emitter qubit to the data qubit

The Purcell decay typically refers to qubit relaxation due to its coupling to a readout resonator, which is in turn coupled to the environment. Here, we extend this concept to the data qubit, which is coupled to a highly decaying emitter qubit, causing an unintended decay of the data qubit into the waveguide, regardless of the control pulses. When estimating the Purcell decay rate, κ_p , we consider two primary contributions: the capacitive interaction between the qubits, g_{DE} , and the static coupling rate between the two qubits, J_{dc} , achieved after positioning the coupler at its operating frequency. The Purcell decay rate is given by,

$$\kappa_p = \left(\frac{g_{DE} + J_{dc}}{\Delta_{DE}} \right)^2 \Gamma_E. \quad (5.18)$$

The interaction term g_{DE} remains unaffected as we adjust the coupler frequency and is defined by,

$$g_{DE} = \frac{C_{DE}}{\sqrt{C_{\Sigma,D}C_{\Sigma,E}}} \sqrt{\omega_D \omega_E} \quad (5.19)$$

where C_{DE} is the mutual capacitance of the two qubits, and $C_{\Sigma,D}$ ($C_{\Sigma,E}$) is the total capacitance of the data (emitter) qubit. From simulations of the device's capacitance matrix, we obtain $g_{DE}/2\pi=0.07$ MHz.

In Eq. (5.18), with the coupler set at 6 GHz, the static coupling rate is $J_{dc}/2\pi = 1.024$ MHz [calculated through Eq. (3.2)]. Δ_{DE} is the detuning between the two qubits. Based on these values, we calculate the Purcell decay rate as $\kappa_p/2\pi = 0.296$ kHz, which is negligible compared to the measured longitudinal relaxation rate of the data qubit. Therefore, in the current setup and with the chosen dc flux bias, the Purcell decay is not a primary issue, as the lifetime of the data qubit is not limited by Purcell decay into the emitter qubit.

Bibliography

- [1] M. A. Nielsen and I. L. Chuang. *Quantum computation and quantum information*. Vol. 2. Cambridge university press Cambridge, 2001 (cit. on p. 3).
- [2] J. Preskill. “Quantum computing in the NISQ era and beyond”. In: *Quantum*. 2, p. 79 (cit. on p. 3).
- [3] A. G. Fowler, M. Mariantoni, J. M. Martinis, and A. N. Cleland. “Surface codes: Towards practical large-scale quantum computation”. In: *Physical Review A*. 86, p. 032324 (cit. on p. 3).
- [4] M. Reiher, N. Wiebe, K. M. Svore, D. Wecker, and M. Troyer. “Elucidating reaction mechanisms on quantum computers”. In: *Proceedings of the National Academy of Sciences*. 114, pp. 7555–7560 (cit. on p. 3).
- [5] P. Magnard et al. “Microwave Quantum Link between Superconducting Circuits Housed in Spatially Separated Cryogenic Systems”. In: *Physical Review Letters*. 125, p. 260502 (cit. on pp. 3–5).
- [6] S. Krinner, S. Storz, P. Kurpiers, P. Magnard, J. Heinsoo, R. Keller, J. Luetolf, C. Eichler, and A. Wallraff. “Engineering cryogenic setups for 100-qubit scale superconducting circuit systems”. In: *EPJ Quantum Technology*. 6, p. 2 (cit. on pp. 3, 20, 21).
- [7] J. I. Cirac, P. Zoller, H. J. Kimble, and H. Mabuchi. “Quantum State Transfer and Entanglement Distribution among Distant Nodes in a Quantum Network”. In: *Physical Review Letters*. 78, pp. 3221–3224 (cit. on p. 4).
- [8] H. J. Kimble. “The quantum internet”. In: *Nature*. 453, pp. 1023–1030 (cit. on p. 4).
- [9] V. Krutyanskiy et al. “Entanglement of Trapped-Ion Qubits Separated by 230 Meters”. In: *Physical Review Letters*. 130, p. 050803 (cit. on pp. 4, 65).
- [10] J. Hofmann, M. Krug, N. Ortegel, L. Gérard, M. Weber, W. Rosenfeld, and H. Weinfurter. “Heralded Entanglement Between Widely Separated Atoms”. In: *Science*. 337, pp. 72–75 (cit. on pp. 4, 65).
- [11] S. Ritter, C. Nölleke, C. Hahn, A. Reiserer, A. Neuzner, M. Uphoff, M. Mücke, E. Figueroa, J. Bochmann, and G. Rempe. “An elementary quantum network of single atoms in optical cavities”. In: *Nature*. 484, pp. 195–200 (cit. on pp. 4, 65).

- [12] A. Delteil, Z. Sun, W.-b. Gao, E. Togan, S. Faelt, and A. Imamoglu. “Generation of heralded entanglement between distant hole spins”. In: *Nature Physics*. 12, pp. 218–223 (cit. on pp. 4, 65).
- [13] R. Stockill, M. J. Stanley, L. Huthmacher, E. Clarke, M. Hugues, A. J. Miller, C. Matthiesen, C. Le Gall, and M. Atatüre. “Phase-Tuned Entangled State Generation between Distant Spin Qubits”. In: *Physical Review Letters*. 119, p. 010503 (cit. on pp. 4, 65).
- [14] H. Bernien, B. Hensen, W. Pfaff, G. Koolstra, M. S. Blok, L. Robledo, T. H. Taminiau, M. Markham, D. J. Twitchen, L. Childress, et al. “Heralded entanglement between solid-state qubits separated by three metres”. In: *Nature*. 497, pp. 86–90 (cit. on pp. 4, 65).
- [15] P. C. Humphreys, N. Kalb, J. P. Morits, R. N. Schouten, R. F. Vermeulen, D. J. Twitchen, M. Markham, and R. Hanson. “Deterministic delivery of remote entanglement on a quantum network”. In: *Nature*. 558, pp. 268–273 (cit. on pp. 4, 65).
- [16] H. K. Beukers, M. Pasini, H. Choi, D. Englund, R. Hanson, and J. Borregaard. “Remote-Entanglement Protocols for Stationary Qubits with Photonic Interfaces”. In: *PRX Quantum*. 5, p. 010202 (cit. on p. 4).
- [17] N. Lauk, N. Sinclair, S. Barzanjeh, J. P. Covey, M. Saffman, M. Spiropulu, and C. Simon. “Perspectives on quantum transduction”. In: *Quantum Science and Technology*. 5, p. 020501 (cit. on pp. 4, 68).
- [18] M. Wu, E. Zeuthen, K. C. Balram, and K. Srinivasan. “Microwave-to-Optical Transduction Using a Mechanical Supermode for Coupling Piezoelectric and Optomechanical Resonators”. In: *Physical Review Applied*. 13, p. 014027 (cit. on pp. 4, 68).
- [19] J. G. Bartholomew, J. Rochman, T. Xie, J. M. Kindem, A. Ruskuc, I. Craiciu, M. Lei, and A. Faraon. “On-chip coherent microwave-to-optical transduction mediated by ytterbium in YVO4”. In: *Nature communications*. 11, pp. 1–6 (cit. on p. 4).
- [20] C.-H. Wang, M. Zhang, and L. Jiang. “Generalized Matching Condition for Unity Efficiency Quantum Transduction”. In: *Physical Review Research*. 4, p. L042023 (cit. on p. 4).
- [21] A. Kyle, C. L. Rau, W. D. Warfield, A. Kwiatkowski, J. D. Teufel, K. W. Lehnert, and T. Dennis. “Optically Distributing Remote Two-Node Microwave Entanglement Using Doubly Parametric Quantum Transducers”. In: *Physical Review Applied*. 20, p. 014005 (cit. on pp. 4, 68).
- [22] N. Leung, Y. Lu, S. Chakram, R. Naik, N. Earnest, R. Ma, K. Jacobs, A. Cleland, and D. Schuster. “Deterministic bidirectional communication and remote entanglement generation between superconducting qubits”. In: *npj Quantum Information*. 5, p. 18 (cit. on pp. 4, 48).

- [23] Y. Zhong, H.-S. Chang, A. Bienfait, É. Dumur, M.-H. Chou, C. R. Conner, J. Grebel, R. G. Povey, H. Yan, D. I. Schuster, et al. “Deterministic multi-qubit entanglement in a quantum network”. In: *Nature*. 590, pp. 571–575 (cit. on pp. 4, 5).
- [24] P. Campagne-Ibarcq et al. “Deterministic Remote Entanglement of Superconducting Circuits through Microwave Two-Photon Transitions”. In: *Physical Review Letters*. 120, p. 200501 (cit. on p. 4).
- [25] P. Kurpiers, P. Magnard, T. Walter, B. Royer, M. Pechal, J. Heinsoo, Y. Salathé, A. Akin, S. Storz, J.-C. Besse, et al. “Deterministic quantum state transfer and remote entanglement using microwave photons”. In: *Nature*. 558, pp. 264–267 (cit. on pp. 4, 42, 48).
- [26] C. J. Axline, L. D. Burkhardt, W. Pfaff, M. Zhang, K. Chou, P. Campagne-Ibarcq, P. Reinhold, L. Frunzio, S. Girvin, L. Jiang, et al. “On-demand quantum state transfer and entanglement between remote microwave cavity memories”. In: *Nature Physics*. 14, pp. 705–710 (cit. on p. 4).
- [27] J. Qiu, Y. Liu, J. Niu, L. Hu, Y. Wu, L. Zhang, W. Huang, Y. Chen, J. Li, S. Liu, et al. “Deterministic quantum teleportation between distant superconducting chips”. In: *arXiv preprint arXiv:2302.08756* , (cit. on pp. 4, 5).
- [28] J. Grebel et al. “Bidirectional Multiphoton Communication between Remote Superconducting Nodes”. In: *Physical Review Letters*. 132, p. 047001 (cit. on p. 4).
- [29] K. S. Chou, J. Z. Blumoff, C. S. Wang, P. C. Reinhold, C. J. Axline, Y. Y. Gao, L. Frunzio, M. Devoret, L. Jiang, and R. Schoelkopf. “Deterministic teleportation of a quantum gate between two logical qubits”. In: *Nature*. 561, pp. 368–373 (cit. on p. 4).
- [30] K. G. Fedorov et al. “Experimental quantum teleportation of propagating microwaves”. In: *Science Advances*. 7, eabk0891 (cit. on p. 5).
- [31] C. Zhou, P. Lu, M. Praquin, T.-C. Chien, R. Kaufman, X. Cao, M. Xia, R. S. Mong, W. Pfaff, D. Pekker, et al. “Realizing all-to-all couplings among detachable quantum modules using a microwave quantum state router”. In: *npj Quantum Information*. 9, p. 54 (cit. on p. 5).
- [32] B. Kannan, A. Almanakly, Y. Sung, A. Di Paolo, D. A. Rower, J. Braumüller, A. Melville, B. M. Niedzielski, A. Karamlou, K. Serniak, et al. “On-demand directional microwave photon emission using waveguide quantum electrodynamics”. In: *Nature Physics*. 19, pp. 394–400 (cit. on p. 5).
- [33] A. Almanakly, B. Yankelevich, M. Hays, B. Kannan, R. Assouly, A. Greene, M. Gingras, B. M. Niedzielski, H. Stickler, M. E. Schwartz, et al. “Deterministic remote entanglement using a chiral quantum interconnect”. In: *arXiv preprint arXiv:2408.05164* , (cit. on pp. 5, 45, 48).

- [34] J. Wenner et al. “Catching Time-Reversed Microwave Coherent State Photons with 99.4% Absorption Efficiency”. In: *Physical Review Letters*. 112, p. 210501 (cit. on pp. 5, 44).
- [35] M. Pechal, L. Huthmacher, C. Eichler, S. Zeytinoglu, A. A. Abdumalikov, S. Berger, A. Wallraff, and S. Filipp. “Microwave-Controlled Generation of Shaped Single Photons in Circuit Quantum Electrodynamics”. In: *Physical Review X*. 4, p. 041010 (cit. on pp. 5, 42, 45).
- [36] P. Forn-Díaz, C. W. Warren, C. W. S. Chang, A. M. Vadiraj, and C. M. Wilson. “On-Demand Microwave Generator of Shaped Single Photons”. In: *Physical Review Applied*. 8, p. 054015 (cit. on p. 5).
- [37] Y. Li, Z. Wang, Z. Bao, Y. Wu, J. Wang, J. Yang, H. Xiong, Y. Song, H. Zhang, and L. Duan. “Frequency-tunable microwave quantum light source based on superconducting quantum circuits”. In: *Chip*. 2, p. 100063 (cit. on p. 5).
- [38] X. Li, S.-Y. Li, S.-L. Zhao, Z.-Y. Mei, Y. He, C.-L. Deng, Y. Liu, Y.-J. Liu, G.-H. Liang, J.-Z. Wang, et al. “On-demand shaped photon emission based on a parametrically modulated qubit”. In: *arXiv preprint arXiv:2405.01464* , (cit. on p. 5).
- [39] D. C. McKay, S. Filipp, A. Mezzacapo, E. Magesan, J. M. Chow, and J. M. Gambetta. “Universal Gate for Fixed-Frequency Qubits via a Tunable Bus”. In: *Physical Review Applied*. 6, p. 064007 (cit. on pp. 5, 37).
- [40] J.-C. Besse, K. Reuer, M. C. Collodo, A. Wulff, L. Wernli, A. Copetudo, D. Malz, P. Magnard, A. Akin, M. Gabureac, et al. “Realizing a deterministic source of multipartite-entangled photonic qubits”. In: *Nature communications*. 11, p. 4877 (cit. on pp. 5, 37).
- [41] P. Kurpiers, T. Walter, P. Magnard, Y. Salathe, and A. Wallraff. “Characterizing the attenuation of coaxial and rectangular microwave-frequency waveguides at cryogenic temperatures”. In: *EPJ quantum technology*. 4, pp. 1–15 (cit. on pp. 5, 66).
- [42] G. P. Agrawal. *Fiber-optic communication systems*. John Wiley & Sons, 2012 (cit. on p. 5).
- [43] H.-P. Lo, T. Ikuta, N. Matsuda, T. Honjo, W. J. Munro, and H. Takesue. “Quantum Process Tomography of a Controlled-Phase Gate for Time-Bin Qubits”. In: *Physical Review Applied*. 13, p. 034013 (cit. on p. 6).
- [44] S. Saha, M. Shalaev, J. O’Reilly, I. Goetting, G. Toh, A. Kalakuntla, Y. Yu, and C. Monroe. “High-fidelity remote entanglement of trapped atoms mediated by time-bin photons”. In: *arXiv preprint arXiv:2406.01761* , (cit. on p. 6).
- [45] J. M. Lukens and P. Lougovski. “Frequency-encoded photonic qubits for scalable quantum information processing”. In: *Optica*. 4, pp. 8–16 (cit. on p. 6).

- [46] H.-H. Lu, E. M. Simmerman, P. Lougovski, A. M. Weiner, and J. M. Lukens. “Fully Arbitrary Control of Frequency-Bin Qubits”. In: *Physical Review Letters*. 125, p. 120503 (cit. on p. 6).
- [47] H.-H. Lu, M. Liscidini, A. L. Gaeta, A. M. Weiner, and J. M. Lukens. “Frequency-bin photonic quantum information”. In: *Optica*. 10, pp. 1655–1671 (cit. on p. 6).
- [48] N. A. Peters, J. T. Barreiro, M. E. Goggin, T.-C. Wei, and P. G. Kwiat. “Remote State Preparation: Arbitrary Remote Control of Photon Polarization”. In: *Physical Review Letters*. 94, p. 150502 (cit. on p. 6).
- [49] P. Kok, H. Lee, and J. P. Dowling. “Creation of large-photon-number path entanglement conditioned on photodetection”. In: *Physical Review A*. 65, p. 052104 (cit. on p. 6).
- [50] J. C. F. Matthews, A. Politi, D. Bonneau, and J. L. O’Brien. “Heralding Two-Photon and Four-Photon Path Entanglement on a Chip”. In: *Physical Review Letters*. 107, p. 163602 (cit. on p. 6).
- [51] A. M. Yao and M. J. Padgett. “Orbital angular momentum: origins, behavior and applications”. In: *Advances in Optics and Photonics*. 3, pp. 161–204 (cit. on p. 6).
- [52] J. Ilves, S. Kono, Y. Sunada, S. Yamazaki, M. Kim, K. Koshino, and Y. Nakamura. “On-demand generation and characterization of a microwave time-bin qubit”. In: *npj Quantum Information*. 6, p. 34 (cit. on pp. 6, 42, 67).
- [53] P. Kurpiers et al. “Quantum Communication with Time-Bin Encoded Microwave Photons”. In: *Physical Review Applied*. 12, p. 044067 (cit. on pp. 6, 42, 67).
- [54] K. Boström and T. Felbinger. “Deterministic secure direct communication using entanglement”. In: *Physical Review Letters*. 89, p. 187902 (cit. on p. 6).
- [55] S. Lloyd. “Power of entanglement in quantum communication”. In: *Physical Review Letters*. 90, p. 167902 (cit. on p. 6).
- [56] M. Pennacchietti et al. “Oscillating photonic Bell state from a semiconductor quantum dot for quantum key distribution”. In: *Communications Physics*. 7, p. 62 (cit. on p. 6).
- [57] C. Monroe, R. Raussendorf, A. Ruthven, K. R. Brown, P. Maunz, L.-M. Duan, and J. Kim. “Large-scale modular quantum-computer architecture with atomic memory and photonic interconnects”. In: *Physical Review A*. 89, p. 022317 (cit. on p. 6).
- [58] S. Daiss, S. Langenfeld, S. Welte, E. Distante, P. Thomas, L. Hartung, O. Morin, and G. Rempe. “A quantum-logic gate between distant quantum-network modules”. In: *Science*. 371, pp. 614–617 (cit. on p. 6).

- [59] M. Akhtar, F. Bonus, F. R. Lebrun-Gallagher, N. I. Johnson, M. Siegle-Brown, S. Hong, S. J. Hile, S. A. Kulmiya, S. Weidt, and W. K. Hensinger. “A high-fidelity quantum matter-link between ion-trap microchip modules”. In: *Nature Communications*. 14, p. 531 (cit. on p. 6).
- [60] H. Kimble and L. Mandel. “Theory of resonance fluorescence”. In: *Physical Review A*. 13, p. 2123 (cit. on p. 6).
- [61] I. Strandberg, Y. Lu, F. Quijandría, and G. Johansson. “Numerical Study of Wigner Negativity in One-Dimensional Steady-State Resonance Fluorescence”. In: *Physical Review A*. 100, p. 063808 (cit. on p. 6).
- [62] F. Quijandría, I. Strandberg, and G. Johansson. “Steady-State Generation of Wigner-Negative States in One-Dimensional Resonance Fluorescence”. In: *Physical Review Letters*. 121, p. 263603 (cit. on p. 6).
- [63] Y. Lu, I. Strandberg, F. Quijandría, G. Johansson, S. Gasparinetti, and P. Delsing. “Propagating Wigner-Negative States Generated from the Steady-State Emission of a Superconducting Qubit”. In: *Physical Review Letters*. 126, p. 253602 (cit. on p. 6).
- [64] A. Gonzalez-Tudela, F. P. Laussy, C. Tejedor, M. J. Hartmann, and E. del Valle. “Two-Photon Spectra of Quantum Emitters”. In: *New Journal of Physics*. 15, p. 033036 (cit. on p. 6).
- [65] C. Sánchez Muñoz, E. Del Valle, C. Tejedor, and F. P. Laussy. “Violation of Classical Inequalities by Photon Frequency Filtering”. In: *Physical Review A*. 90, p. 052111 (cit. on p. 6).
- [66] E. Zubizarreta Casalengua, E. Del Valle, and F. P. Laussy. “Two-Photon Correlations in Detuned Resonance Fluorescence”. In: *Physica Scripta*. 98, p. 055104 (cit. on p. 6).
- [67] M. Peiris, B. Petrak, K. Konthasinghe, Y. Yu, Z. C. Niu, and A. Muller. “Two-Color Photon Correlations of the Light Scattered by a Quantum Dot”. In: *Physical Review B*. 91, p. 195125 (cit. on p. 6).
- [68] Y. Nieves and A. Muller. “Third-order photon cross-correlations in resonance fluorescence”. In: *Physical Review B*. 102, p. 155418 (cit. on p. 6).
- [69] J. C. López Carreño, S. Bermúdez Feijoo, and M. Stobińska. “Entanglement in Resonance Fluorescence”. In: *npj Nanophotonics*. 1, p. 3 (cit. on p. 6).
- [70] B. R. Mollow. “Power Spectrum of Light Scattered by Two-Level Systems”. In: *Physical Review*. 188, pp. 1969–1975 (cit. on pp. 6, 23, 56).
- [71] O. Astafiev, A. M. Zagoskin, A. A. Abdumalikov, Y. A. Pashkin, T. Yamamoto, K. Inomata, Y. Nakamura, and J. S. Tsai. “Resonance fluorescence of a single artificial atom”. In: *Science*. 327, pp. 840–843 (cit. on pp. 6, 56).
- [72] B. D. Josephson. “Possible new effects in superconductive tunnelling”. In: *Physics letters*. 1, pp. 251–253 (cit. on pp. 7, 8).
- [73] J. J. Sakurai and J. Napolitano. *Modern Quantum Mechanics*. 3rd ed. Cambridge University Press, 2020 (cit. on p. 10).

- [74] Wikipedia contributors. *Bloch Sphere*. https://en.wikipedia.org/wiki/Bloch_sphere#/media/File: Bloch_sphere.svg. Accessed: 2024-10-29, licensed under CC BY-SA 3.0 (cit. on p. 10).
- [75] J. I. Cirac and P. Zoller. “Quantum Computations with Cold Trapped Ions”. In: *Physical Review Letters*. 74, pp. 4091–4094 (cit. on p. 10).
- [76] Y. Wang, M. Um, J. Zhang, S. An, M. Lyu, J.-N. Zhang, L.-M. Duan, D. Yum, and K. Kim. “Single-qubit quantum memory exceeding ten-minute coherence time”. In: *Nature Photonics*. 11, pp. 646–650 (cit. on p. 10).
- [77] H.-S. Zhong, H. Wang, Y.-H. Deng, M.-C. Chen, L.-C. Peng, Y.-H. Luo, J. Qin, D. Wu, X. Ding, Y. Hu, et al. “Quantum computational advantage using photons”. In: *Science*. 370, pp. 1460–1463 (cit. on p. 10).
- [78] J. Elzerman, R. Hanson, L. Willems van Beveren, B. Witkamp, L. Vandersypen, and L. P. Kouwenhoven. “Single-shot read-out of an individual electron spin in a quantum dot”. In: *nature*. 430, pp. 431–435 (cit. on p. 10).
- [79] J. Yoneda, K. Takeda, T. Otsuka, T. Nakajima, M. R. Delbecq, G. Allison, T. Honda, T. Koder, S. Oda, Y. Hoshi, et al. “A quantum-dot spin qubit with coherence limited by charge noise and fidelity higher than 99.9%”. In: *Nature nanotechnology*. 13, pp. 102–106 (cit. on p. 10).
- [80] F. Arute, K. Arya, R. Babbush, D. Bacon, J. C. Bardin, R. Barends, R. Biswas, S. Boixo, F. G. Brandao, D. A. Buell, et al. “Quantum supremacy using a programmable superconducting processor”. In: *Nature*. 574, pp. 505–510 (cit. on p. 11).
- [81] P. Jurcevic, A. Javadi-Abhari, L. S. Bishop, I. Lauer, D. F. Bogorin, M. Brink, L. Capelluto, O. Günlük, T. Itoko, N. Kanazawa, et al. “Demonstration of quantum volume 64 on a superconducting quantum computing system”. In: *Quantum Science and Technology*. 6, p. 025020 (cit. on p. 11).
- [82] M. Gong, S. Wang, C. Zha, M.-C. Chen, H.-L. Huang, Y. Wu, Q. Zhu, Y. Zhao, S. Li, S. Guo, et al. “Quantum walks on a programmable two-dimensional 62-qubit superconducting processor”. In: *Science*. 372, pp. 948–952 (cit. on p. 11).
- [83] Y. Wu et al. “Strong Quantum Computational Advantage Using a Superconducting Quantum Processor”. In: *Physical Review Letters*. 127, p. 180501 (cit. on p. 11).
- [84] Y. Kim, A. Eddins, S. Anand, K. X. Wei, E. Van Den Berg, S. Rosenblatt, H. Nayfeh, Y. Wu, M. Zaletel, K. Temme, et al. “Evidence for the utility of quantum computing before fault tolerance”. In: *Nature*. 618, pp. 500–505 (cit. on p. 11).
- [85] J. Clarke and F. K. Wilhelm. “Superconducting quantum bits”. In: *Nature*. 453, pp. 1031–1042 (cit. on p. 11).
- [86] Y. Nakamura, Y. A. Pashkin, and J. Tsai. “Coherent control of macroscopic quantum states in a single-Cooper-pair box”. In: *nature*. 398, pp. 786–788 (cit. on p. 11).

- [87] D. Vion, A. Aassime, A. Cottet, P. Joyez, H. Pothier, C. Urbina, D. Esteve, and M. H. Devoret. “Manipulating the quantum state of an electrical circuit”. In: *Science*. 296, pp. 886–889 (cit. on p. 12).
- [88] J. Koch, T. M. Yu, J. Gambetta, A. A. Houck, D. I. Schuster, J. Majer, A. Blais, M. H. Devoret, S. M. Girvin, and R. J. Schoelkopf. “Charge-insensitive qubit design derived from the Cooper pair box”. In: *Physical Review A*. 76, p. 042319 (cit. on p. 12).
- [89] M. Hutchings, J. B. Hertzberg, Y. Liu, N. T. Bronn, G. A. Keefe, M. Brink, J. M. Chow, and B. Plourde. “Tunable superconducting qubits with flux-independent coherence”. In: *Physical Review Applied*. 8, p. 044003 (cit. on p. 13).
- [90] P. Krantz, M. Kjaergaard, F. Yan, T. P. Orlando, S. Gustavsson, and W. D. Oliver. “A quantum engineer’s guide to superconducting qubits”. In: *Applied physics reviews*. 6, (cit. on p. 14).
- [91] A. Wallraff, D. I. Schuster, A. Blais, L. Frunzio, R.-S. Huang, J. Majer, S. Kumar, S. M. Girvin, and R. J. Schoelkopf. “Strong coupling of a single photon to a superconducting qubit using circuit quantum electrodynamics”. In: *Nature*. 431, pp. 162–167 (cit. on p. 15).
- [92] A. Sears, A. Petrenko, G. Catelani, L. Sun, H. Paik, G. Kirchmair, L. Frunzio, L. Glazman, S. Girvin, and R. Schoelkopf. “Photon shot noise dephasing in the strong-dispersive limit of circuit QED”. In: *Physical Review B—Condensed Matter and Materials Physics*. 86, p. 180504 (cit. on p. 16).
- [93] G. Ithier. “Manipulation, readout and analysis of the decoherence of a superconducting quantum bit”. PhD thesis. Université Pierre et Marie Curie-Paris VI, 2005 (cit. on p. 16).
- [94] H.-P. Breuer and F. Petruccione. *The theory of open quantum systems*. Oxford University Press, USA, 2002 (cit. on p. 17).
- [95] C. W. Gardiner and M. J. Collett. “Input and output in damped quantum systems: Quantum stochastic differential equations and the master equation”. In: *Physical Review A*. 31, pp. 3761–3774 (cit. on p. 17).
- [96] R. Loudon. *The Quantum Theory of Light*. 3rd ed. Oxford Science Publications. Oxford ; New York: Oxford University Press, 2000 (cit. on p. 17).
- [97] C. W. Gardiner and P. Zoller. *Quantum Noise: A Handbook of Markovian and Non-Markovian Quantum Stochastic Methods with Applications to Quantum Optics*. 3rd ed. Springer Series in Synergetics. Berlin ; New York: Springer, 2004. ISBN: 978-3-540-22301-6 (cit. on pp. 17, 56).
- [98] BlueFors Cryogenics Ltd. *BF-LD250 Cryogen-Free Dilution Refrigerator System User Manual*. Version 1.5.0. 2016 (cit. on pp. 19, 20).
- [99] G. Ithier et al. “Decoherence in a superconducting quantum bit circuit”. In: *Physical Review B*. 72, p. 134519 (cit. on p. 21).

- [100] I. Strandberg. “Simple, Reliable, and Noise-Resilient Continuous-Variable Quantum State Tomography with Convex Optimization”. In: *Physical Review Applied*. 18, p. 044041 (cit. on pp. 23, 29, 30).
- [101] A. A. Clerk, M. H. Devoret, S. M. Girvin, F. Marquardt, and R. J. Schoelkopf. “Introduction to quantum noise, measurement, and amplification”. In: *Reviews of Modern Physics*. 82, pp. 1155–1208 (cit. on p. 23).
- [102] M. S. Kim. “Quasiprobability functions measured by photon statistics of amplified signal fields”. In: *Physical Review A*. 56, pp. 3175–3179 (cit. on p. 23).
- [103] K. E. Cahill and R. J. Glauber. “Density Operators and Quasiprobability Distributions”. In: *Physical Review*. 177, pp. 1882–1902 (cit. on p. 23).
- [104] R. J. Glauber. “Coherent and Incoherent States of the Radiation Field”. In: *Physical Review*. 131, pp. 2766–2788 (cit. on p. 23).
- [105] W. Kern. “The evolution of silicon wafer cleaning technology”. In: *Journal of the Electrochemical Society*. 137, p. 1887 (cit. on p. 24).
- [106] A. Bengtsson et al. “Improved Success Probability with Greater Circuit Depth for the Quantum Approximate Optimization Algorithm”. In: *Physical Review Applied*. 14, p. 034010 (cit. on p. 25).
- [107] A. Bengtsson. “Quantum information processing with tunable and low-loss superconducting circuits”. PhD thesis. Chalmers Tekniska Hogskola (Sweden), 2020 (cit. on p. 26).
- [108] Ansys Inc. *Ansys HFSS (version 2020 R1) [Computer software]*. Available from <https://www.ansys.com/> (cit. on p. 26).
- [109] M. Pechal. “Microwave photonics in superconducting circuits”. PhD thesis. ETH Zurich, 2016 (cit. on pp. 26, 45).
- [110] C. Eichler. “Experimental characterization of quantum microwave radiation and its entanglement with a superconducting qubit”. PhD thesis. ETH Zurich, 2013 (cit. on pp. 27, 29).
- [111] Intermodulation Product. *Vivace microwave platform* (cit. on pp. 28, 73).
- [112] R. Nehra, M. Eaton, C. González-Arciniegas, M. S. Kim, T. Gerrits, A. Lita, S. W. Nam, and O. Pfister. “Generalized overlap quantum state tomography”. In: *Physical Review Research*. 2, p. 042002 (cit. on p. 29).
- [113] A. V. Rodionov, A. Veitia, R. Barends, J. Kelly, D. Sank, J. Wenner, J. M. Martinis, R. L. Kosut, and A. N. Korotkov. “Compressed sensing quantum process tomography for superconducting quantum gates”. In: *Physical Review B*. 90, p. 144504 (cit. on p. 30).
- [114] Y. Wang, L. Liu, S. Cheng, L. Li, and J. Chen. “Efficient factored gradient descent algorithm for quantum state tomography”. In: *Physical Review Research*. 6, p. 033034 (cit. on p. 31).
- [115] D. Greenbaum. “Introduction to quantum gate set tomography”. In: *arXiv preprint arXiv:1509.02921*, (cit. on pp. 32, 33).

- [116] A. Gaikwad, K. Shende, Arvind, and K. Dorai. “Implementing efficient selective quantum process tomography of superconducting quantum gates on IBM quantum experience”. In: *Scientific Reports*. 12, p. 3688 (cit. on pp. 32, 53).
- [117] A. Gaikwad, Arvind, and K. Dorai. “Efficient experimental characterization of quantum processes via compressed sensing on an NMR quantum processor”. In: *Quantum Information Processing*. 21, p. 388 (cit. on p. 32).
- [118] R. Jozsa. “Fidelity for mixed quantum states”. In: *Journal of Modern Optics*. 41, pp. 2315–2323 (cit. on p. 33).
- [119] F. Motzoi, J. M. Gambetta, P. Rebentrost, and F. K. Wilhelm. “Simple pulses for elimination of leakage in weakly nonlinear qubits”. In: *Physical review letters*. 103, p. 110501 (cit. on p. 33).
- [120] M. Werninghaus, D. J. Egger, F. Roy, S. Machnes, F. K. Wilhelm, and S. Filipp. “Leakage reduction in fast superconducting qubit gates via optimal control”. In: *npj Quantum Information*. 7, p. 14 (cit. on p. 33).
- [121] P. Magnard, P. Kurpiers, B. Royer, T. Walter, J.-C. Besse, S. Gasparinetti, M. Pechal, J. Heinsoo, S. Storz, A. Blais, et al. “Fast and unconditional all-microwave reset of a superconducting qubit”. In: *Physical review letters*. 121, p. 060502 (cit. on p. 33).
- [122] M. A. Aamir, P. J. Suria, J. A. M. Guzmán, C. Castillo-Moreno, J. M. Epstein, N. Y. Halpern, and S. Gasparinetti. “Thermally driven quantum refrigerator autonomously resets superconducting qubit”. In: *arXiv preprint arXiv:2305.16710* , (cit. on p. 33).
- [123] X. Dong, X. Cao, W.-L. Li, G. Zhang, Z. Peng, and R.-B. Wu. “The Shaping of Flying Qubits based on Quantum Optimal Control Theory”. In: *arXiv preprint arXiv:2404.09487* , (cit. on p. 45).
- [124] M. Ganzhorn et al. “Benchmarking the noise sensitivity of different parametric two-qubit gates in a single superconducting quantum computing platform”. In: *Physical Review Research*. 2, p. 033447 (cit. on p. 46).
- [125] M. Scigliuzzo, A. Bengtsson, J.-C. Besse, A. Wallraff, P. Delsing, and S. Gasparinetti. “Primary Thermometry of Propagating Microwaves in the Quantum Regime”. In: *Physical Review X*. 10, p. 041054 (cit. on pp. 56, 77).
- [126] H. P. Breuer and F. Petruccione. *The Theory of Open Quantum Systems*. Oxford University Press, Jan. 2007. ISBN: 978-0-19-921390-0 (cit. on p. 56).
- [127] H. Carmichael. *An Open Systems Approach to Quantum Optics*. Vol. 18. Lecture Notes in Physics Monographs. Berlin, Heidelberg: Springer Berlin Heidelberg, 1993. ISBN: 978-3-540-56634-2 (cit. on p. 56).
- [128] J. J. García Ripoll. *Quantum Information and Quantum Optics with Superconducting Circuits*. 1st ed. Cambridge University Press, July 2022 (cit. on p. 56).
- [129] H. J. Kimble and L. Mandel. “Theory of resonance fluorescence”. In: *Physical Review A*. 13, pp. 2123–2144 (cit. on p. 56).

- [130] A. H. Kiilerich and K. Mølmer. “Input-Output Theory with Quantum Pulses”. In: *Physical Review Letters*. 123, p. 123604 (cit. on p. 56).
- [131] Y. Lu, A. Bengtsson, J. J. Burnett, B. Suri, S. R. Sathyamoorthy, H. R. Nilsson, M. Scigliuzzo, J. Bylander, G. Johansson, and P. Delsing. “Quantum efficiency, purity and stability of a tunable, narrowband microwave single-photon source”. In: *npj Quantum Information*. 7, p. 140 (cit. on p. 59).
- [132] G. Vidal and R. F. Werner. “Computable measure of entanglement”. In: *Physical Review A*. 65, p. 032314 (cit. on p. 61).
- [133] J. I. Cirac, R. Blatt, A. S. Parkins, and P. Zoller. “Spectrum of resonance fluorescence from a single trapped ion”. In: *Physical Review A*. 48, pp. 2169–2181 (cit. on p. 65).
- [134] V. Bühner and C. Tamm. “Resonance fluorescence spectrum of a trapped ion undergoing quantum jumps”. In: *Physical Review A*. 61, p. 061801 (cit. on p. 65).
- [135] M. Bienert, J. M. Torres, S. Zippilli, and G. Morigi. “Resonance fluorescence of a cold atom in a high-finesse resonator”. In: *Physical Review A*. 76, p. 013410 (cit. on p. 65).
- [136] A. Müller, E. B. Flagg, P. Bianucci, X. Y. Wang, D. G. Deppe, W. Ma, J. Zhang, G. J. Salamo, M. Xiao, and C. K. Shih. “Resonance fluorescence from a coherently driven semiconductor quantum dot in a cavity”. In: *Physical Review Letters*. 99, p. 187402 (cit. on p. 65).
- [137] M. N. Makhonin, J. E. Dixon, R. J. Coles, B. Royall, I. J. Luxmoore, E. Clarke, M. Hugues, M. S. Skolnick, and A. M. Fox. “Waveguide coupled resonance fluorescence from on-chip quantum emitter”. In: *Nano Letters*. 14, pp. 6997–7002 (cit. on p. 65).
- [138] J. M. Higbie, J. D. Perreault, V. M. Acosta, C. Belthangady, P. Lebel, M. H. Kim, K. Nguyen, V. Demas, V. Bajaj, and C. Santori. “Multiphoton-excited fluorescence of silicon-vacancy color centers in diamond”. In: *Physical Review Applied*. 7, p. 054010 (cit. on p. 65).
- [139] D. Chen et al. “Quantum interference of resonance fluorescence from Germanium-vacancy color centers in diamond”. In: *Nano Letters*. 22, pp. 6306–6312 (cit. on p. 65).
- [140] N. Ofek, A. Petrenko, R. Heeres, P. Reinhold, Z. Leghtas, B. Vlastakis, Y. Liu, L. Frunzio, S. M. Girvin, L. Jiang, et al. “Extending the lifetime of a quantum bit with error correction in superconducting circuits”. In: *Nature*. 536, pp. 441–445 (cit. on p. 67).
- [141] S. Kono, K. Koshino, Y. Tabuchi, A. Noguchi, and Y. Nakamura. “Quantum non-demolition detection of an itinerant microwave photon”. In: *Nature Physics*. 14, pp. 546–549 (cit. on p. 67).

- [142] J.-C. Besse, S. Gasparinetti, M. C. Collodo, T. Walter, P. Kurpiers, M. Pechal, C. Eichler, and A. Wallraff. “Single-Shot Quantum Nondemolition Detection of Individual Itinerant Microwave Photons”. In: *Physical Review X*. 8, p. 021003 (cit. on p. 67).
- [143] F. Riera-Sàbat and W. Dür. “A modular entanglement-based quantum computer architecture”. In: *arXiv preprint arXiv:2406.05735* , (cit. on p. 67).
- [144] W. Tang, T. Tomesh, M. Suchara, J. Larson, and M. Martonosi. “Cutqc: using small quantum computers for large quantum circuit evaluations”. In: *Proceedings of the 26th ACM International conference on architectural support for programming languages and operating systems*. 2021, pp. 473–486 (cit. on p. 67).
- [145] R. Renner. “Security of quantum key distribution”. In: *International Journal of Quantum Information*. 6, pp. 1–127 (cit. on p. 68).
- [146] M. Mehic, M. Niemiec, S. Rass, J. Ma, M. Peev, A. Aguado, V. Martin, S. Schauer, A. Poppe, C. Pacher, et al. “Quantum key distribution: a networking perspective”. In: *ACM Computing Surveys (CSUR)*. 53, pp. 1–41 (cit. on p. 68).
- [147] C. Simon. “Towards a global quantum network”. In: *Nature Photonics*. 11, pp. 678–680 (cit. on p. 68).
- [148] *How a real 5G Quantum AI use case could disrupt antenna tilting, Ericsson Research*. Accessed: 2024-11-04 (cit. on p. 69).
- [149] D. Bern. “Quantum Annealing Algorithms for PAPR Minimisation in Wireless Networks”. MA thesis. Uppsala University, 2022 (cit. on p. 69).
- [150] W. Laius Lundgren. “Quantum Algorithms for Feature Selection and Compressed Feature Representation of Data”. MA thesis. KTH Royal Institute of Technology, 2023 (cit. on p. 69).
- [151] M. S. Khalil, M. Stoutimore, F. Wellstood, and K. Osborn. “An analysis method for asymmetric resonator transmission applied to superconducting devices”. In: *Journal of Applied Physics*. 111, (cit. on pp. 75, 76).
- [152] S. Probst, F. Song, P. A. Bushev, A. V. Ustinov, and M. Weides. “Efficient and robust analysis of complex scattering data under noise in microwave resonators”. In: *Review of Scientific Instruments*. 86, (cit. on p. 76).